Aerospace Engineering Sciences Graduate Theses & Dissertations

Aerospace Engineering Sciences

Summer 7-22-2014

Relativistic Electrons in Earth's Outer Radiation Belt: Wave-Particle Interactions and Precipitation Loss

Lauren Weber Blum
University of Colorado Boulder, lwblum@gmail.com

Relativistic Electrons in Earth's Outer Radiation Belt: Wave-Particle Interactions and

Precipitation Loss

by

Lauren W. Blum

B.A., Dartmouth College, 2007

M.A., Boston University, 2010

A thesis submitted to the

Faculty of the Graduate School of the

University of Colorado in partial fulfillment

of the requirement for the degree of

Doctor of Philosophy

Department of Aerospace Engineering Sciences

2014

This Thesis entitled:
Relativistic Electrons in Earth's Outer Radiation Belt: Wave-Particle Interactions and Precipitation Loss
written by Lauren W. Blum
has been approved for the Department of Aerospace Engineering and Sciences

_____
Prof. Xinlin Li

_____
Prof. Dan Baker

_____
Prof. Zoltan Sternovsky

_____
Prof. Scott Palo

_____
Prof. Howard Singer

Date _____

The final copy of this proposal has been examined by the signatories, and we find that both the content
and the form meet acceptable presentation standards of scholarly work in the above mentioned discipline.

Blum, Lauren W. (Ph.D., Aerospace Engineering Sciences)

Relativistic Electrons in Earth's Outer Radiation Belt: Wave-Particle Interactions and

      Precipitation Loss

Thesis directed by Professor Xinlin Li

Earth's outer radiation belt is a highly dynamic region of the magnetosphere composed of relativistic electrons with often unpredictable variations in energy and spatial extent. Understanding this variable radiation environment is critical for protecting both spacecraft and humans in space. A number of competing acceleration and loss processes combine to produce net enhancements or depletions of the outer radiation belt. Electron precipitation into the atmosphere is a critical part of this loss, and quantified understanding of this mechanism is needed in order to understand and ultimately predict radiation belt dynamics. In the following work, we investigate the contribution of electron precipitation to radiation belt losses, looking at what times precipitation is important and at how much loss it contributes. Through a combination of long-term existing data sets as well as new CubeSat measurements we perform both statistical and detailed event studies to better understand the nature and extent of MeV electron loss to the atmosphere. We analyze measurements of precipitating electrons directly as well as electromagnetic waves that may be causing this precipitation. Our studies provide a more cohesive picture of outer radiation belt dynamics and the relationship between precipitating energetic electrons and global magnetospheric conditions.

Dedication

To my family and friends for their continual support and encouragement.

Acknowledgements

Thank you first and foremost to my advisor Xinlin Li, for not only encouraging me to join CU and the Aerospace Department, but giving me the rare opportunity to play a leading role in a hardware project like CSSWE. Being on this CubeSat team has shaped my graduate experience, and I am very grateful to have had this opportunity. The many CSSWE team members and mentors that made the project so exciting and successful, thank you as well. Thanks to my committee members for their guidance and support: Howard Singer, Dan Baker, Scott Palo, and Zoltan Sternovsky. I would also like to thank the research advisors and mentors I've had along the way that got me to this point – Kristina Lynch, Liz MacDonald, Harlan Spence, and others. I appreciate the encouragement, direction, and motivation they have provided. And finally, a big thank you to fellow graduate students, past and present, and the other members of Xinlin's research group – for all the discussions, advice, support, and happy hours that have taught me so much and made me look forward to coming in every day.

TABLE OF CONTENTS

LIST OF TABLES

LIST OF FIGURES

Chapter 1: Introduction

The radiation belts are a highly dynamic region of Earth's magnetosphere, with often-unpredictable variations in intensity and spatial range. The high energy particles found in this region can be damaging to both spacecraft and humans in space, and understanding this variable radiation environment and its response to geomagnetic activity is critical to mitigating spacecraft anomalies. The physical processes controlling the acceleration and loss of trapped relativistic electrons in the radiation belts are complex, and there are a number of competing processes that can combine to produce net enhancements or depletions of the belts. Particle precipitation into the atmosphere is a critical part of radiation belt electron loss, and without quantified understanding of this loss mechanism, we are unable to fully understand acceleration mechanisms. The work in this dissertation addresses two main topics, both related to understanding the role of precipitation loss on the overall dynamics of the outer radiation belt. In the first half of this work, we focus on one wave mode in particular, electromagnetic ion cyclotron (EMIC) waves, believed to be responsible for scattering MeV electrons into the atmosphere. Studying the distributions of these waves, as well as the conditions in which they are generated, can give insight into when this particular loss mechanism may be active. The latter half of this work then shifts to examine precipitating electrons directly, with studies enabled by measurements at low altitude from both the 20 year SAMPEX mission as well as the more recent Colorado Student Space Weather Experiment (CSSWE) CubeSat, designed, built, and operated by students at the University of Colorado.

We begin in Chapter 2 with a brief overview of the terrestrial magnetospheric system and the various plasma populations that make it up. The focus is on the outer Van Allen radiation

belt and the various source and loss mechanisms that contribute to its overall dynamics. In particular, we look at the role of wave-particle interactions, which can scatter MeV electrons into the atmosphere, and review the basic physics behind these resonant interactions. Finally, some of the open questions in radiation belt physics that motivate our work are outlined.

Theory has shown that EMIC waves, which arise from anisotropic ion populations, can resonantly interact with energetic electrons and scatter them into the atmosphere. Studies of this anisotropic ion population and free energy source can give insight into the likely presence and growth of these waves, and thus aid studies of this precipitation loss process. In Chapter 3, we investigate the local plasma conditions in which EMIC waves develop and use this to create a plasma-based proxy for the waves. To test the validity of the proxy, we compare EMIC wave distributions inferred from Los Alamos National Laboratory (LANL) plasma data at geosynchronous orbit (GEO) with wave measurements from GOES spacecraft, also at GEO. This chapter describes the development of the plasma-based wave proxy and validates the use of it for future investigations of EMIC wave distributions in the inner magnetosphere.

Next, using this proxy, we investigate the storm-time distributions of EMIC waves in relation to radiation belt enhancements and suppressions. Some geomagnetic storms result in net radiation belt enhancements, while others cause depletions or no net change at all. Understanding what processes lead to these differing post-storm results is still one of the open questions and goals of radiation belt studies. Chapter 4 details a superposed epoch study performed to investigate plasma conditions and inferred wave distributions in local time as well as storm phase. Utilizing seven LANL spacecraft spanning ~15 years, we are thus able to statistically examine inferred EMIC wave distributions during two different sets of storms – ones resulting in post-storm enhancements of outer radiation belt MeV electrons and ones resulting in

no enhancements. This study gives insight into the global distributions of EMIC waves during storm times and their relation to post-storm radiation belt responses.

In addition to an understanding of electromagnetic wave distributions in the magnetosphere, characterization of relativistic electron precipitation is needed to fully understand radiation belt losses into Earth's atmosphere. Thus in Chapter 5, we move to study precipitating MeV electrons directly. In particular, signatures of rapid pitch angle scattering into the loss cone are often observed by low altitude satellites. Through high-cadence low-altitude measurements from the SAMPEX satellite, we investigate two distinct types of rapid precipitation: millisecond-long "microbursts" as well as longer duration "precipitation bands." The distributions of these events are analyzed over a variety of geomagnetic conditions to look at the relative contributions of these two precipitation types to overall radiation belt losses.

Finally, in Chapters 6 and 7 we discuss some new low-altitude measurements used to further characterize radiation belt precipitation. The CSSWE CubeSat, built by graduate students at the University of Colorado Boulder, was launched in September 2012 into a low-altitude, high-inclination orbit and measures energetic particles precipitating from the radiation belts into Earth's atmosphere. A brief overview of the CSSWE system and the scientific measurements it provides is given in Chapter 6, as well as my involvement in the project, namely as Project Manager for the past three years. Chapter 7 presents one result from the mission thus far, a detailed conjunction study quantifying loss during rapid precipitation events. By combining magnetically conjugate measurements from CSSWE and the 2013 BARREL balloon campaign, measuring electron precipitation signatures above Antarctica, we estimate the spatial features of rapid precipitation events and quantify the number of electrons lost to the atmosphere during such events.

Our studies of long-term existing data sets, combined with these new measurements, help form a more cohesive picture of the relationship between electromagnetic waves, their source populations, and the interactions of these waves with relativistic electrons in the outer radiation belt. Through a combination of numerous in situ measurements – of the low energy plasma populations, high energy radiation belt electrons, and electromagnetic waves – we perform both statistical as well as detailed event studies to better understand the nature and extent of MeV precipitation and radiation belt losses. These studies aid in the understanding of outer radiation belt dynamics and the relationship between precipitating energetic electrons and global magnetospheric conditions.

Chapter 2: Relevant Background

2.1 Earth's Inner Magnetosphere

The magnetosphere is a tear-shaped region carved out of the solar wind by Earth's internal, roughly dipolar magnetic field. The solar wind, emitted radially outward from the sun, compresses this dipole field on the dayside while the tail of the magnetosphere stretches back up to 100s of Earth radii (R_E, =6371 km). Separating the magnetosphere from interplanetary space is a boundary termed the magnetopause, whose location is determined primarily by a balance between solar wind flow pressure and the magnetic pressure of Earth's field. While this boundary is typically located at geocentric distances of ~10 R_E at the subsolar point, its location is highly dynamic and can be moved inwards of 6 R_E during large solar wind pressure pulses. Numerous overlapping particle populations and current systems exist within the magnetosphere, illustrated in Figure 2.1, and a few of the regions relevant to this work are discussed below.
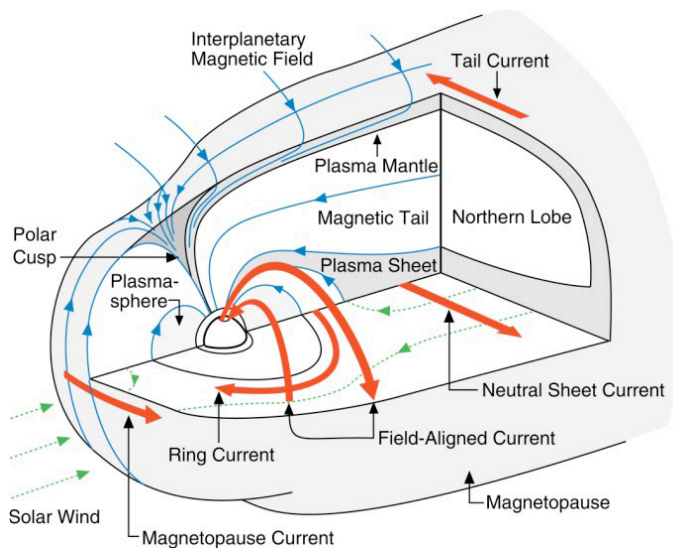
Figure 2.1   A schematic of Earth's magnetosphere, with various plasma populations and current systems labeled. (Adapted from *Kivelson and Russell*, 1995)

2.1.1 Particle Populations

The plasmasphere (depicted in Figure 2.1) is a cold (~eV), dense (~10^3 cm^{-3}) region of plasma, sitting just above the ionosphere and extending outwards to distances of 2-6 R_E, depending on solar wind and geomagnetic conditions. It is composed primarily of H$^+$ ions, but He$^+$, O$^+$, O^{2+}, N$^+$, and N^{2+} have also been observed. The motion of this plasma is determined by the summation of an inward pointing corotation electric field and a dawn-dusk convection electric field, depicted in Figure 2.2. Close to Earth, the corotation field dominates, and thus the cold plasmamasphere tends to corotate about Earth, following lines of constant potential. The boundary of this region, the plasmapause, is determined by the strength of the convection electric field; during geomagnetically active times, when convection is enhanced, this boundary moves inward, shrinking the plasmasphere and often creating drainage plumes on the dusk side, as illustrated in Figure 2.3. These plumes bring cold, dense material to larger radial distances across the afternoon sector and out to the magnetopause.

Overlapping the outer extent of the plasmasphere, starting at roughly 4 R_E, is the ring current, composed of 10s to a few 100s keV ions and electrons drifting opposite directions about Earth, creating a westward-directed current. While less dense than the plasmasphere (typical ring current densities are ~1 cm^{-3}), this population contains the bulk of the energy density in the inner magneosphere. This population is also responsible for providing the free energy source for some types of wave growth in the inner magnetosphere. The strength of the ring current, as well as its composition, is highly dependent on geomagnetic activity, and the dynamics of this region during geomagnetic storms will be discussed further in Section 2.1.3.
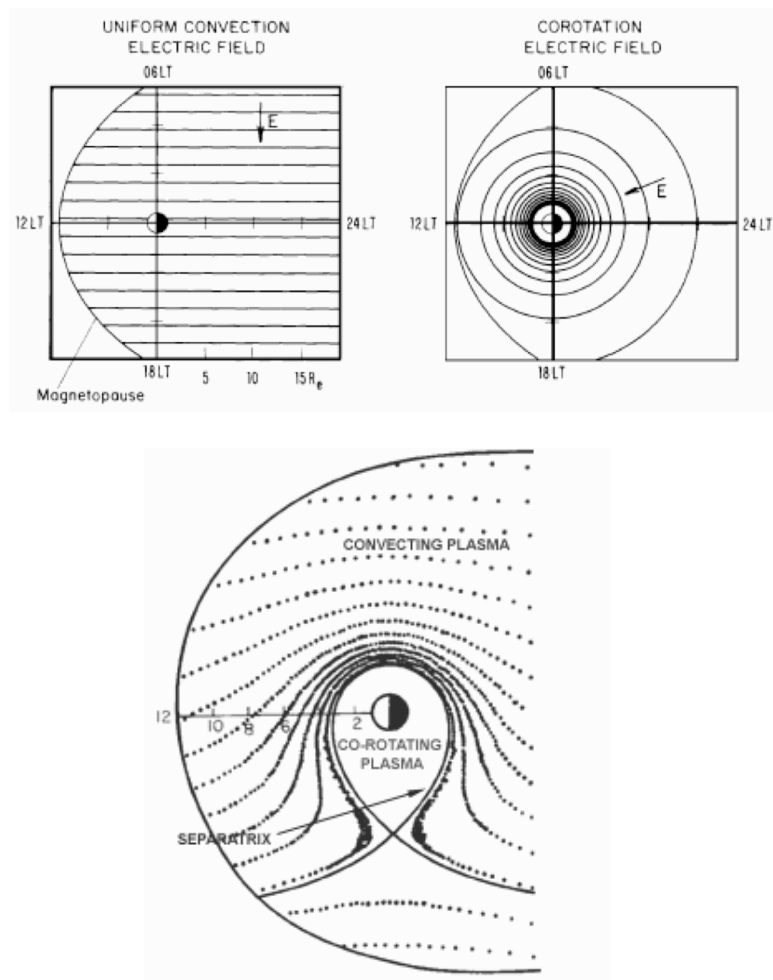
Figure 2.2   Lines of constant potential from the convection electric field (upper left), corotation electric field (upper right), and the total electric field (bottom), a combination of the two. (Top panels from *Lyons and Williams*, 1984; bottom panel adapted from *Kavanagh et al.*, 1968)
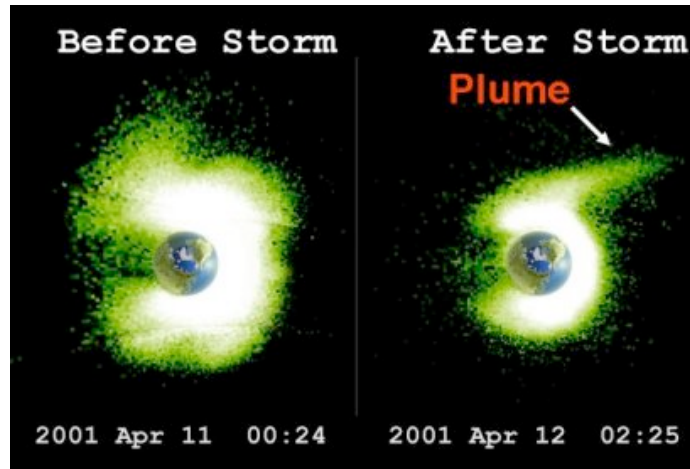
Figure 2.3 Extreme ultraviolet (EUV) images of the plasmasphere taken by the IMAGE satellite. The sun is to the right, and the shadow of Earth is visible on the left hand side of each image. Left hand panel shows an extended plasmasphere prior to the April 2001 storm, while the right panel shows the post-storm plasmasphere, compressed in closer to Earth with a drainage plume extending outward towards the dayside magnetopause. (Copyright Jerry Goldstein/SwRI)

The most energetic and tenuous population in the inner magnetosphere is found in the radiation belts, toroidal regions of energetic particles. In the steady state picture, two belts exist: an inner belt, centered around 1.5 R_E and dominated by multi-MeV protons, and an outer belt, peaking between 4-5 R_E, composed primarily of electrons ranging from 100s keV up to multi-MeV energies. A region of low flux, called the slot region, exists in between the two belts. Typical fluxes of the two species during solar maximum are shown in Figure 2.4 based on NASA's empirical AP/AE-8 model, a statistical model derived from over 20 satellites.

2.1.2 Charged Particle Motion

The toroidal shape of the radiation belts is dictated by charged particle motion in a dipole magnetic field, which is composed of three main, periodic motions – gyration about the field line, bouncing along the field line, and drift motion about Earth (illustrated in Figure 2.5). Particles gyrate perpendicularly around a magnetic field line, electrons in a right handed sense
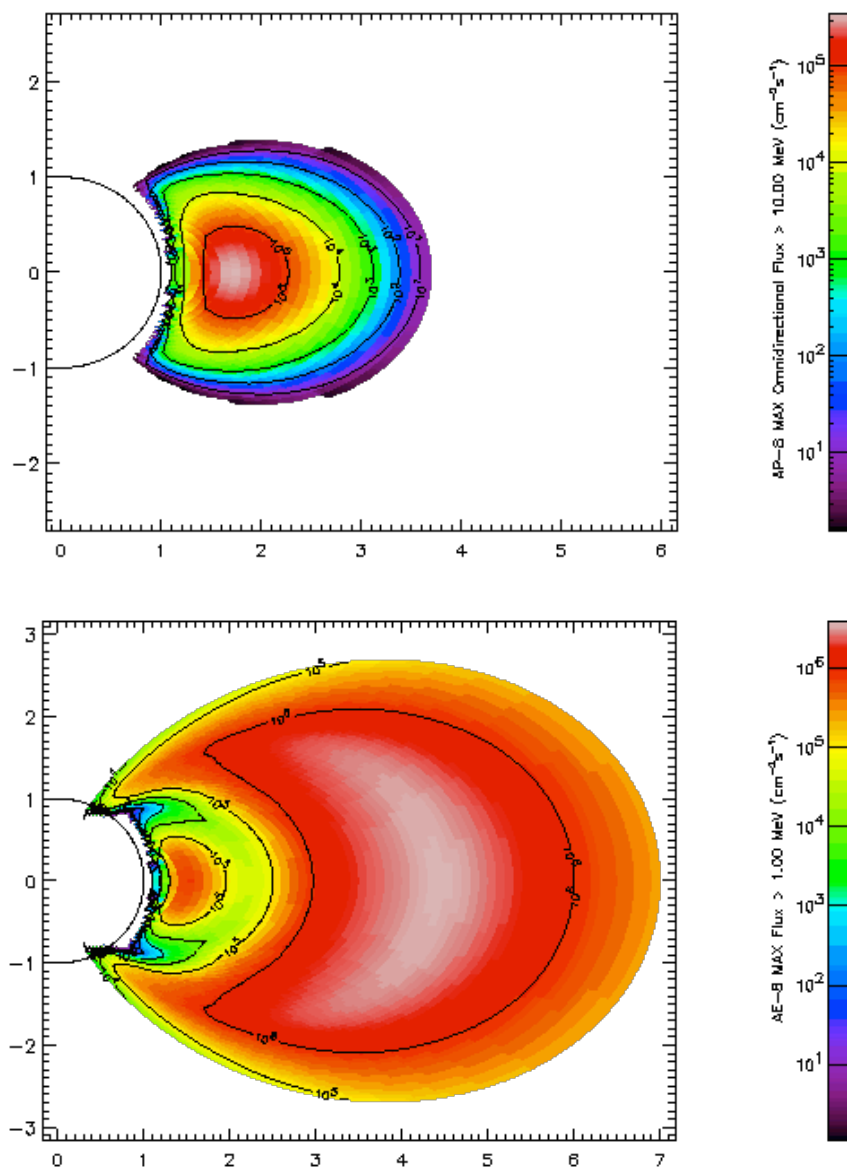
Figure 2.4 NASA AP-8 and AE-8 empirical models for the radiation environment during solar maximum. Top panel (AP-8) shows integral proton flux for energies >10 MeV and bottom panel (AE-8) >1 MeV integral electron flux. Axes show distance in units of Earth radii (R_E). (From the Space Environment Information System website – www.spenvis.oma.be)

and protons left handed. The gyration or cyclotron frequency is defined as $\Omega_i = |q_i|B/m_i$, where i denotes particle species, q particle charge, B magnetic field strength, and m the mass of the particle. As a particle travels along a field line, the field-aligned gradient of the magnetic field will cause its velocity parallel to this field ($v_{\parallel}$) to decrease and ultimately reverse at a "mirror

point," whose location is determined by the magnetic field gradient and the particle pitch angle, defined as α where $\tan(\alpha)=v_\perp/v_\parallel$. This mirror point occurs at the point at which $B=B_0/\sin^2\alpha_0$, where B_0 is the minimum field strength along the field line and α_0 the pitch angle at this minimum. Particles in the magnetosphere whose mirror point is below ~100km altitude will be lost to the atmosphere before they can return up the field line, while particles mirroring above this height remain trapped in the inner magnetosphere. A loss cone can thus be defined as all pitch angles small enough to be lost to the atmosphere for a given magnetic field configuration. An empty loss cone would imply that all particles remain trapped in the magnetosphere, while a full loss cone would lead to rapid particle precipitation.
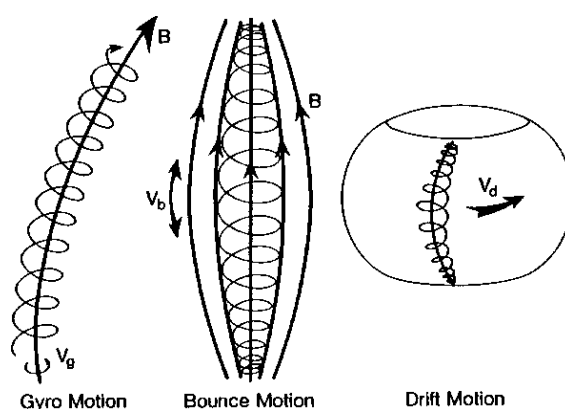
Figure 2.5 **The three characteristic motions of a charged particle in a dipole magnetic field. An electron (proton) will gyrate about the field line in a right (left) hand sense (depicted on the far left). A field-aligned gradient of the magnetic field causes a particle's parallel velocity to decrease as it moves to regions of higher field strength, until a point termed the "mirror point" when it reverses and returns back along the field line. Motion between two mirror points creates the bounce motion depicted in the middle panel. Finally, field gradient and curvature effects cause electrons (protons) to drift eastward (westward) about Earth as they gyrate and bounce (depicted on the far right). (From *Kivelson and Russell*, 1995)**

Finally, the curvature and radial gradient of Earth's magnetic field cause electrons to drift eastward about Earth and ions to drift westward. This charge-dependent drift is the source of the ring current, described previously. Figure 2.6 shows the timescales associated with these periodic motions for electrons and protons over a range of energies and radial distances. For a 1

MeV electron in the outer radiation belt, gyration, bounce, and drift periods are roughly 10^{-3}, 10^0, and 10^3 seconds, respectively.
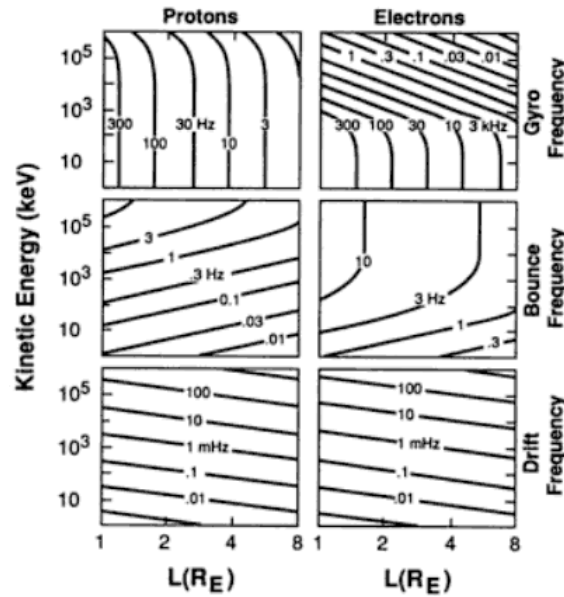
Figure 2.6 Gyration, bounce, and drift frequencies for equatorially mirroring particles in Earth's magnetic field as a function of energy and radial distance. (Adapted from Schulz and Lanzerotti, 1974)

With each of these periodic motions is an associated adiabatic invariant, whose value is conserved so long as fields do not vary on timescales faster than the oscillation frequency. The first adiabatic invariant μ, associated with gyromotion, is defined as $p_\perp^2/2m_0 B_o$, where $p_\perp$ is the momentum perpendicular to the background magnetic field B_0, and m_0 is the rest mass. The second invariant J equals $\oint p_\parallel \, ds$, or the momentum parallel to B_0 integrated over the guiding center path of the particle over one bounce period. This is often rewritten as $K=J/[2\sqrt{(2m_0\mu)}]$. Finally, the third adiabatic invariant ϕ is related to the drift motion of a particle about Earth, and is equal to the magnetic flux contained within the orbit path. This invariant is often written in terms of the Roederer L* parameter, equal to $2\pi k_0/(\phi R_E)$, where k_0 is Earth's magnetic moment

[*Roederer*, 1970]. In a perfect dipole field, L* is equal to a parameter known as McIlwain L. This L is defined as the geocentric distance to a magnetic field line at its equatorial crossing point, in units of R_E [*McIlwain*, 1961]. In non-dipolar or time-varying fields, this L value is not necessarily conserved and is no longer equivalent to L*, but it is less computationally expensive to calculate and still useful for organizing particle populations in the inner magnetosphere so L or L shell will often be used in studies presented here.

These adiabatic invariants are often used when examining particle phase space density (PSD) in the radiation belts. Typically a function of position and velocity vectors, PSD can also be expressed in terms of these three adiabatic coordinates, μ, K, and L*. This coordinate system is often used to distinguish between true acceleration/loss of particles and simply adiabatic changes that will revert back to the original state once a disturbance passes. PSD profiles are also commonly used to identify the source location of electron energization [e.g. *Green and Kivelson,* 2004].

2.1.3 Geomagnetic Storms

Geomagnetic storms are temporary global disturbances of the magnetic field, driven by transient solar wind events. One of the most common measures of a storm is the Disturbance Storm Time, or Dst, index. As the storm-time ring current becomes enhanced, this current induces a southward magnetic field, oppositely directed from that of Earth's. This negative deflection in field strength is measured at multiple magnetometer stations on the ground, and is used to create the Dst index. An example of this index is shown in Figure 2.7, capturing a large geomagnetic storm occurring around Day 25. The maximum deflection of the field (or Dst$_{min}$) reaches roughly -140 nT, indicated by the red star. Storms can typically be broken up into three phases: storm sudden commencement or "initial phase", where the Dst becomes positive briefly;

the "main phase", as the ring current builds up to its maximum and Dst drops to negative

values; and finally the "recovery phase" as the storm-time ring current decays away, returning

Dst and the magnetosphere to a quiet-time state.
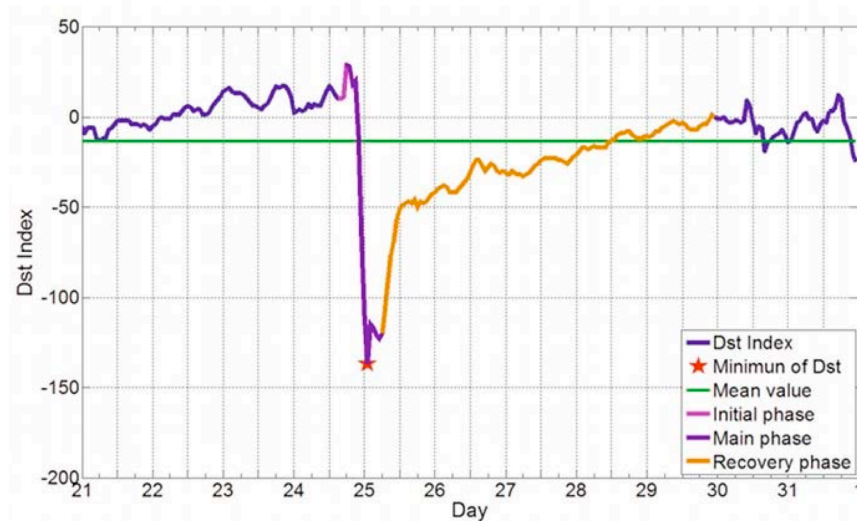
Figure 2.7 Dst index during a geomagnetic storm occurring on Day 25. The three primary storm phases are marked in different colors, pink, purple, and yellow. (From *Sarachaga et al.*, 2014)

Two main solar wind drivers of geomagnetic storms exist: coronal mass ejections

(CMEs) and corotating interaction regions (CIRs). CME-driven storms typically have large

negative Dst signatures and are most frequent during solar maximum. CIR-driven storms, on the

other hand, often produce less extreme excursions in Dst but have more extended recovery

phases [*Borovsky and Denton*, 2006]. They are associated with high speed streams (HSSs) in the

solar wind, produced by coronal holes on the sun, most common during the declining phase of

the solar cycle. These storms are often recurrent with a 27-day periodicity, the solar rotation

period. Geomagnetic storms can have dramatic effects on the particle populations within Earth's

magnetosphere, and the two storm types often result in different magnetospheric responses. In

particular, the radiation belt is highly responsive to geomagnetic activity, and these dynamics are

described in the following section.

2.2 Radiation Belt Dynamics

While the inner radiation belt is fairly stable, the outer belt can be highly dynamic, with often-unpredictable variations in intensity and spatial extent, particularly following geomagnetic storms. The physical processes controlling the acceleration and loss of trapped relativistic electrons in the radiation belts are complex, and there are a number of competing processes that can combine to produce net enhancements or depletions of the belts. NASA's Van Allen Probes mission [*Kessel et al.*, 2012], launched in August 2012 to investigate these dynamics, has provided an unprecedented look at the detailed phenomena affecting the radiation belts. Figure 2.8 from *Baker et al.* [2013] illustrates this highly variable response of the outer radiation belt to geomagnetic storms, showing 4.5 MeV electrons measured by the Van Allen Probes/REPT instrument [*Baker et al.*, 2012] across L* and time during three consecutive storms, each of roughly similar magnitude as indicated by the Dst index on the bottom panel. Understanding the combination of processes that produce these dramatically different responses in the magnitude, location, and structure of the outer belt is still an open area of study.

More statistically, *Reeves et al.* [2003] found that roughly 50% of geomagnetic storms cause enhancements in the outer radiation belt, ~20% cause depletions, and the remaining 30% result in no significant change in MeV electron flux. Understanding which storms cause what response, and if there are any predictive factors in the solar wind or magnetosphere, has long been a subject of study in the radiation belt community. To understand radiation belt dynamics and ultimately predict relativistic electron variations, an understanding of both acceleration *and* loss mechanisms is needed. Below we briefly review some of the primary acceleration and loss processes affecting radiation belt electrons.
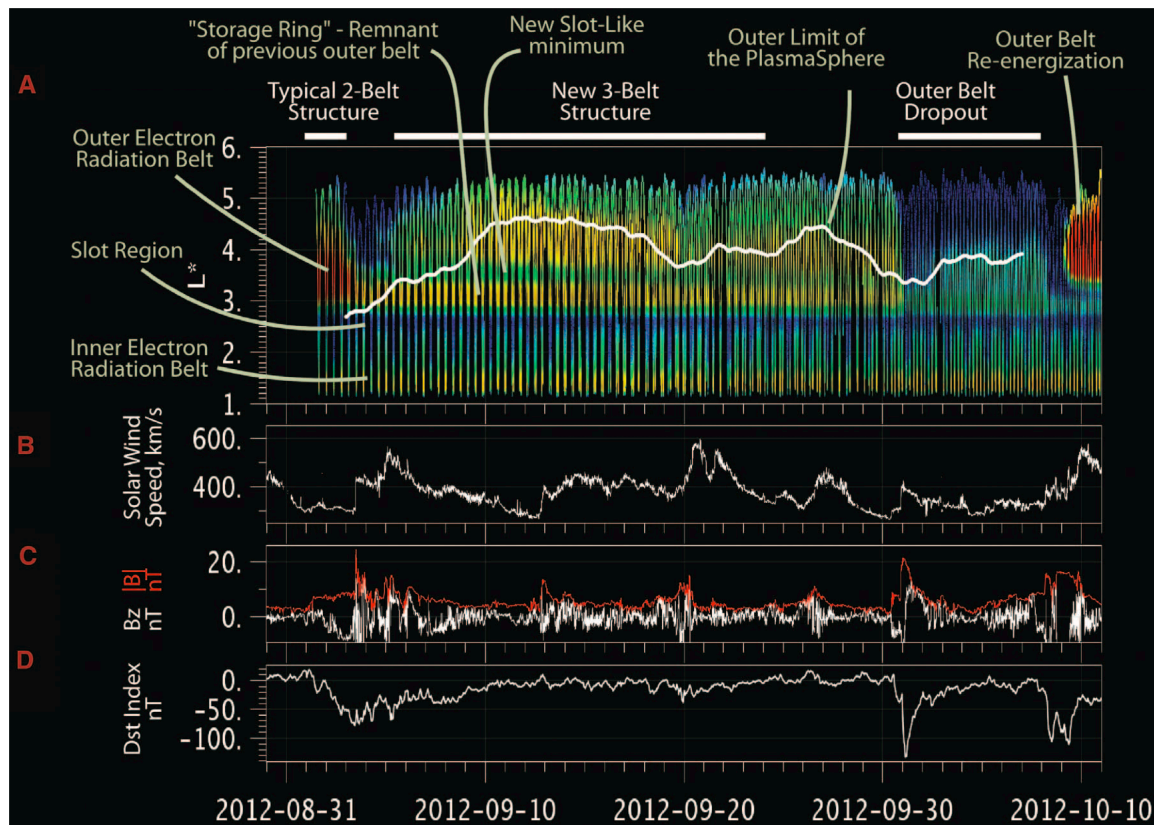
Figure 2.8 (a) 4.5 MeV electron measurements from the Van Allen Probes/REPT instrument from early mission. (b-d) The solar wind speed, interplanetary magnetic field, and Dst index, respectively, for this same period. As evident from panel (d), three geomagnetic storms occur (~9/1, 9/30, and 10/9), each resulting in dramatically different responses in the outer radiation belt electrons. (From *Baker et al.*, 2013)

2.2.1 Acceleration Mechanisms

Two main electron acceleration mechanisms exist in the outer radiation belt: inward radial transport and local heating. By conserving the first and second adiabatic invariants, <u>radial transport</u> can energize electrons by moving them inward to smaller radial distances from Earth and thus into regions of increased magnetic field strength. This process can be accomplished via

large scale electric and magnetic field fluctuations at periods comparable to the electron drift period (~mHz for outer belt electrons) [*Falthammar*, 1965].

Local heating, on the other hand, occurs via wave-particle interactions that violate the first adiabatic invariant, causing local energy diffusion. Signatures of this acceleration mechanism have been identified by a peak in phase space density within the heart of the outer radiation belt, rather than a flat profile or gradient increasing outwards [e.g. *Green and Kivelson*, 2004; *Reeves et al.,* 2013]. Whistler mode chorus waves are a primary mechanism shown to cause substantial local heating [*Temerin et al.*, 1994; *Li et al.,* 1997]. As depicted in Figure 2.9, these waves are generated outside the plasmasphere on the dawn side (~midnight to noon) from the free energy provided by anisotropic ($T_\perp > T_\parallel$) keV electrons injected from the tail during
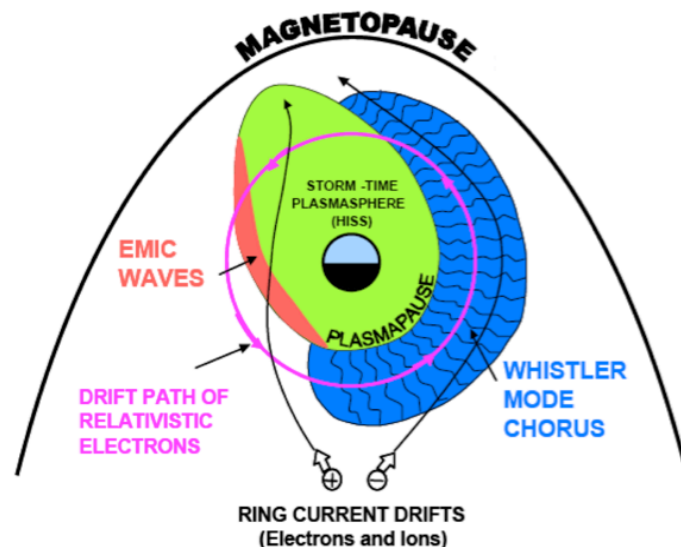
Figure 2.9 A cartoon schematic of the inner magnetosphere, looking down on the equatorial plane with the sun towards the top. A few of the primary wave modes important for the dynamics of outer radiation belt electrons are depicted, namely plasmaspheric hiss (green), whistler mode chorus (blue), and electromagnetic ion cyclotron (EMIC) waves (orange), in their expected regions of generation. These modes can all resonate with energetic electrons, causing energy as well as pitch angle diffusion. (Adapted from *Summers et al.,* 1998)

active times. With frequencies ranging from ~100Hz to 5 kHz (~0.1-0.8 Ω_e), these right-hand polarized waves often occur in discrete elements of rising or falling tones [*Li et al*., 2012] and are resonant with the gyrofrequency of energetic electrons (Ω_e).

2.2.2 Loss Mechanisms

A number of relativistic electron loss processes also exist in the inner magnetosphere, the primary ones being: magnetopause shadowing, outward radial diffusion, and precipitation into the atmosphere. <u>Magnetopause shadowing</u> occurs when the drift paths of energetic electrons intersect the magnetopause and are thus lost to this outer boundary. This mechanism has been shown to produce rapid loss often seen at outer edge of the radiation belt during the main phase of geomagnetic storms, under sharp pressure pulses in the solar wind [*Li et al.*, 1997; *Millan and Thorne*, 2007].

Similarly to inward radial diffusion described previously, <u>outward diffusion</u> can cause de-energization and further losses to the magnetopause by transporting electrons to regions of lower magnetic field strength. As the direction of radial diffusion (inward or outward) is determined by PSD gradients, a sharp decrease in the electron population at larger radial distances, due for example to magnetopause shadowing, can cause enhanced outward diffusion [*Shprits et al.*, 2006; *Turner et al.*, 2012].

Finally, <u>precipitation</u> of electrons into the atmosphere, as a result of pitch angle scattering into the loss cone, is another important loss process of radiation belt electrons. A number of different wave types can resonantly interact with MeV electrons, breaking their first invariant and scattering their pitch angles to small enough values that they collide with the atmosphere before mirroring back up the field line. Hiss, whistler mode chorus, and electromagnetic ion cyclotron (EMIC) waves, all illustrated in Figure 2.9 in their respective generation regions, can

contribute to precipitation losses in this way. Plasmaspheric hiss, concentrated within the cold, high-density plasma region of the inner magnetosphere, is a broadband whistler mode wave with frequencies ranging from ~100Hz – few kHz. This wave mode can precipitate electrons at low L shells and has been accredited for creation of the slot region between the inner and outer radiation belts [*Lyons and Thorne*, 1973]. Whistler mode chorus waves, mentioned previously as a source of energy diffusion and local acceleration, can also cause pitch angle diffusion. As both a potential acceleration and loss mechanism, these waves will be discussed in more detail in Chapter 5. Finally, EMIC waves range from ~0.1 – 5Hz and appear at frequencies below and approaching the local proton gyrofrequency (Ω_p), typically with stopbands at the 0^+, He^+, and H^+ gyrofrequencies. These waves, generated by anisotropic ($T_\perp > T_\parallel$) keV ions as they drift across the dusk sector, can also resonate with MeV electrons, causing pitch angle scattering and loss. These waves will be discussed in more detail in Chapters 3 and 4.

As demonstrated in Figure 2.9, the generation regions of these various wave modes, which can cause electron acceleration as well as loss, are highly dictated by location of the cold plasma population and plasmapause boundary. Additionally ring current particles often provide the free energy source for wave generation. The coupled nature of these diverse magnetospheric populations is apparent, as well as the important role electromagnetic waves play in the transfer of energy from one to the other.

2.3 Wave-Particle Interactions

Wave-particle interactions play a critical role in radiation belt dynamics, providing a source of both acceleration and loss of energetic electrons in the inner magnetosphere. A brief review is presented here of some of the basic physics behind resonant wave-particle interactions

leading both to energy diffusion as well as pitch angle scattering. In particular, we focus on waves resonant with the gyromotion of energetic electrons, which can change a particle's momentum as well as energy by breaking the first adiabatic invariant. The resonance condition governing this interaction can be written as:

$$\omega - k_{\|} v_{\|} = \frac{n\Omega}{\gamma} \tag{2.1}$$

where ω is the wave frequency, $k_{\|}$ and $v_{\|}$ the components of the wave vector and particle velocity, respectively, parallel to the background magnetic field, Ω the qyrofrequency of the particle, γ the relativistic factor, and n some integer multiple ($=0, \pm1, \pm2$, etc). For a particle approaching a wave of the same polarization and of frequency less than Ω, the wave frequency may be Doppler shifted upwards to match that of the particle. In this case, a particle in phase with the oscillating electric and magnetic fields of the wave can either lose or gain energy in both the perpendicular and parallel directions, causing either wave growth or damping and particle energization [*Tsurutani and Lakhina*, 1997]. This type of resonance can occur, for example, between right hand polarized (RHP) whistler mode chorus waves and electrons, which gyrate in the right-handed sense, as they propagate along a field line towards each other (Figure 2.10 depicts this same type of interaction between and ion and LHP wave).

Anomalous resonance, on the other hand, can cause interaction between waves and particles with oppositely handed polarizations. In this situation, as an electron (or ion) overtakes a LHP (RHP) wave, the wave polarization appears reversed in the reference frame of the particle, allowing resonance conditions to be met. EMIC wave resonance with MeV electrons is one example of this type of interaction [*Thorne and Kennel*, 1971].

These resonant interactions are often described as a diffusive process, where the net result after multiple interactions between many electrons and wave packets is to smooth out pitch angle

(Normal) Cyclotron Resonance

Wave-Particle (Cyclotron) Interaction
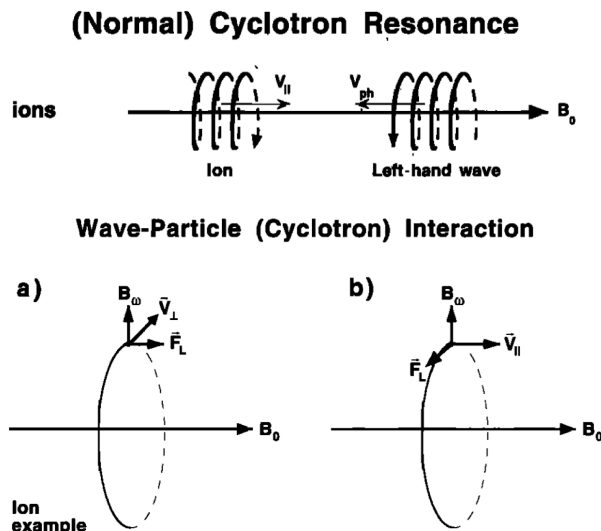
Figure 2.10 A schematic illustrating the interaction between gyroresonant waves and particles. The top panel illustrates a scenario resulting in normal cyclotron resonance, and the bottom panel shows how both the parallel and perpendicular velocities of the particle can be altered by the wave via the Lorentz force. (From *Tsurutani and Lakhina*, 1997)

and energy gradients. While this quasilinear diffusion formalism is not necessarily appropriate for large monochromatic waves, such as the large amplitude whistler mode waves first reported by *Cattell et al*. [2008], it has been shown to well represent the bulk electron behavior for a large number of wave types [*Thorne et al*., 2013].

2.4 Open Questions and Motivation

Above, we've described the variability of the outer radiation belt and outlined some of the key processes involved in causing enhancements and depletions of the energetic electrons trapped in this region. While much work has been done on these topics, critical open questions remain regarding the contribution of each of these processes to overall outer belt dynamics. When and where do losses dominate over acceleration mechanisms? What role does precipitation play in these losses, compared to magnetopause shadowing or outward radial diffusion? And what mechanisms or wave modes are primarily responsible for the precipitation?

In the following work, we investigate the contribution of wave-particle interactions and precipitation loss to the overall dynamics of the outer radiation belt.

Chapter 3: A Plasma-Based Proxy for EMIC Waves

The following chapter is based primarily on work that was published in Blum et al. (2012), A comparison of magnetic field measurements and a plasma-based proxy to infer EMIC wave distributions at geosynchronous orbit, *J. Geophys. Res., 117,* A05220.

3.1 Introduction

Plasma waves in Earth's inner magnetosphere can resonantly interact with trapped electrons and accelerate them to MeV energies as well as cause pitch angle diffusion and scatter them into the atmosphere. Theory has shown that electromagnetic ion cyclotron (EMIC) waves are one such source of pitch angle scattering and can thus cause electron precipitation and enhanced losses to the outer radiation belt [*Thorne and Kennel*, 1971]. EMIC waves are generated in the inner magnetosphere by anisotropic ($T_\perp > T_\parallel$) keV ion populations as the ions convect in from the tail and drift westward around Earth (e.g., *Anderson et al.*, 1996). Large anisotropies, as well as the presence of cool plasma, can produce enhanced EMIC wave growth [*Cornwall et al.*, 1970; *Horne and Thorne* 1993].

EMIC waves often occur in the afternoon sector where ring current ions overlap cool, dense plasmaspheric plumes [*Spasojevic et al.*, 2004]. A number of studies have examined the distributions of EMIC waves across local time and L shell using magnetometer measurements from a variety of satellites including CRRES, GOES, AMPTE CCE, and DE 1 (e.g., *Meredith et al.*, 2003; *Clausen et al.*, 2011; *Anderson et al.*, 1992; *Erlandson and Ukhorskiy*, 2001, respectively). In the inner magnetosphere, the waves are observed primarily on the dusk side, with occurrences peaking during the main phase of storms but often persisting into the recovery

phase as well [*Fraser and Nguyen*, 2001; *Bossen et al.*, 1976; *Halford et al.*, 2010]. While in situ EMIC measurements show strong wave activity during the main phase of storms, a relative absence is observed in ground measurements of Pc1-Pc2 waves during this storm phase [*Engebretson et al.*, 2008, *Posch et al.*, 2010].

EMIC waves are able to gyroresonate with both keV ions as well as MeV electrons, breaking the first adiabatic invariant and scattering the particles into the loss cone [*Albert*, 2003; *Summers and Thorne*, 2003]. In order to better quantify losses of radiation belt electrons due to EMIC waves, an understanding of the waves' global distributions is needed. As these waves are a localized phenomenon, multi-point measurements are necessary to accurately measure EMIC distributions and determine the spatial and temporal extent of the waves.

To enable better investigation of the spatial and temporal evolution of these waves, as well as their storm-time distributions, we develop a plasma-based proxy for EMIC wave activity based on Alfven-cyclotron instability theory [*Gary et al.*, 1994]. Using in situ plasma measurements from the Los Alamos National Laboratory (LANL) instruments onboard geosynchronous satellites, this EMIC proxy is calculated and compared to in situ wave measurements from the GOES satellites to investigate the accuracy and validity of such a proxy over local time and during varying levels of geomagnetic activity. We look both at single events, as well as statistical distributions, and compare the LANL proxy to GOES direct EMIC wave measurements. The proxy is found to correspond well with measured waves both statistically and for individual instances, demonstrating the value of plasma measurements to infer EMIC wave distributions. Subsequent studies have also investigated this proxy and these will be briefly described in Section 3.5.

3.2 Linear Theory and Proxy Development

Observations, theory, and simulations have established the following general picture for the interaction of anisotropic ion velocity distributions and enhanced EMIC fluctuations in space plasmas. Consider an idealized electron-proton collisionless plasma in which both species are represented by bi-Maxwellian velocity distributions. Consider the condition $T_{\perp p}/T_{\parallel p} > 1$, where the directional subscripts represent directions relative to the background magnetic field and "p" denotes protons. If this anisotropy is sufficiently large, it will excite growth of the electromagnetic proton cyclotron anisotropy instability [*Gary,* 1993]. The resulting enhanced EMIC fluctuations have maximum growth at $\mathbf{k x B_o = 0,}$ where $\mathbf{B_o}$ is the background magnetic field and $\mathbf{k}$ is the wave vector, with a range of frequencies $0 < \omega < \Omega_p$ where the latter symbol represents the proton cyclotron frequency. The fluctuations from this instability are further characterized by left-hand polarization and weak magnetic compressibility.

The enhanced fluctuations are resonant with and scatter the protons so as to reduce $T_{\perp p}/T_{\parallel p}$ and thereby quench the instability. As a result an upper bound is imposed upon the proton anisotropy, which can be written as

$$\frac{T_{\perp p}}{T_{\parallel p}} - 1 = \frac{S_p}{\beta_{\parallel p}^{\alpha_p}} \tag{3.1}$$

where $\beta_{\parallel p} = 8\pi n_p T_{\parallel p}/B_o^2$ and S_p and α_p are parameters which are obtained by a fit to the instability threshold condition derived from linear theory. For example, choosing the maximum growth rate to be $\gamma/\Omega_p = 10^{-3}$ yields $S_p = 0.43$ and $\alpha_p = 0.42$ for a fit over the range $0.01 \leq \beta_{\parallel p} \leq 10$ [*Gary et al.,* 1994].

In the terrestrial magnetosphere, observations show the existence of two or more distinct components in ion velocity distributions. Consider the idealized picture of two proton

components, one hot (denoted by subscript h) and one cool (subscript c). In the plasmasphere, $n_c \gg n_h$ and $T_{\|h} \gg T_{\|c}$; the cool component is relatively dense and collisional so that it is relatively isotropic. Beyond the plasmasphere, the cool component persists but at densities such that $n_c \sim n_h$. The presence of the cool component modifies the properties of the proton cyclotron instability so that the upper bound on the anisotropy is written as

$$\frac{T_{\perp h}}{T_{\|h}} - 1 = \frac{S_h}{\beta_{\|h}^{\alpha_h}} \tag{3.2}$$

where $\beta_{\|h} = 8\pi n_h T_{\|h}/B_o^2$ and S_h and α_h are fitting parameters which are functions of both γ/Ω_p and n_h/n_e, where n_e is the electron density, which we take to be equal to $n_h + n_c$ [*Gary et al., 1994*]. Equation 3.2 has the same form as Equation 3.1, namely that of a limiting temperature anisotropy, though the limit to the instability now has a more complex description. If we choose a fixed value of the maximum growth rate, we can then use linear theory to determine how these two fitting parameters vary with the relative hot proton density. Linear theory shows that both parameters are relatively weak functions of n_h/n_e. We have quantified this result by choosing the forms:

$$S_h = \sigma_0 + \sigma_1 \ln\left(n_h/n_e\right) + \sigma_2 \left[\ln\left(n_h/n_e\right)\right]^2 \tag{3.3a}$$

and

$$\alpha_h = a_0 - a_1 \ln\left(n_h/n_e\right) - a_2 \left[\ln\left(n_h/n_e\right)\right]^2 \tag{3.3b}$$

Then, assuming $\gamma/\Omega_p = 10^{-3}$, we fit linear theory results to these two curves, obtaining $\sigma_0 = 0.429$, $\sigma_1 = 0.124$, $\sigma_2 = 0.0118$, $a_0 = 0.409$, $a_1 = 0.0145$, and $a_2 = 0.00028$. Table 3.1 provides the values of the constants σ and a calculated for various other growth rates.

γ/Ω_p	σ_0	σ_1	σ_2	a_0	a_1	a_2
0.001	0.429	0.124	0.0118	0.409	0.0145	0.00028
0.004	0.535	0.171	0.0224	0.403	0.0215	0.00111
0.01	0.664	0.249	0.0438	0.403	00289	0.00229

Table 3.1 Values for constants σ and a in the expressions for fitting parameters S_h (Equation 3.3a) and α_h (Equation 3.3b), calculated for three different local temporal growth rates γ/Ω_p.

The most direct determination of EMIC wave activity in space plasmas is through the use of spacecraft magnetometers, which measure the level of magnetic fluctuations near and below the proton cyclotron frequency. However, the plasma data described below is obtained from LANL spacecraft that do not carry magnetometers; thus we have developed a procedure, similar to *MacDonald et al.* [2008] for whistler waves, whereby theory and plasma observations become a proxy for direct measurements of wave activity.

The procedure is as follows: we define the observational EMIC parameter

$$\Sigma_h = \left(\frac{T_{\perp h}}{T_{\parallel h}} - 1\right)\beta_{\parallel h}^{\alpha_h} \tag{3.4}$$

where $T_{\perp h}$, $T_{\parallel h}$, and n_h are measured by the plasma instrument, α_h is determined via Equation 3.3b using measured values of n_h/n_e, and the background magnetic field B_o necessary to calculate $\beta_{\parallel h}$ is taken from the T89 magnetic field model [*Tysganenko*, 1989]. As α_h is a very weak function of γ/Ω_p, we use the expression for α_h associated with $\gamma/\Omega_p = 10^{-3}$ in all calculations of Σ_h. If we then plot experimental values of Σ_h as a function of the relative hot proton density, those values can be compared against the theoretical expression for the threshold S_h given as Equation 3.3a. If $\Sigma_h < S_h$ for a measurement time interval, it is likely that the hot protons are not

sufficiently anisotropic to excite the Alfven-cyclotron instability at the prescribed growth rate.
In contrast, if the observations yield $\Sigma_h > S_h$, it is likely that this mode is unstable during the measurement. Thus a comparison of the two quantities Σ_h and S_h becomes a proxy for determining the level of enhanced EMIC wave activity. We expect that the choice of an appropriate value of the maximum growth rate will yield an S_h which provides a statistical upper bound on the observed Σ_h. The growth rate needed to bound the observed anisotropies should be an indication of how strongly the instability is driven. Where $\Sigma_h=S_h$ for a given temporal growth rate γ, wave growth at this rate is expected. To help visualize these expressions, Figure 3.1 shows the dependence of this Σ_h-S_h value on density ratio n_h/n_e and hot plasma beta $\beta_{\|h}$ for γ=0.001 for three different temperature anisotropies (defined as $A_{hp}=T_{\perp h}/T_{\|h}$ -1).
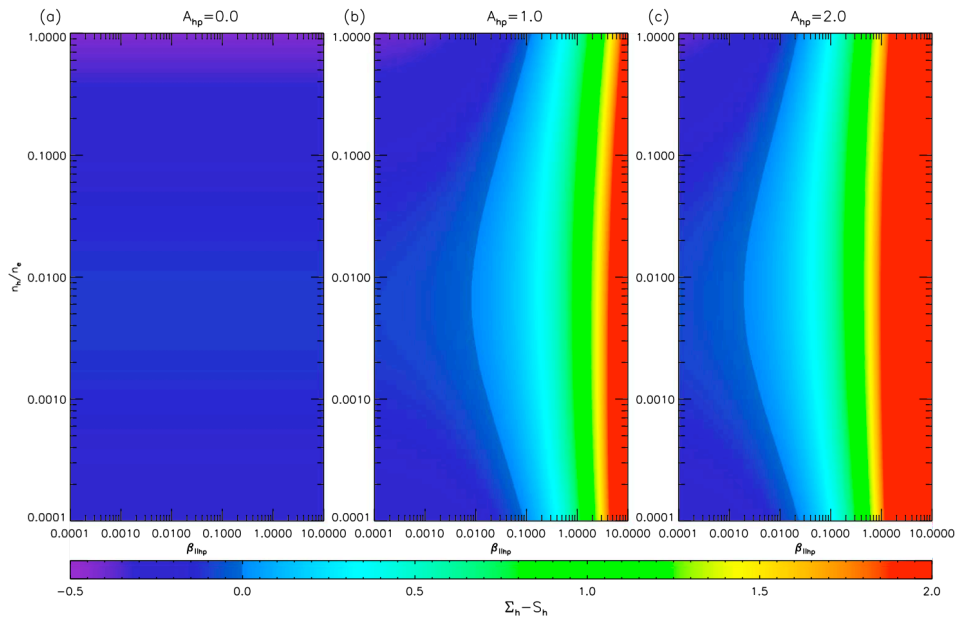
Figure 3.1 Contours of Σ_h-S_h in the $\beta_{\|h}$ − n_h/n_e plane for three temperature anisotropy values and a constant =0.001. (From *Lin et al.*, 2014)

This proxy is further developed to calculate physical wave characteristics and enable a more quantitative comparison to direct wave measurements. Using S_h expressions for γ/Ω_p

=0.001, 0.004, and 0.01, and interpolating linearly between these values, a γ value is found for each Σ_h measurement such that $\Sigma_h = S_h(\gamma/\Omega_p)$. Next, using the warm plasma dispersion relation and following Equation (4) of *Kozyra et al.* [1984], the group velocity is calculated, and thus the convective growth rate (γ/v_g) for the waves. Following *Jordanova et al.* [1997] and *Chen et al.* [2009], the path-integrated gain G is calculated in decibels by integrating the convective growth rate along the source region of the field line:

$$G = 20\log_{10} e^{\int_{\lambda_1}^{\lambda_2} \gamma/v_g \, ds} \tag{3.5}$$

where λ_1 and λ_2 are the lower and upper limits of the source region. We assume parallel propagating waves, a dipole magnetic field, the source region to be +/- 10° magnetic latitude, and the growth rate and group velocity to be constant within this region.

Finally, we adopt the simple scaling model used by *Jordanova et al.* [2001] to compute a wave amplitude B_w:

$$B_w = B_{sat} \times 10^{(G - G_{max})/G_{min}} \tag{3.6}$$

where B_{sat} is the saturation amplitude of the waves, G_{max} is a maximum gain, above which saturation is assumed, and G_{min} the minimum gain, below which growth and wave-particle scattering is considered to be negligible. Comparing to statistical studies of EMIC wave amplitudes, which typically measure waves to be ~1-3 nT in the inner magnetosphere, with a maximum observed magnitude ~10 nT [*Erlandson and Ukhorskiy*, 2001; *Anderson et al.*, 1992], we set B_{sat}=10 nT, G_{min}=13.3 (equivalent to an amplitude of 0.1 nT), and G_{max}=40 (10 nT). Below this G_{min} value, waves drop below magnitudes detectable by the GOES spacecraft. To better match wave amplitudes measured by GOES, our selections for these values differ from

those used by *Jordanova et al.*, [2001], who takes G_{min}=20 and G_{max}=60. While this amplitude calculation includes a number of assumptions, it allows for estimation of physical wave characteristics, for quantitative comparison to the wave measurements themselves. We discuss the implications of these assumptions in more detail in the Section 3.4.2.

3.3 Proxy Validation: Observations

LANL data from geosynchronous orbit are used to investigate the the in situ plasma conditions during a set of events. Using the Magnetospheric Plasma Analyzer (MPA) instrument, bulk moments are obtained for the density of cool ions (defined as <100 eV), the density of warm ions (100 eV – 45 keV), as well as the warm ion temperature both parallel and perpendicular to the background magnetic field ($T_{\parallel}$ and $T_{\perp}$, respectively). As MPA cannot distinguish among ion species, a pure proton population is assumed. The background magnetic field direction is inferred from symmetry in the plasma distributions [*Thomsen et al.*, 1999]. The T89 magnetic field model is used to calculate the magnitude of the background field B_o.

The inferred waves are compared to wave measurements taken by the GOES satellites, also at geosynchronous orbit. Using 0.512-second high-resolution magnetometer data, re-sampled at a constant resolution of 0.6 s, dynamic spectra are computed for all three magnetic field components using a Fast-Fourier Transform (FFT) with a 1 hour window, advanced in 20 minute steps, following the analysis performed by *Clausen et al.* [2011]. The instrument response is suppressed for frequencies between 0.5 – 1.0 Hz, so only EMIC waves with amplitudes > 1 nT are resolvable up to ~0.8 Hz, and amplitudes > 0.1 nT below 0.5 Hz [*Fraser et al.*, 2010]. This enables identification of waves in the He^+ and O^+ bands, and the lower portion of the H^+ band. To automate identification of EMIC waves from the spectrograms, an

algorithm developed and described by *Clausen et al.* [2011] is employed. This algorithm selects waves between 0.1 - 0.8 Hz, with total power spectral density in the transverse components greater than 10 nT^2/Hz above the background noise lasting 15 minutes or more. Figure 3.2 demonstrates the output of this algorithm for a single day of GOES data, where the red boxes indicate EMIC wave selections.
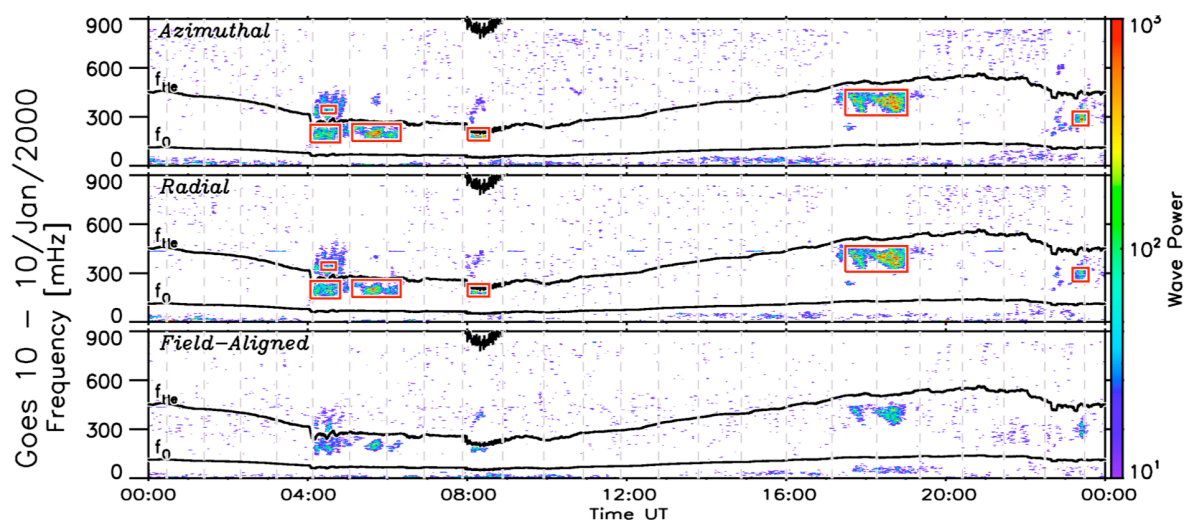
Figure 3.2 Spectrograms of GOES 0.512 s magnetometer data. Wave powers are shown in the azimuthal, radial, and field-aligned directions, with respect to the background magnetic field. Red boxes indicate activity identified as EMIC waves, as selected by the *Clausen et al.* [2011] algorithm.

Using these data sets, we perform both single event comparisons as well as a superposed epoch study of 52 events. For the statistical study, a set of energetic electron flux dropouts taken from *Green et al.* [2004] is used, where events were chosen based on a decrease in the >2 MeV electron flux, as measured by GOES, by a factor of 100 or greater when compared to the flux on the previous day. On average, these events show a dip in Dst reaching a minimum of -40 nT in the day following dropout onset (zero epoch). Solar wind conditions and geomagnetic indices during these events are shown in Figure 3.3. While *Green et al.* [2004] looked at these events to investigate the potential causes of the relativistic electron dropouts, they are used here as a

convenient event list for which both LANL and high-resolution GOES data are available. Investigation of the link between the waves and the radiation belt flux dropouts is not the focus of the present study. Below, we first present GOES and LANL data from a single day during one such dropout event, and then place it in the larger context of the statistical study.
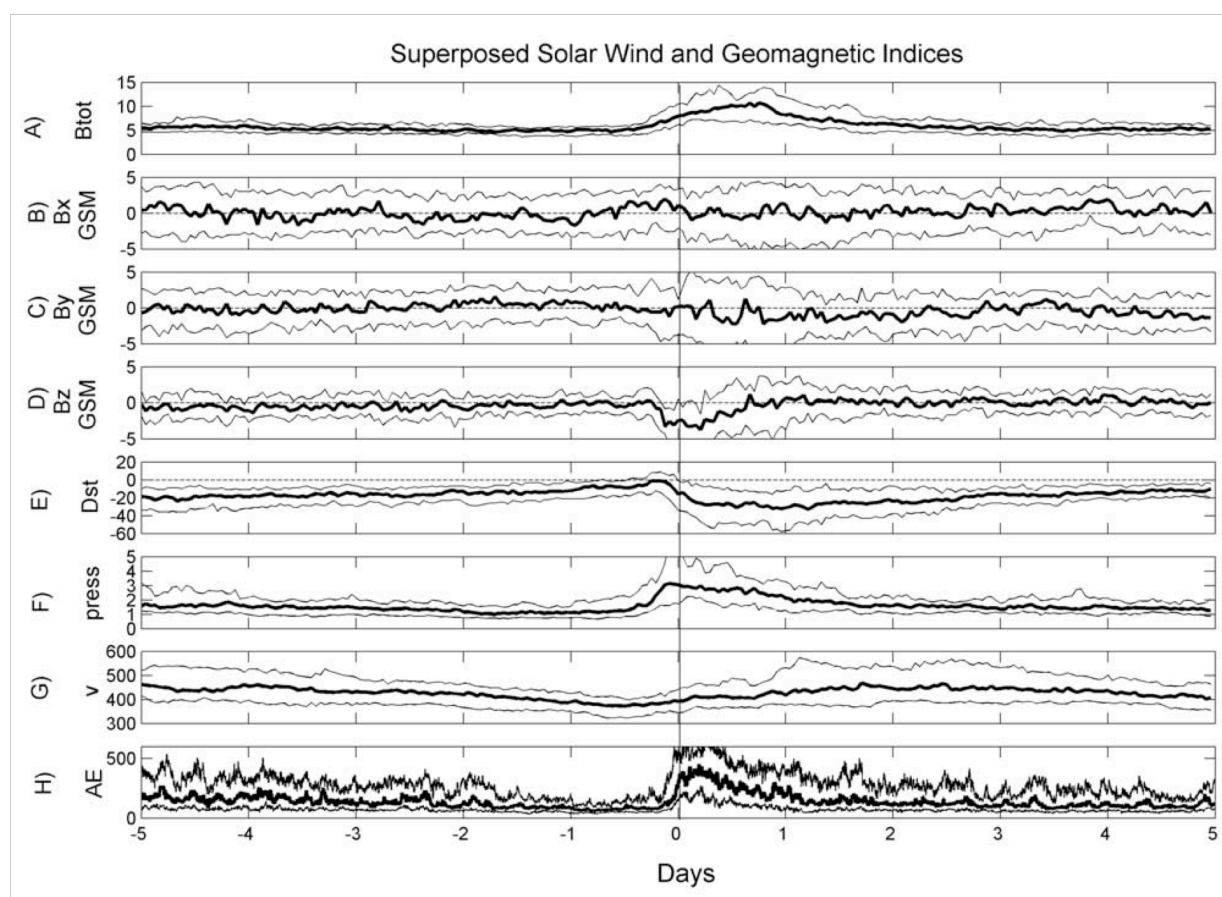
Figure 3.3 Superposed solar wind conditions and geomagnetic indices during the 52 dropout events investigated here. (From *Green et al*., 2004)

3.3.1 January 10th, 2000

Data are presented from the GOES 10 and LANL-89 (1989-046) satellites for one such event on January 10th, 2000, where LANL-89 trails GOES by 2 hours. This dropout event, with zero epoch occurring at 5 UT, takes place just prior to the onset of a geomagnetic storm, with minimum Dst reaching -81 nT on January 11 around 22 UT. This day is selected for comparison

because GOES detects EMIC waves at 5 distinct times throughout the day; we investigate the accuracy of the plasma-based proxy for each of these instances of wave activity, which are distributed across a range of local times. On the 10th, EMIC waves are measured first by GOES at 4 UT, followed by subsequent bursts at roughly 5, 8, 17:30, and 23:10 UT (see Figure 3.2).

The various plasma parameters measured by LANL MPA and used to calculate the EMIC proxy are presented in Figure 3.4. Figure 3.4a shows the cool plasma density, enhancements indicating crossings into plasmaspheric bulge or plume regions. In Figure 3.4b, we show hot proton density, and in c the hot proton temperature anisotropy, defined as $T_{\perp h}/T_{\|h}-1$. Elevated anisotropies, concurrent with enhanced cool and hot plasma densities, combine to create four separate times where the proxy exceeds the instability threshold for a growth rate $\gamma/\Omega_p = 10^{-3}$ (Figure 3.4d). For these times, the wave amplitude is calculated (Figure 3.4e) following the steps previously outlined in Section 3.2. Below this panel, in Figure 3.4f, average amplitudes of the EMIC waves measured by GOES 10 are shown. GOES amplitudes are approximated by calculating the square root of the wave power, integrated over the frequency range of the activity as identified by the *Clausen et al*. [2011] algorithm described in Section 3.3. When waves in multiple bands are detected simultaneously (e.g., 4-5 UT), the average amplitude of the two wave bursts is calculated, as the LANL EMIC proxy does not distinguish the exact frequency of the EMIC activity it infers. Simultaneous waves in multiple bands are measured relatively infrequently (during roughly 2% of the GOES wave detections) so we do not expect this to greatly affect our statistical results. From Figure 3.4e and f, it is evident that each EMIC wave burst measured by GOES 10 is subsequently detected in the LANL-89 data.
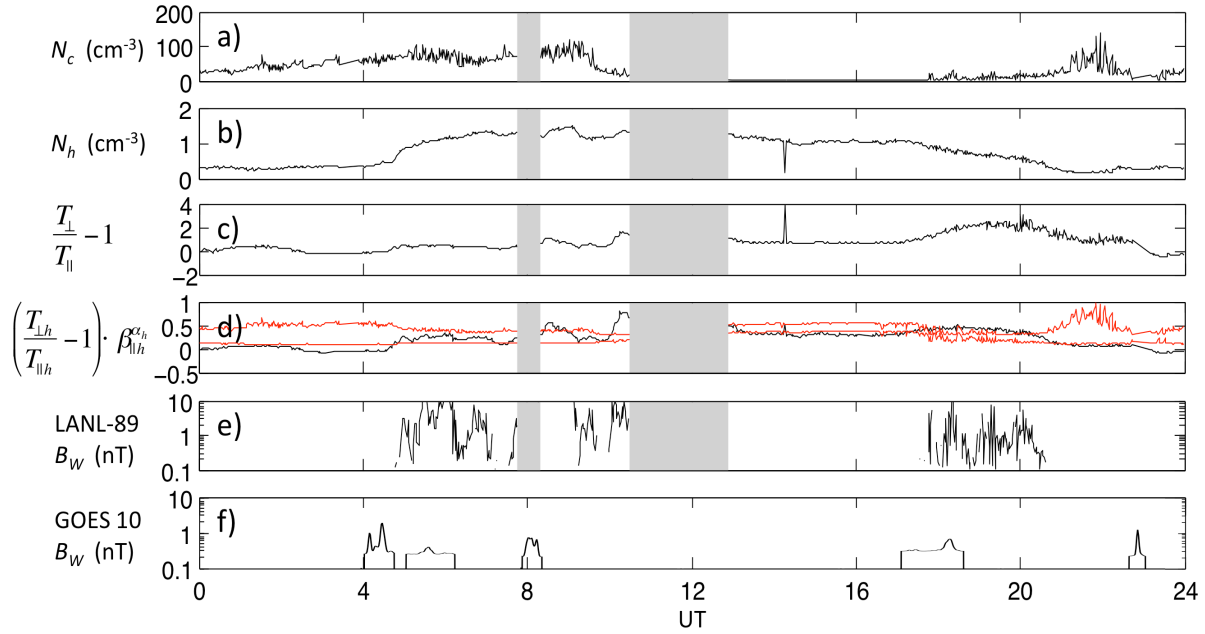
Figure 3.4 LANL-89 MPA data for 10 January 2000. (a) Cool proton density, (b) hot proton density, and (c) hot proton anisotropy are shown versus universal time (UT). (d) The EMIC wave proxy Σ_h in black, calculated following equation (3.4). We have included calculations of the theoretical instability threshold S_h for local growth rates of 10^{-3} (lower red line) and 10^{-2} (upper red line), following equation (3.3a) and using values found in Table 3.1. The instability threshold for a growth rate of $\gamma/\Omega_p = 10^{-3}$ is exceeded at four different instances. Grey-shaded regions are periods where MPA data are unavailable. (e) The calculated wave amplitude during the four times when the threshold is exceeded. (f) The EMIC wave amplitudes measured by GOES 10 are presented for comparison.

3.3.2 52 Event Superposed Epoch Study

The LANL spacecraft are not equipped with field measurements, and GOES 8, 9, and 10 do not provide the necessary plasma parameters to calculate the EMIC proxy. Thus, the conclusions drawn from single event comparisons of wave amplitude are limited by the physical separation of the spacecraft. Therefore, we perform a superposed epoch study of 52 relativistic electron flux dropout events and compare EMIC wave distributions across both local and epoch times. Following *Green et al.* [2004], events are superposed to align the onsets of the electron dropouts, where zero epoch is set to the time when the >2 MeV electron flux drops by a factor of two as compared to the flux level on the previous day. On average, minimum Dst falls within

one day after zero epoch and a small storm sudden commencement (SSC) is observed just before zero epoch, so for events associated with storms, the dropouts occur primarily during the main phase (see Figure 3.3). There is also, on average, an increase in AE activity coinciding with zero epoch. These events are often preceded by increased solar wind dynamic pressure and a southward turning of the interplanetary magnetic field [*Green et al.*, 2004].

Figure 3.5 shows normalized occurrence rates of both the plasma-based LANL proxy (Figure 3.5a), as well as the GOES EMIC wave measurements (Figure 3.5b). The LANL data
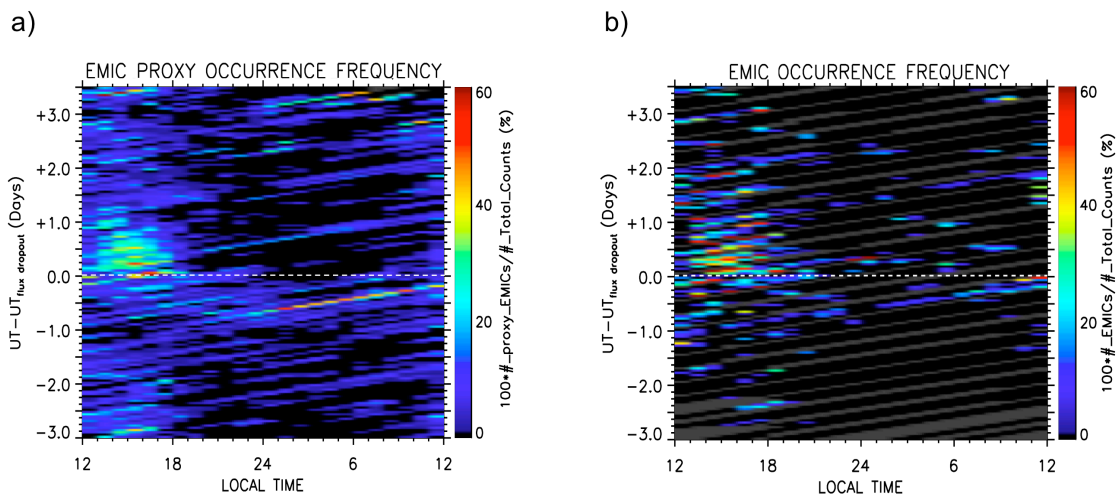
Figure 3.5 Distributions of EMIC wave occurrences over local and epoch times from (a) the plasma-based proxy from LANL MPA data and (b) wave measurements from GOES. The color bar indicates normalized occurrence rates in hourly time bins.

set utilizes measurements from 6 spacecraft distributed in local time, while GOES includes data from the GOES 8, 9, and 10 spacecraft depending on availability. For each dataset, the number of measurements made during EMIC activity (measured or inferred), divided by the total number of measurements in that time bin, is plotted. Data is divided into hourly bins, and average values within each bin are plotted; grey bins indicate times with no data. We choose a minimum amplitude of 0.1 nT for the lower threshold of the LANL proxy, to best match the GOES

instrument sensitivity. Here, the proxy and wave measurements agree well qualitatively across both local and epoch time. The majority of EMIC waves, ~65% of those measured by GOES and 69% inferred by LANL, occur between 12 and 18 MLT, in agreement with other statistical EMIC observations from CRRES [*Meredith et al.*, 2003] and GOES [*Clausen et al.*, 2011].

3.4 Proxy Validation: Discussion

3.4.1 EMIC Wave Occurrence Rate Comparison

We return to the case study previously presented to validate the proxy for individual events, with the caveat that wave characteristics may be varying in the two hours of local time between GOES 10 and LANL-89. Figure 3.4 shows the plasma conditions combining to exceed the local instability threshold and incite EMIC wave activity at 4 times throughout the day, each slightly later in universal time than the wave activity detected by GOES 10. The first two periods of wave activity detected by LANL (just after 4 UT through ~9:30 UT) occur during periods of enhanced cool plasma as the satellite passes through the dusk sector. In contrast, the fourth occurrence of EMIC activity, beginning at LANL-89 around 17:30 UT, occurs on the morning side, where cool plasma density remains low but hot ion anisotropy is enhanced. At ~ 21 UT, as cool plasma density increases again, the hot plasma density drops to very low values, elevating the instability threshold (Figure 3.4d) and making wave growth more difficult. Both cool plasma enhancements, as well as a large enough source population of hot ions, are needed to exceed the instability threshold and incite EMIC waves. We see the EMIC instability excited under various plasma conditions across a range of local times, in good agreement with observed

EMIC waves. This case study demonstrates the validity of the plasma-based proxy across local times, and for a variety of plasma parameters that combine to trigger the instability.

Figure 3.6 compares the statistical occurrence rates of the plasma-based proxy and EMIC wave measurements as a function of local and epoch time by averaging the occurrence frequencies from Figure 3.5 across epoch (Figure 3.6a) as well as a range of local times (Figure 3.6b, c, d, and e). Figure 3.6a shows the distribution of LANL and GOES measurements across local time, and demonstrates the coherence between the proxy and wave occurrences over local
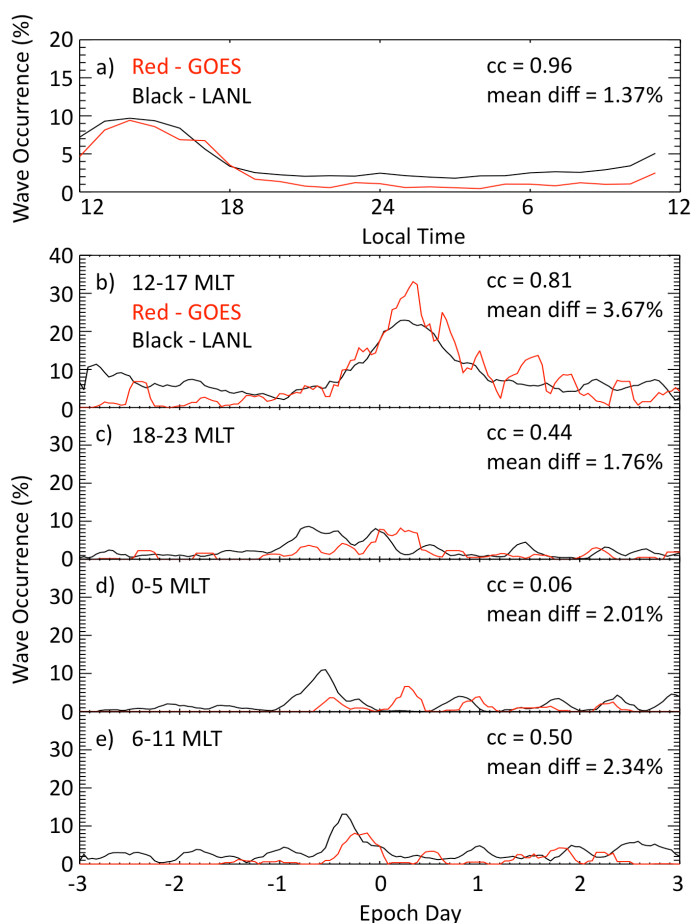
Figure 3.6 Smoothed occurrence frequencies of GOES EMIC wave measurements (red) and the LANL EMIC proxy (black) versus (a) local time and (b–e) epoch time. (a) the distribution of waves over local time, averaged across all epoch days. (b–e) average occurrence rates across four local time sectors to show variation over epoch time. The measurements show agreement in both overall shape and magnitude. Mean differences as well as linear correlation coefficients between LANL and GOES occurrence rates are calculated for each panel.

time. There is a strong peak in both LANL and GOES from ~12 to 18 MLT, with a linear correlation coefficient of 0.96 between the two, and a mean difference over all local times of 1.37%. At local times beyond this peak, somewhat larger wave occurrences exist in the LANL proxy than in GOES. These slightly elevated LANL values are also revealed when comparing across epoch time for various MLTs (see Figure 3.6b, c, d, and e). This suggests that the plasma instability may be triggered without exciting EMIC waves of large enough amplitude for detection by GOES.

We focus on Figure 3.6b, which averages EMIC occurrences from 12 through 17 MLT, as this is the region in which the majority of the waves occur. Occurrence rates are elevated in both the LANL proxy and the GOES data beginning half a day before the onset of the dropouts and extending one day following, with a peak just after zero epoch. Peak occurrence rates reach 20-30%, with a linear correlation coefficient of 0.81 and mean difference of 3.7% between the LANL proxy and GOES data. For events in this data set associated with storms, this occurrence peak falls in the main phase of the storms, consistent with other in situ measurements of EMIC waves but not necessarily with those from the ground [*Halford et al*., 2010; *Engebretson et al*., 2008]. As is evident from Figure 3.5, the greater coverage of the LANL satellites, both over time and longitude, provides an excellent database to draw from for statistical EMIC wave studies. Using the extensive LANL MPA database, it is possible to supplement current wave measurements and form a global picture of EMIC wave distributions at geosynchronous orbit during a variety of geomagnetic conditions.

3.4.2 EMIC Wave Amplitude Comparison

Next we discuss the wave amplitude calculation and compare the resulting inferred wave amplitudes to those measured by GOES. As mentioned in Section 3.2, we use a source region of +/- 10° magnetic latitude, as was used by *Jordanova et al.* [1997]. This is consistent with EMIC measurements from the CRRES satellite which indicate a source region constrained within +/- 11° magnetic latitude [*Loto'aniu et al.*, 2005]. However, the proxy wave amplitude calculation is fairly sensitive to this assumption (a region of +/- 5° produces a wave gain roughly half as large as that for +/- 10°), so while our source region choice is accurate statistically, it may be a source of uncertainty in gain, and thus wave magnitude, calculations for individual wave events.

Additionally, we scale G_{min}=13.3 to a wave amplitude of 0.1 nT, rather than the G_{min}=20 used by *Jordanova et al.* [2001]. When using G_{min}=20, there were far lower occurrence rates in the LANL data than the GOES, indicating that events with G<20 were still able to incite EMIC wave growth. The G_{min} and G_{max} values used here are tuned to identify these smaller amplitude waves, and agree well with observations as well as theoretical calculations by *Bortnik et al.* [2011] for waves in the few nT range. However, the sensitivity of the scaling model (Equation 3.6) to larger gain values causes small increases in gain to result in large amplitude enhancements, potentially overestimating wave amplitudes at the upper end of the gain scale. As seen from the LANL amplitudes calculated for January 10th in Figure 3.4e, the proxy saturates on a number of occasions while the GOES measurements remain below ~2 nT. Measurements of >10 nT EMIC waves appear relatively rarely in the GOES data. We choose to use these lower G_{min} and G_{max} values of 13.3 and 40, respectively, in order to calculate accurate

occurrence rates, despite the likely larger-than-realistic amplification of values at the upper end of the measurements.

Figure 3.7 compares average wave amplitudes, measured and inferred, across both local and epoch time. As was done in Figure 3.6, the mean wave amplitudes in each hourly bin are now averaged across epoch time (Figure 3.7a) and local time (Figure 3.7b) to enable quantitative comparison of the LANL predicted amplitudes to those measured by GOES. Only bins where waves are detected are taken into consideration, so the GOES data is sparser, as can be seen in Figure 3.7b. The GOES data here also show more scatter around the mean, most likely due to fewer data points from the 2 GOES satellites when compared to all 6 of the LANL. As GOES wave occurrence rates are 0% for a number of hourly bins across the night and morning side, Figure 3.7b is not subdivided into four local time sectors, as was done in Figure 3.6. No obvious trends in variation in average amplitude are exhibited in relation to either epoch or local time,
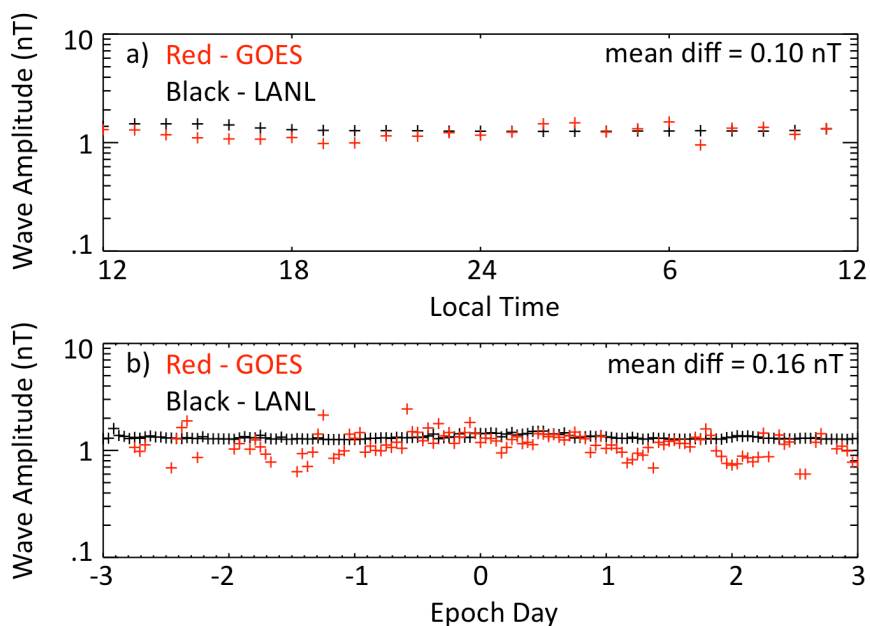
Figure 3.7 Average wave amplitudes measured by GOES (red) and calculated from the LANL EMIC proxy (black) across local and epoch time. No significant trends in amplitude variation as functions of either variable are observed. Average amplitudes calculated from LANL agree well with those measured by GOES.

and the average magnitudes of the GOES and LANL measurements are very similar. The total distribution of wave amplitudes is also computed for all GOES wave detections as well as LANL proxy calculations, and distribution properties are compared. The mean amplitude measured by GOES across all local and epoch times is 1.12 nT, with a standard deviation of 0.43 nT, while the mean amplitude of waves inferred by LANL equals 1.13 nT, with a standard deviation of 1.6 nT. The average values agree well, as is also seen in Figure 3.7. The larger standard deviation in the LANL inferred wave amplitudes may be due to a greater sensitivity of the proxy to low amplitude waves as compared to the GOES instrument response, as well as to potential amplitude overestimation for events at the upper end of the gain range, as discussed earlier.

3.5 Additional Proxy Applications

This plasma-based proxy has also been compared to various other measures of EMIC wave activity. As EMIC waves are known to resonate with and scatter keV ions as well as MeV electrons (e.g. *Carson et al.*, 2012), we have also compared proton aurora to this EMIC proxy. In *Spasojevic et al.* [2011], we look at events such as the one shown in Figure 3.8, during which a localized subauroral proton arc is observed by the Far Ultraviolet (FUV) Spectrographic Imager (SI) [*Mende et al.,* 2000] onboard the IMAGE satellite [*Burch,* 2000]. When mapped along magnetic field lines to the equatorial plane, this proton aurora falls within a plasmaspheric plume in the afternoon sector, where the plasmapause has been determined from the IMAGE Extreme Ultraviolet (EUV) instrument following *Goldstein et al.,* [2003].

During the July 31 2001 event pictured in Figure 3.8, two LANL spacecraft were at locations whose footpoints mapped to within the proton aurora (see Figure 3.9). The plasma conditions at these two geostationary spacecraft are investigated and the plasma-based EMIC
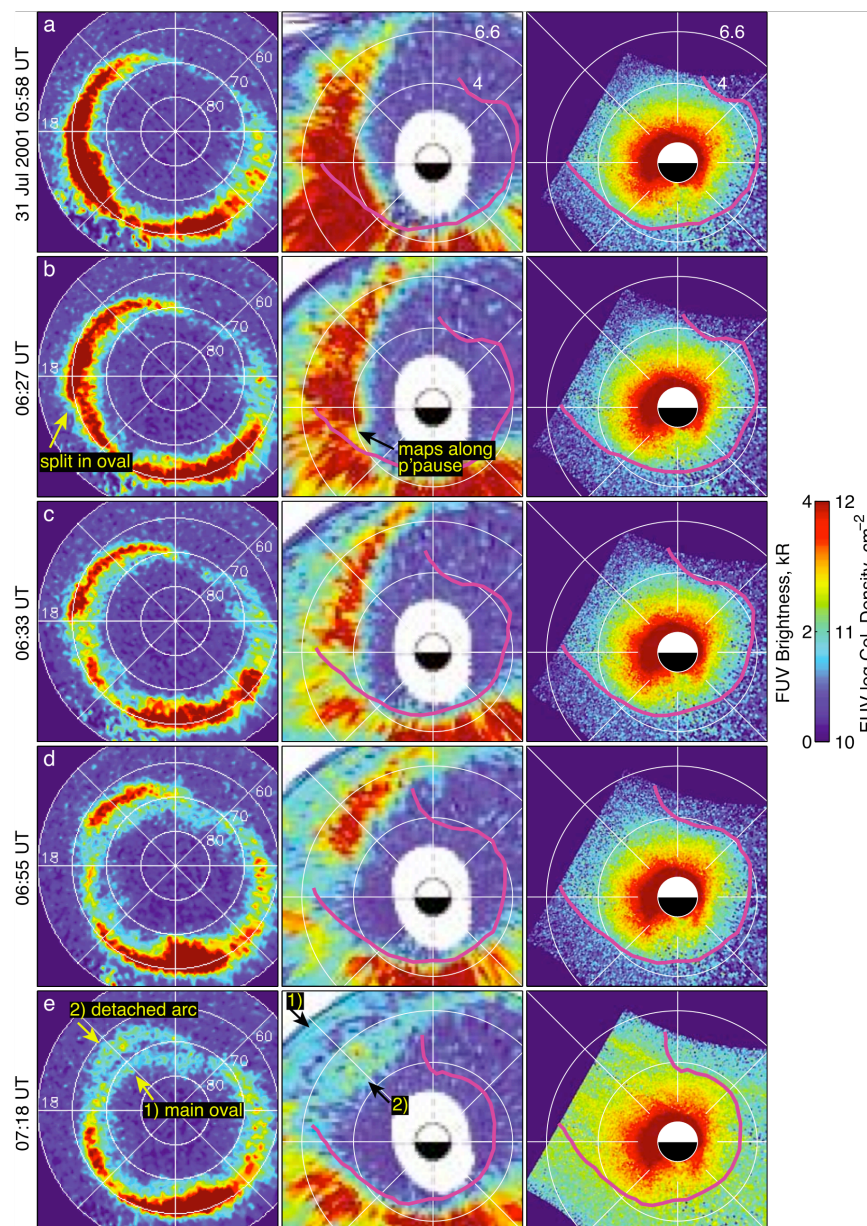
Figure 3.8 (a-e) A sequence of FUV SI12 proton aurora and EUV plasmasphere images for an event on July 31 2001. The left panel is the FUV SI12 image mapped to the ionosphere in magnetic APEX coordinates. The middle panel is that same image mapped along geomagnetic field lines, using the T96 magnetic field model and prevailing solar wind conditions, to the GSM equatorial plane. The right panel is the closest-in-time EUV image mapped to the equatorial plane. The location of the plasmapause is indicated by the magenta line. Noon is to the top in all images. In panel (e), the EUV image is contaminated by high background and column density values are invalid. (From *Spasojevic and Fuselier*, 2009)

proxy and estimated wave amplitude calculated, following the technique described in Section 3.2. Figure 3.10 shows the various plasma parameters as well as inferred wave amplitude calculated at satellite 1994-084 (green) and LANL-97a (magenta). Figure 3.10f shows the mean FUV brightness in a 300 km circle around the magnetic footprint of the spacecraft as detected by
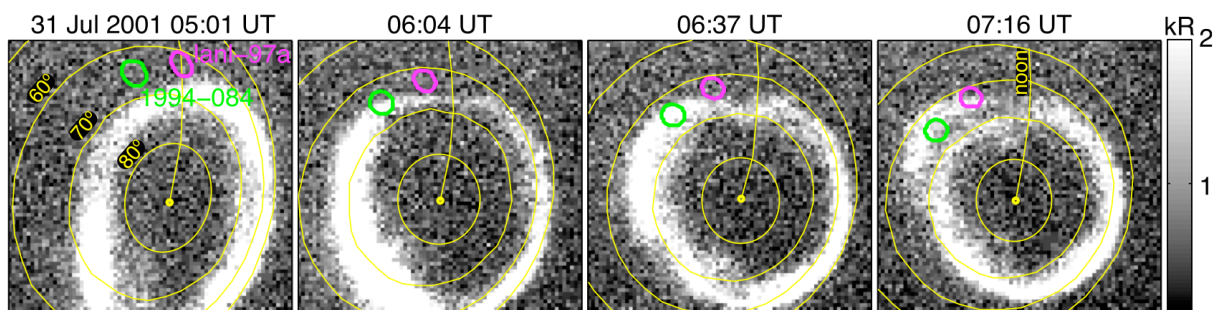
Figure 3.9 Sequence of IMAGE FUV SI12 images of the proton aurora along with 300-km circles drawn around the magnetic field line footprint of the geostationary spacecraft 1994-084 and lanl-97a. The latitude circles are geomagnetic and the 12 MLT meridian is indicated. These times correspond to the dashed vertical lines in Figure 3.10 below. (From *Spasojevic et al.*, 2011)

the IMAGE FUV SI12 instrument. Vertical dashed lines correspond to the times of FUV images shown in Figure 3.9. For the events presented in *Spasojevic et al*. [2011], good correspondence between proxy predictions of EMIC growth and proton precipitation within the field line footprint were found. A relationship between precipitation and wave intensity (rather than just wave growth rate) is expected since in treating the wave-particle interaction as a quasi-linear process, the pitch angle diffusion rate is a function of wave amplitude [*Kennel and Petschek*, 1966]. The agreement between wave amplitude and FUV brightness is, of course, not perfect, demonstrating the uncertainty associated with using either of these measures to infer the wave distribution; however, given the considerable number of assumptions upon which the proxy and wave amplitude predictions are based and the challenges in comparing those quantities to data from the ionospheric footprint, the correspondence between the proxy predictions and FUV

brightness is fairly impressive. These results demonstrate the efficacy of proxy measures, as well as the ability to combine them to separate spatial and temporal changes in global EMIC wave patterns.
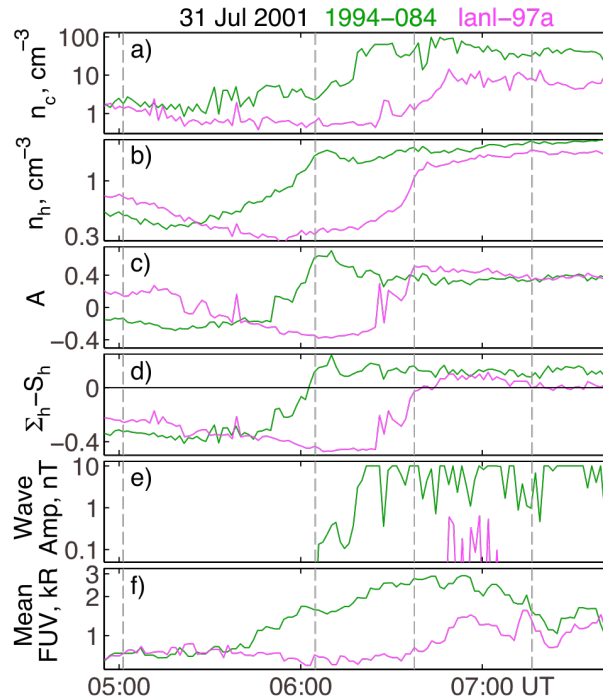
Figure 3.10 For geostationary spacecraft 1994-084 (green) and LANL-97a (magenta): (a) cool (1-100 eV/q) ion density (log scale), (b) hot (0.1-45 keV/q) ion density (log scale), (c) hot ion temperature anisotropy, A=T$_{\perp h}$/T$_{\| h}$ - 1, (d) EMIC wave proxy, Σ_h - S_h, (e) estimated EMIC wave amplitude (log scale), and (f) mean FUV brightness in a 300 km circle around the magnetic footprint of the spacecraft as detected by the IMAGE FUV SI12 instrument (log scale). The vertical dashed lines correspond to the times of the FUV images in Figure 3.9. (From *Spasojevic et al.*, 2011)

This plasma-based EMIC proxy has also been investigated in numerous other studies. *Chen et al*. [2014] find good agreement among GOES measured EMIC waves, LANL inferred EMIC waves, as well as wave growth simulated with the kinetic ring current-atmosphere interactions model with self-consistent magnetic field (RAM-SCB) and a ray-tracing code (HOTRAY). Figure 3.11 shows an event on June 8th 2001 comparing the modeled waves (black), GOES waves (pink and cyan) and LANL proxy $\Sigma_h > S_h$ (green, blue, orange). Dots along the spacecraft trajectories indicate measured and inferred EMIC wave activity, occurring

~12-18 MLT and persisting >10 hours during this event. These studies demonstrate the numerous applications of such a plasma-based proxy for EMIC wave activity, in combination with models, wave measurements, and particle precipitation.
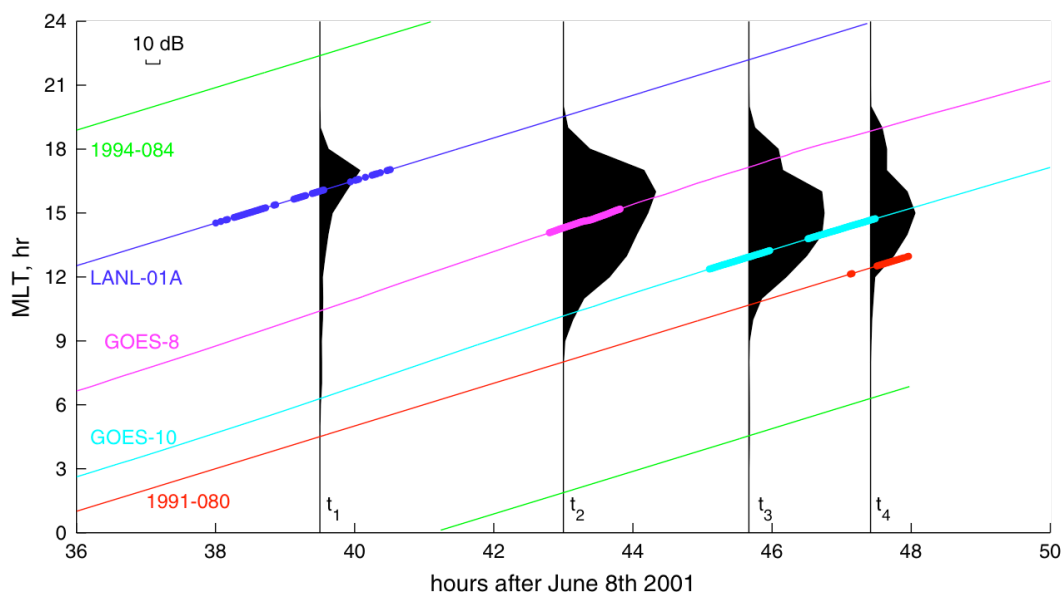
Figure 3.11 Comparison between EMIC wave observations and simulated maximum wave gain along trajectories of geosynchronous orbiting satellites as a function of UT and MLT. The dot points along the trajectories denote either observation or proxy of EMIC wave event. Four shaded areas represent the MLT distribution of maximum wave path-integrated over all the frequency bands at the selected UTs, with scale of 10 dB shown in the upper left corner. (From *Chen et al.*, 2014)

3.6 Summary

Based on quasi-linear theory and LANL/MPA observations, we have developed a plasma-based proxy to estimate the occurrence as well as amplitude of EMIC waves in the inner magnetosphere. This proxy is derived from warm (keV) ion temperature anisotropy and warm and cool ion population densities as measured by the MPA instruments at geosynchronous orbit.

To validate the use of this proxy, EMIC wave measurements from the GOES satellites are compared to the plasma-based proxy as measured by LANL satellites. We investigate the correspondence between the plasma-based proxy and wave measurements at geosynchronous

orbit both for individual cases as well as statistically across local and epoch times. Statistical EMIC occurrence rates from LANL and GOES both become elevated half a day before the onset of flux dropouts, peaking during the day following, and in the afternoon sector, consistent with theory and past observations. On January 10th, 2000, as LANL-89 trailed GOES 10 by two hours, EMIC wave signatures were detected in the plasma measurements at roughly the same local times as those measured by GOES magnetometers. Each wave burst measured by GOES 10 is subsequently detected in the plasma conditions at LANL-89 as it passes through the same region somewhat later in universal time. Strong agreement is found between the wave and proxy occurrences both statistically as well as for single events.

The ability to include LANL MPA data to complement wave measurements greatly enhances our understanding of EMIC wave distributions across local and storm times. As the LANL database consists of seven spacecraft spanning approximately 18+ years, it contributes a vast number of measurements to supplement current EMIC wave statistics at geosynchronous orbit. This proxy validation also enables the use of LANL satellites to provide multipoint measurements of equatorial wave distributions, to compare both with other nearby satellites as well as to ground based wave measurements (e.g. *Posch et al.*, 2010) or low altitude precipitation signatures (e.g., *Miyoshi et al.*, 2008; *Millan et al.*, 2010). As seen from the EMIC activity on January 10th, 2000 in Figure 3.4, as well as from the *Spasojevic et al.* [2011] study and Figure 3.9, this proxy can be used in combination with wave measurements and other proxies to study the temporal and spatial variation for individual EMIC events. With the extension of the proxy to calculate EMIC wave amplitudes, an estimation of wave-particle scattering rates can be made, to aid in the quantification of relativistic electron losses from the outer radiation belt [*Bortnik et*

al., 2011].   Here, we demonstrate the value of plasma measurements to aid in the characterization of global EMIC wave distributions.

Chapter 4: Inferred Storm-Time EMIC Wave Distributions

The following chapter is based on work that was published in Blum et al. (2009), Ion observations from geosynchronous orbit as a proxy for ion cyclotron wave growth during storm times, *J. Geophys. Res., 114,* A10214.

4.1 Introduction

Earth's radiation belts are highly variable, and the processes contributing to their enhancements and reductions are an area of active research. High relativistic electron flux levels are found following some geomagnetic storms but not others. The resultant flux does not seem to be correlated to the size of the storm or the pre-storm flux level [*Reeves et al.,* 2003]. Both acceleration and loss processes contribute to determining the post-storm populations, with wave-particle interactions believed to play an important role in these processes. *MacDonald et al.* [2008] examined whistler waves using a proxy based on the keV electron population and a superposed epoch analysis to find that storms resulting in higher radiation belt fluxes had higher levels of whistler waves. Their analysis agreed well with a similar superposed epoch analysis of whistler wave distributions using ground-based magnetometers [*Smith et al.*, 2004]. In this paper, we focus on electromagnetic ion cyclotron (EMIC) waves and look to see if there is any relation between their occurrences and storm-time radiation belt dynamics.

EMIC waves have long been observed in space and from the ground. In general, they have been found to be most prevalent in the dusk or afternoon sector [*Fraser et al.*, 2001]. Ground observations of Pc1-Pc2 waves have indicated consistent local-time distribution, however differences, possibly due to ionospheric attenuation, appear when comparing by storm-

phase; in particular, a distinct lack of these waves is observed during the storm main phase [*Engebretson et al.*, 2008]. This contrasts with most in situ observations, including early work by *Bossen et al.* [1976], which observed an increase in afternoon-sector Pc1 events at geosynchronous orbit, coinciding with the main phase of geomagnetic storms. Observational evidence for the scattering and loss of relativistic electrons by EMIC waves has been reviewed by *Millan and Thorne* [2007]. *Spasojevic et al.* [2004] used multiple IMAGE observations to show the first direct link between a detached subauroral proton arc and a plasmaspheric plume and that instability growth calculations were consistent with the Alfven-cyclotron instability causing EMIC waves and proton precipitation within the plume region.

In this study we do not use direct observations of EMIC waves. Rather, we infer the existence of the waves from the observed properties of the hot and cool plasma populations using statistical analysis and linear theory. Using the plasma-based proxy for EMIC waves described and validated in Chapter 3, we explore the inferred occurrence of such waves relative to relativistic electron flux levels during and after geomagnetic storms.

4.2 LANL Observations

In this study, we use LANL Magnetospheric Plasma Analyzer (MPA) particle data to calculate the proxy for enhanced EMIC wave activity, Σ_h, defined in Equation 3.4. We look at data from seven satellites at geosynchronous orbit from years 1989 through 2004. We calculate bulk moments, including density and perpendicular and parallel temperature for both the hot proton population, defined as 100eV-45keV, and the cool protons, less than 100eV. Perpendicular and parallel are in reference to the background magnetic field vector, as inferred from symmetry in the plasma distributions [*Thomsen et al.,* 1999]. The ion population is assumed to be only protons as the MPA instrument does not distinguish among the various ion

species. While magnetospheric conditions can be quite far from this ideal, the presence of heavy ions should not greatly affect our calculations. Cold He^+ can at times constitute a significant fraction of the cold magnetospheric ions, but it does not contribute substantially to driving the instability. Although helium cyclotron damping creates a stop band in the spectrum near the helium cyclotron frequency, the maximum growth rate is only modestly reduced [*Gendrin et al.*, 1984; *Kozyra et al.*, 1984]. Hot magnetospheric O^+ can also be present during magnetic storms. Such ions can be anisotropic and contribute to instability growth, but the resonant frequencies of such waves are near 1/16 the proton cyclotron frequency, Ω_p, and therefore resonate with electrons of energies a few times higher than the MeV ones of primary geophysical interest for this study [*Meredith et al.,* 2003].

From these data, we use a superposed epoch technique to examine over 300 storms, chosen following criteria first described by *O'Brien et al.* [2001, 2003] and subsequently used by *Smith et al.* [2004] and *MacDonald et al.* [2008]. Storms were superposed by setting the time of minimum Dst equal to zero epoch. The storms were chosen to be isolated, not within 4 days of another storm's minimum Dst, and to have a minimum Dst of less than -50 nT. The storm list is divided into two categories, termed "events" and "nonevents", based on post-storm relativistic electron flux levels measured by LANL satellites at geosynchronous orbit (see Figure 4.1). Storms whose noon-reconstructed 1.8-3.5 MeV electron flux was above 0.5 e-/cm^{2}s sr keV for 48-72 hrs after Dst minimum were categorized as events, and those with fluxes lower than 0.5 as nonevents. (The so-called noon-reconstruction technique is described by *O'Brien et al.,* 2001). These criteria, based only on the post-storm flux, were chosen because the pre-storm flux has been shown to be uncorrelated with the post-storm result [*Reeves et al.,* 2003].
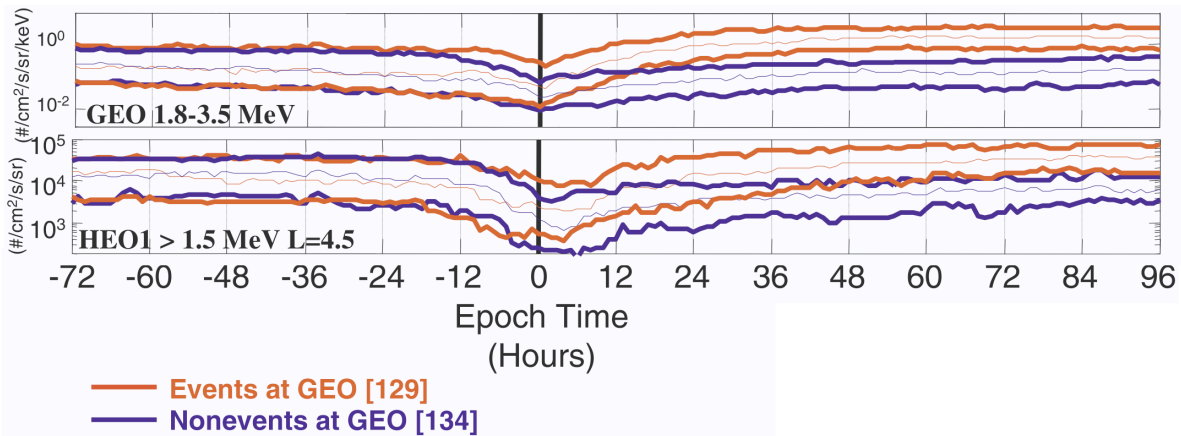
Figure 4.1 Superposed epoch of the noon reconstructed MeV electron fluxes during the storms investigated in this work. The storms, superposed based on minimum Dst, are grouped into two categories. Storms resulting in noon-reconstructed 1.8-3.5 MeV electron fluxes > 0.5 e/cm² s sr keV (orange) are labeled "events", and those resulting in fluxes lower than this (purple) "nonevents." Thin orange (purple) traces indicate the median at each epoch time for events (nonevents). Thick traces indicate the upper and lower quartiles. (Adapted from *O'Brien et al.*, 2003)

Figure 4.2 shows superposed Dst and Kp plots for both the 138 storms constituting the events list, having higher post-storm flux levels, and the 183 storms of the nonevents, having lower levels. The Dst profiles for the two groups of storms look fairly similar, while the Kp for events storms stays elevated, above a level of 3, for approximately one day longer than nonevents. This suggests that the events storms have extended driving, similar to corotating interaction region (CIR) occurrences examined using superposed epoch analysis by *Miyoshi and Kataoka* [2005] and *Denton et al.* [2006].

With this data set, we compare relevant properties of the geosynchronous plasma populations for the events and nonevents storm lists. We examine the effect of these parameters on the EMIC wave proxy, described and validated in Chapter 3, for the two sets of storms, globally and as a function of storm phase, or epoch time.

a)   EVENTS
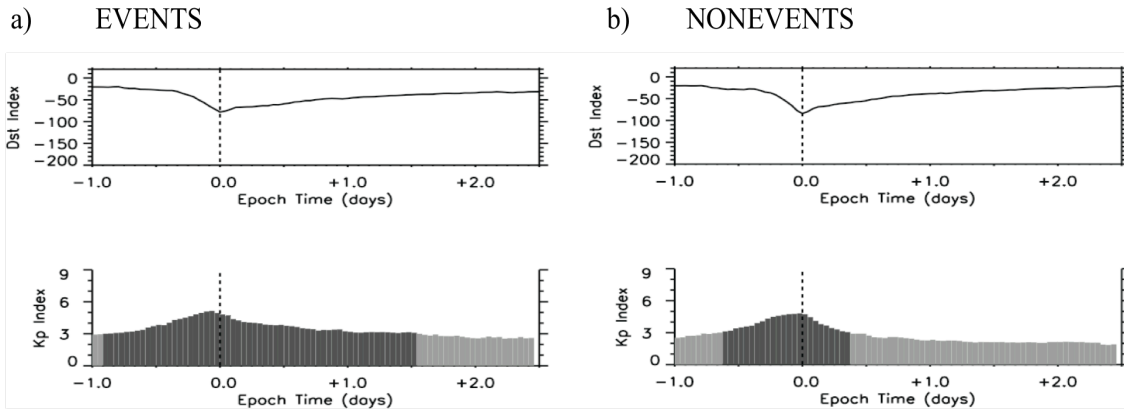
b)   NONEVENTS

Figure 4.2 Superposed storm Dst and Kp indices for "events" and "nonevents" storm-sets. Dst profiles look similar, while an elevated Kp (above 3) lasts about a full day longer for the events storms. (Adapted from *MacDonald et al.,* 2008)

4.3 Superposed Epoch Results

First we perform an observational test of the linear theory proxy formulation discussed previously, and we compare the theoretical instability threshold S_h, from Equation 3.3a, to our observational EMIC growth parameter Σ_h. The solid lines in Figure 4.3 show S_h as a function of the ratio of the hot proton density to the total density n_h/n_e for three different growth rates, $\gamma/\Omega_p =$ 0.001, 0.004, and 0.01, where γ is the maximum temporal growth rate. The scatter points show Σ_h for the nonevents storm set for two different local times, at noon and at midnight. Both events and nonevents storm sets show similar qualitative behavior when plotted in this manner. Here, data points with increasing Σ_h values relative to an S_h curve correspond to the transition from stable conditions to successively stronger growth rates. Σ_h approaches a theoretical limit (e.g. $\gamma/\Omega_p = 0.01$ for the noon points) indicating that enhanced fluctuations from the EMIC instability are effectively scattering protons near this threshold condition and are imposing a statistical constraint on the proton temperature anisotropy. Figure 4.3 further validates the use of the observed Σ_h compared to the theoretical limit of S_h as a proxy for enhanced EMIC waves.

Additionally, it tells us that a growth rate of 0.001 is appropriate for data points at midnight, while a higher value of 0.01 is approached during local times around noon.
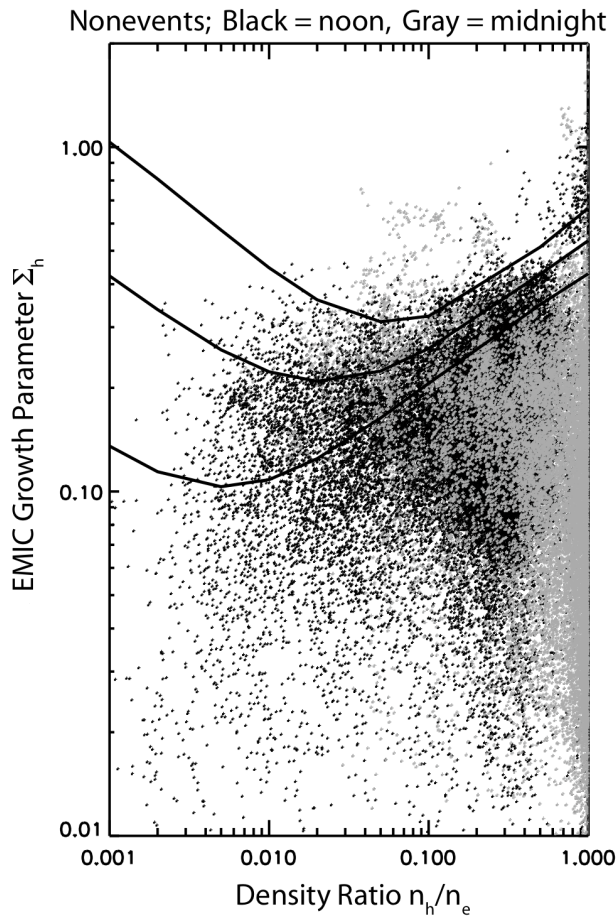
Figure 4.3 Scatterplot of EMIC growth parameter Σ_h versus the density ratio n_h/n_e (hot proton density divided by total proton density) for noon (black points) and midnight (gray points) for the nonevents storm set. The instability threshold S_h is also plotted here as three solid black lines, corresponding to three different growth rates γ/Ω_p (the lowest line for a growth rate of 0.001, then 0.004, and highest is 0.01). We see the Σ_h values approach S_h of different growth rates at different local times; $\gamma/\Omega_p = 0.001$ is appropriate for data points at midnight, while 0.01 is approached around noon.

We plot various parameters over local and epoch times to better understand the variations of constituent plasma properties for our events and nonevents storm sets. First we look at the different density components of the proton population – the hot and cool, as well as the ratio of the hot to total proton density n_h/n_e (Figure 4.4a, c, e for events, and Figure 4.4b, d, f for

nonevents). Figure 4.4a and b show the hot plasma sheet density, highest around minimum Dst from dusk through dawn, extending further both in local and epoch time for the nonevents storms, as was seen by *Denton et al.,* [2006]. In Figure 4.4c and d, there is evidence of cold dense plasmaspheric plumes in the afternoon sector during storm main phase (prior to minimum Dst) and continuing, with a weaker presence and narrower in local time, through the recovery phase in both sets of storms. The density ratio (Figure 4.4e and f) is a variable that affects the value of the instability threshold S_h for a given growth rate (see Figure 4.3). Over most of the range of n_h/n_e, a lower ratio (corresponding to more cool plasma) lowers the instability threshold, and enhanced EMIC waves can more easily be obtained. Both Figure 4.4e and f show that the plasma sampled at geosynchronous orbit is dominated by hot plasma in the midnight sector throughout the duration of the storms, and that very low levels of hot protons exist on the day side. Starting just prior to one day after minimum Dst, the density ratio is lower for the nonevents than events in the region around midnight.

We also explore the temperature anisotropy of the hot protons, $T_{\perp h}/T_{\parallel h}$, for both storm lists (Figure 4.5a and b), as it is the temperature anisotropy in this population that drives the Alfven-cyclotron instability responsible for the growth of EMIC mode waves. Here a difference between the events and nonevents is most striking during the recovery phase. The night-side anisotropy increases after zero epoch in the nonevents, while in the events it remains at levels around 1.0 on most of the night side.

Figure 4.5c and d show the hot proton parallel beta $\beta_{\parallel h}$, equal to $8\pi n_h T_{\parallel h}/B_o^2$, for events and nonevents. Beta is composed of the hot proton density as well as the hot parallel temperature. The combination of these parameters makes for slightly higher beta levels in the
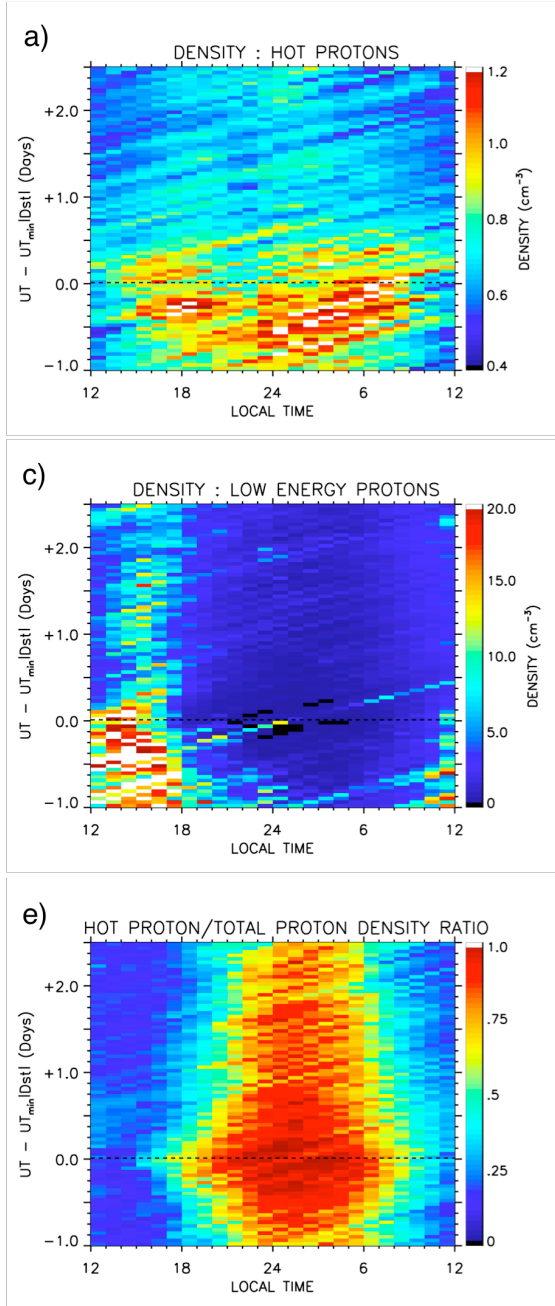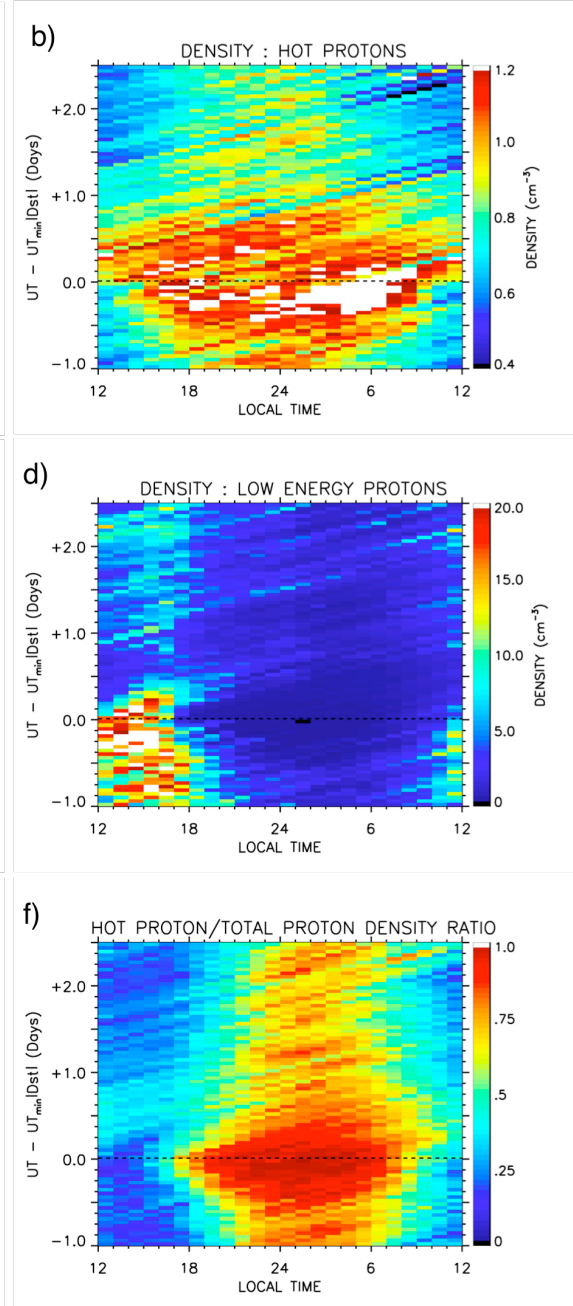
Figure 4.4 (a and b) Hot proton density n_h, (c and d) cold proton density n_c, and (e and f) density ratio n_h/n_e across local and epoch times for events and nonevents. Density ratio n_h/n_e is lowest in the region from approximately noon to dusk, where the cold dense plume is located.

nonevents, but the similar profiles suggest that this parameter does not cause significant differences between events and nonevents in the observational EMIC growth parameter Σ_h.
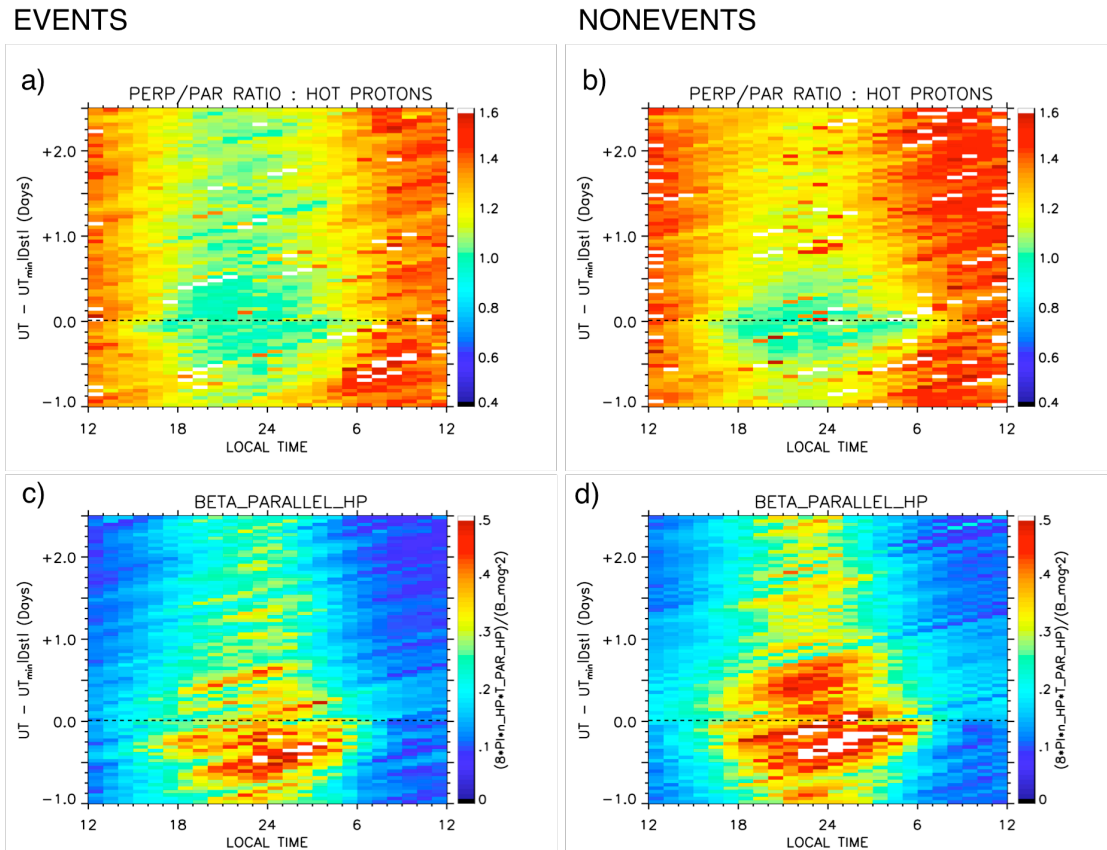
Figure 4.5 (a and b) Temperature anisotropy and (c and d) plasma beta $\beta_{\|h}$ for hot proton populations. These two parameters are the main components in the calculation of the observational EMIC growth parameter Σ_h.

In Figure 4.6, we plot the theoretical instability threshold S_h, as well as the observational EMIC growth parameter Σ_h, for events and nonevents. Here we use a growth rate of 0.001, as suggested by Figure 4.3, to calculate S_h. Figure 4.6a and b show that S_h has the same variation pattern as n_h/n_e (from Figure 4.4e and f) since the density ratio is the only plasma parameter upon which S_h depends. Figure 4.6a and b show variation of the instability threshold S_h over local and epoch times, but the difference between storm sets does not appear to be great.

EVENTS   NONEVENTS
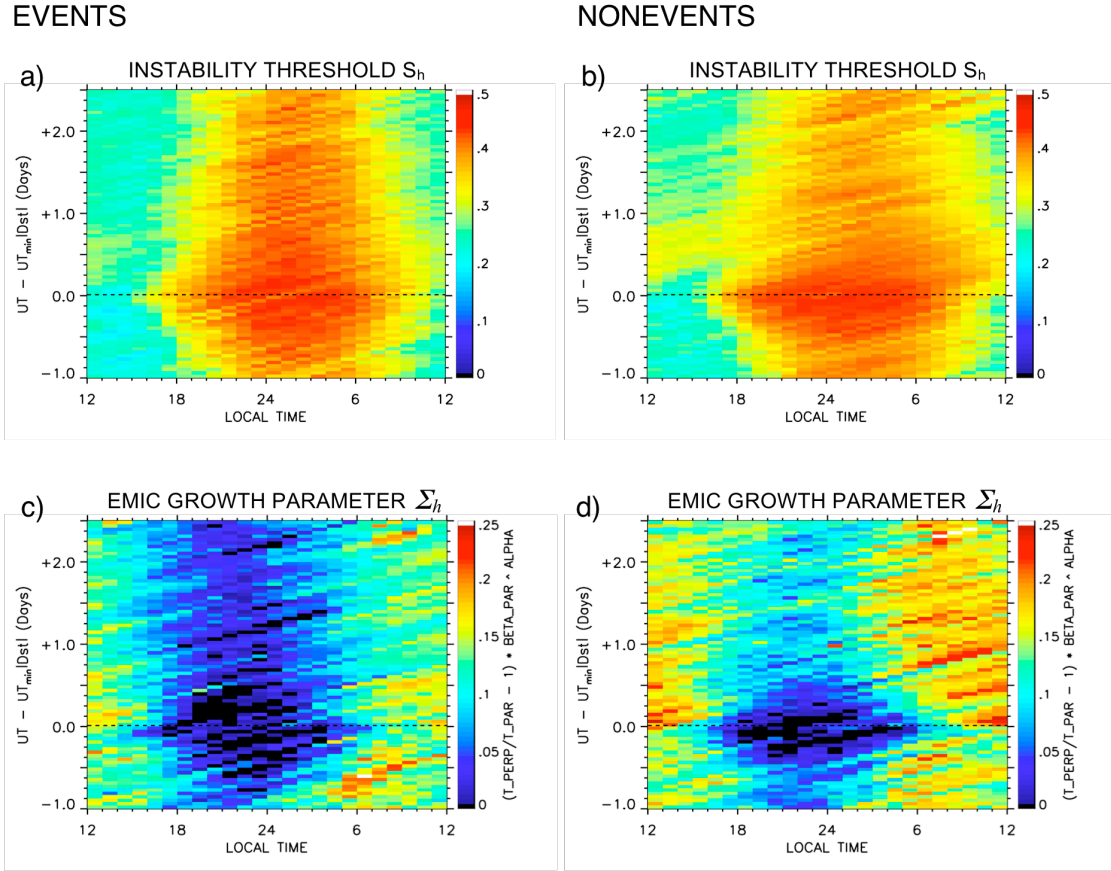
Figure 4.6 (a and b) Theoretical instability threshold S_h, dependent on the density ratio n_h/n_e only, and (c and d) EMIC growth parameter Σ_h, based on measured plasma parameters. Both are plotted for all local and epoch times for a growth rate $\gamma/\Omega_p = 0.001$.

The observational EMIC growth parameter Σ_h (Figure 4.6c and d), however, shows a significant difference between the events and nonevents storm sets, as well as a great deal of variation over local time.   Nonevents have a higher value, especially around noon, but additionally around dawn in the recovery phase. The absolute value of this parameter alone, though, is not necessarily indicative of higher wave growth, but must be compared with the expected S_h at given local and epoch times to be able to infer relative wave growth.

To make this comparison, we calculate the percent of Σ_h data points that exceed the average S_h for each local and epoch time bin. Figure 4.7 shows the percentage of time that the

observational EMIC growth parameter Σ_h exceeds the average instability threshold for a growth rate of 0.001. Here we see that the percentage is high for both events and nonevents in the day leading up to minimum Dst, but it remains elevated longer during the period of 1 to 4 days after minimum Dst for the nonevents.
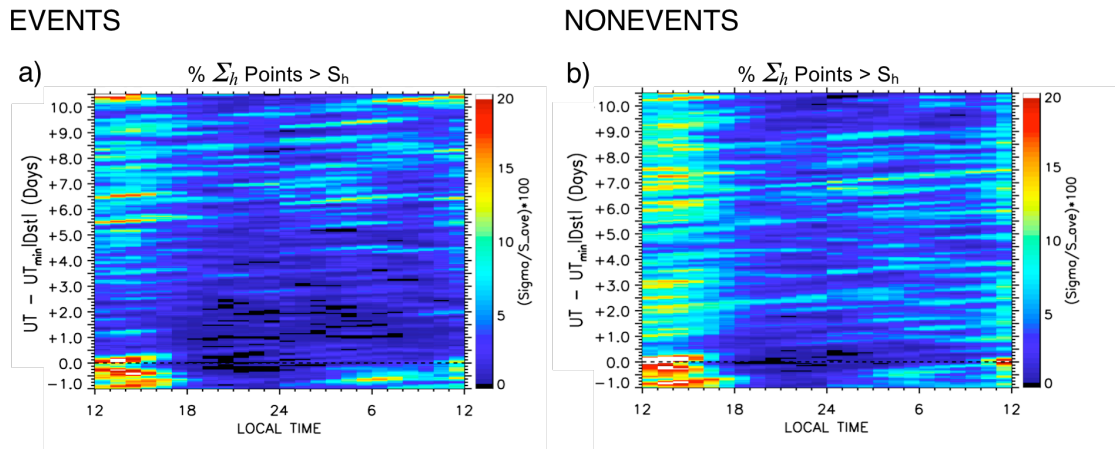
EVENTS   NONEVENTS

Figure 4.7 The percentage of Σ_h values which lie above the average S_h value for a given local and epoch time. For both (a) events and (b) nonevents, this percentage is high from noon to dusk during the main phase of the storms. In the recovery phase, however, there is a significant difference between the two storm sets, and the values for the nonevents remain higher than events for a few days after minimum Dst.

4.4 Discussion

Figure 4.8 shows the epoch-time dependence of this percentage averaged from noon to dusk, the region of most interest. Here gray indicates nonevents, black indicates events, and the thin solid line shows the quiet time average of both storm sets (from 6-10 days after storm epoch), with dotted lines showing the standard deviation averaged for both storm sets. The events storms, which result in elevated relativistic flux levels 48 to 72 hours after minimum Dst, show different Σ_h behavior than the nonevents especially 1 to 4 days after zero epoch, during the recovery phase of the storms. Both types of storms appear to have higher occurrence of

enhanced EMIC waves, according to our proxy, in the main phase of the storm, which is consistent with in situ wave measurements seen in *Fraser et al.* [2010]. They then both display a sharp drop in this measurement immediately after zero epoch, minimum Dst. In the subsequent
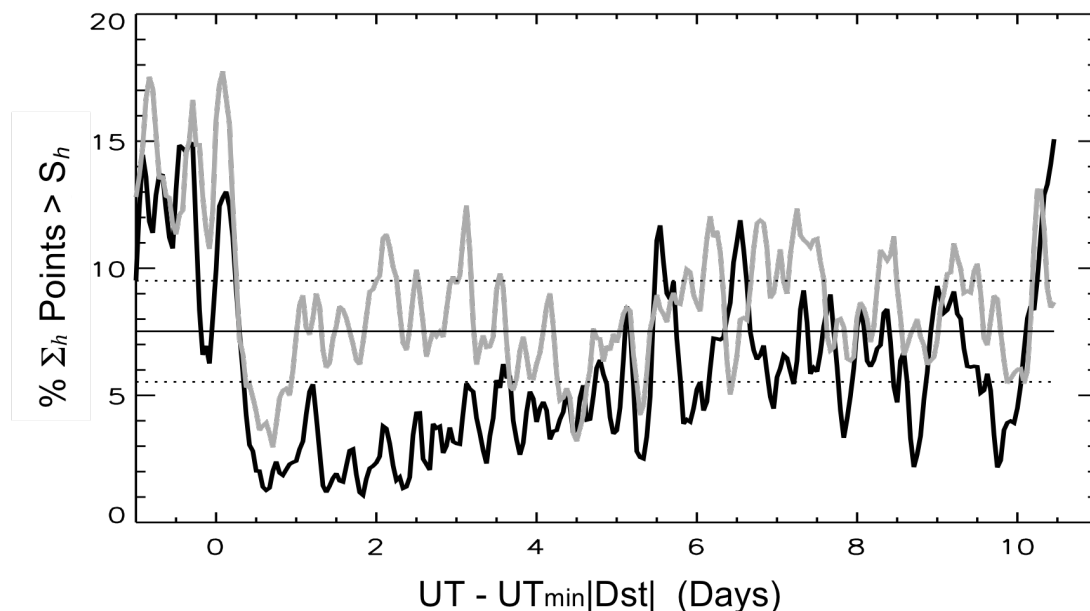
Figure 4.8 An average of the parameters plotted in Figure 4.7 taken from noon to dusk, the period of most activity. The black line represents the events storms, and the gray represents the nonevents. Here the difference in the percentage between the storm sets in the recovery phase is even more distinct. The quiet time average is displayed with the thin solid line, along with the standard deviation (dotted lines).

days, however, the nonevents recover to levels around 8% (an average quiet time value), while the events remain at around 3%. The quiet time value for both storm sets fluctuates, with an average value around 7.5%. This suggests that the difference in events and nonevents in the recovery phase of storms is associated with a suppression of EMIC growth in the events, rather than an enhancement in the nonevents. One possible explanation for this is that CIR storms, which show similar properties to our events storms, involve enhanced convection and elevated Kp. *Denton et al.* [2005] show that temperature anisotropy is typically inversely related to Kp index. As temperature anisotropy is a main component of our calculation of the EMIC growth

parameter, a lower anisotropy could lead to suppressed Σ_h values. As Kp remains elevated during the recovery period of our events storms, as seen in Figure 4.2, less anisotropic plasma is present during this period, leading to the suppression of EMIC growth seen in our events storms.

We return to Figure 4.7 to examine the percentage values over all local and epoch times. The most concentrated area of enhanced EMIC fluctuations is shown to be in the region from noon to dusk. This is in agreement with in situ EMIC wave observations, as shown by both *Meredith et al.* [2003] and *Bossen et al.* [1976]. The distribution of elevated values in these final percentage plots (Figure 4.7) differs significantly from those for the observational EMIC growth parameter Σ_h alone in Figure 4.6c and d. This emphasizes the need to compare the observed Σ_h to the theoretical instability threshold determined by S_h. While the temperature anisotropy and hot plasma beta parameters cause elevated values from dawn nearly to dusk in our nonevents, the density ratio causes the instability threshold to be more easily attained only from noon to dusk, where more cold plasma is present. Therefore we conclude that the Alfven-cyclotron instability can grow, and enhanced EMIC waves can arise, most easily from noon to dusk, showing that our proxy for such waves corresponds well in local time to wave observations.

4.4.1 Additional Superposed Epoch Proxy Studies

As shown in the discussion above, the long-duration multipoint LANL-GEO database combined with plasma-based proxies for waves can give insight into the global wave distributions under a variety of geomagnetic conditions and local times. While the study detailed here categorized storms by the resulting radiation belt electron response, we can also group and examine storms according to their driver. We have applied this superposed epoch and proxy technique to study a set of 124 high speed stream (HSS) driven storms, first selected by *Denton and Borovsky* [2008]. Zero epoch time was chosen as the time of magnetospheric convection

onset, following the arrival of each HSS at the magnetosphere (via examination of the Kp index). The exact time of the zero epoch was derived at higher time resolution than the 3h Kp index by identifying the time of equatorward expansion of the midnight boundary index (MBI; *Madden and Gussenhoven* 1990). As shown by *Thomsen* [2004], the Kp index and the MBI are highly correlated with the magnetospheric convection onset. It is also noted that previous studies have identified that the MBI provides a cleaner comparison basis for these small HSS-driven storms than the Dst index. The mean minimum Dst for HSS storms is only approximately -20 nT [*Denton and Borovsky* 2008]. Dst is not used in the selection criteria for the HSS storms. This storm set will be further discussed and investigated in Chapter 5.

In *MacDonald et al.* [2010], we compare two plasma-based proxies derived from LANL/MPA data – the EMIC proxy defined and discussed previously as well as a similar proxy for whistler mode chorus waves, based on anisotropic keV electron distributions [*MacDonald et al.*, 2008] – to examine the relative contributions of different wave types across various storm types and phases. The inferred distributions of EMIC and whistler mode waves are examined during the 124 HSS storms and compared to their distributions during the previously analyzed events and nonevents storm sets. Figure 4.9 shows the EMIC and whistler wave proxies during these sets of storms.

We see in Figure 4.9 that the relativistic electron fluxes during HSS events start from a base level higher than that of the other groups. They also peak higher and slightly later (approximately 1.5 days) than the set of events storms. In addition, the dropout for HSS storms is similar in magnitude to nonevent storms, i.e. quite large, although the flux levels for HSS storms begin much higher. Relative to the other two categories, the HSS events have the highest inferred EMIC-wave activity in the main phase of storms, with a full 20 percent of observations
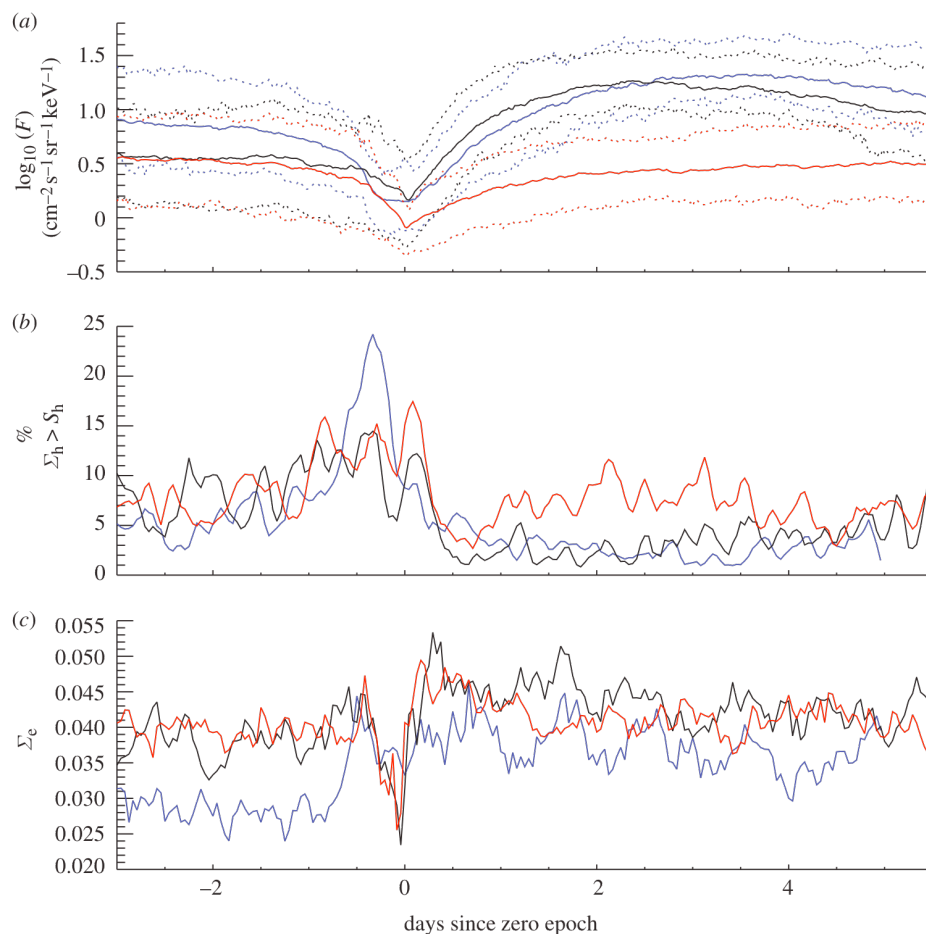
Figure 4.9 Comparison between relativistic electron flux, EMIC wave growth and whistler wave growth from the superposed epoch results of the three storm types: blue, high speed stream (HSS) driven storms; black, events; red, nonevents. Zero epoch is time of convetion onset +0.5 days for the HSS events, and time of minimum Dst for the events and nonevents. (a) SOPA electron flux from 1 to 1.5 MeV (dashed lines represent quartiles), (b) proxy for EMIC waves, averaged over the peak local times from 12.00 to 18.00, and (c) whistler wave proxy averaged over the peak local times from 24.00 to 12.00. (From *MacDonald et al.*, 2010)

exceeding a growth rate of 0.001, consistent with the largest observed dropout. In the recovery phase, the level of EMIC wave activity during HSSs looks similar to that of the events storms, namely that it is suppressed below 'normal' levels. This is consistent with a suppressed loss mechanism and hence a net gain of relativistic electrons. For whistler waves during the HSS events, there is a prolonged, but not dramatic, enhancement throughout the main and recovery phases, during the times of fast solar wind and enhanced magnetospheric convection. In the pre-

storm period for HSS events, whistler waves are significantly reduced below 'normal' levels seen in either event or nonevent storms.

Recent efforts (e.g. *Huang et al.*, 2009) have shown that magnetopause shadowing may be responsible for the observed major dropout of relativistic electron fluxes at the main phase. The results outlined in this study indicate that conditions are ripe for intense EMIC waves around storm onset as well. The relative importance of adiabatic and non-adiabatic effects on losses during the main phase of storms thus remains open and a subject of future research.

Radiation belt electron fluxes are lowest for the storms exhibiting the most EMIC activity and the least whistler wave activity in the recovery phase. This is consistent with the current interpretation that whistler waves are primarily an acceleration mechanism, whereas EMIC waves are primarily a loss process for relativistic radiation belt electrons. The inclusion of HSS events in this comparison leads to the interesting possibility that the relative suppression of EMIC activity in the recovery phase may be more important for radiation belt regrowth than the enhanced whistler activity.

4.5 Summary

Using the large LANL/MPA database and the plasma-based proxy for EMIC waves developed in Chapter 3, we are able to investigate the statistical distributions of EMIC waves across various storm types and phases to better understand the role these waves might play in storm-time radiation belt dynamics. We observe that there are differences in the statistical behavior of certain relevant plasma properties between storms resulting in higher versus lower net fluxes of relativistic electrons. From these plasma parameters and validated linear theory, we find that both the average values of our observational EMIC growth parameter Σ_h, as well as the frequency of elevated values, are greater, especially in the recovery phase of the storm, for

storms resulting in lower radiation belt fluxes, labeled nonevents. This is consistent with the idea that enhanced EMIC waves scatter relativistic electrons and thereby contribute to the loss of such particles from the magnetosphere in the main phase, and for nonevents on into the recovery phase, preventing the buildup of substantial post-storm flux enhancements. Additionally, as shown by *MacDonald et al.* [2010], suppression of EMIC waves as a loss mechanism may be as important for some post-storm radiation belt buildups as concurrent acceleration mechanisms. This EMIC proxy combined with a similar proxy for whistler chorus waves can be used to study the relative contributions of various wave types to overall radiation belt dynamics through a balance of acceleration and loss mechanisms.

Chapter 5: SAMPEX Rapid Precipitation Measurements

5.1 Introduction

We move now from studying storm-time EMIC wave distributions to investigating precipitating relativistic electrons themselves. Understanding the characteristics and sources of precipitation is essential to forming a complete picture of global precipitation loss rates. Relativistic electron precipitation, as observed from low Earth orbit (LEO), can be divided into a few categories: slower, steadier diffusive pitch angle scattering into the edge of the loss cone, and more rapid scattering events, filling the loss cone on timescales of milliseconds to seconds. The slow decay of the outer radiation belt observed during quiet times has been attributed to this steadier pitch angle diffusion by plasmaspheric hiss waves, resulting in electron lifetimes on the order of 5-20 days [*Meredith et al.*, 2006]. However, changes in the trapped outer belt electron population can occur on much faster timescales as well, especially in response to geomagnetic activity. Rapid depletions of outer belt electrons on ~hour timescales following geomagnetic storms are often not fully explained by losses to the magnetopause and outward diffusion (e.g. *Hudson et al.*, 2014; *Turner et al.,* 2014), suggesting rapid atmospheric loss must be occurring as well.

Here we focus on two specific types of rapid precipitation and we investigate their relative contributions to radiation belt losses. Sudden enhancements in electron fluxes are often observed at LEO on timescales of short bursts lasting less than a second (termed microbursts) to longer duration areas of precipitation spanning a few degrees in latitude (precipitation bands). Each of these precipitation signatures can be an integral contributor to relativistic electron

precipitation loss – microbursts have been calculated to be able to empty the outer radiation belt in less than a day [*O'Brien et al*, 2004; *Thorne et al*., 2005] – and both microbursts and precipitation bands are still not well understood.

We examine microbursts and precipitation bands using low-altitude measurements from Solar, Anomalous, and Magnetospheric Particle Explorer (SAMPEX) to better characterize and quantify the contribution of these rapid precipitation events to radiation belt electron loss. By focusing on specific types of precipitation, and investigating the distributions of these rapid precipitation events, we gain insight into both potential scattering mechanisms as well as the relative roles of various loss processes with respect to overall radiation belt dynamics. Low-altitude measurements, such as those from SAMPEX, are necessary to make direct measurements of the precipitation loss, as most low-inclination, high-altitude spacecraft cannot resolve the electron pitch angle distribution near and inside the loss cone. The spatial distributions of these rapid precipitation features are examined, as well as their occurrences and magnitudes during various storm types and phases. The aim of these investigations is to better understand the relative role of these two loss processes in overall radiation belt dynamics, and how it varies spatially as well as with storm type and phase.

5.2 SAMPEX/HILT Observations

To interpret the SAMPEX measurements, one must first understand some details of the mission and instrument as well as the nature of low altitude measurements in general. SAMPEX was launched in July 1992 into a 520-670 km, 82° inclination orbit [*Baker et al.,* 1993]. Initially expected to reenter by 2000, a quiet sun and extended solar minimum allowed it to remain in operation until November 2012 when it finally reentered. The HILT (Heavy Ion Large Telescope) instrument onboard returned high time resolution measurements of >150 keV and >1

MeV electrons. We focus here on the >1 MeV measurements from the instrument solid state

detectors (SSDs), as we are primarily interested in these higher energy radiation belt electrons.

HILT contains of an array of 16 SSDs, arranged in 4 rows of 4, each row with its own signal

processing chain and labeled SSD1-4 (see Figure 5.1 for an instrument schematic).   The

instrument was operated in four different modes over the course of the mission, returning

anywhere between 20-100ms count rates in one to four of these rows.
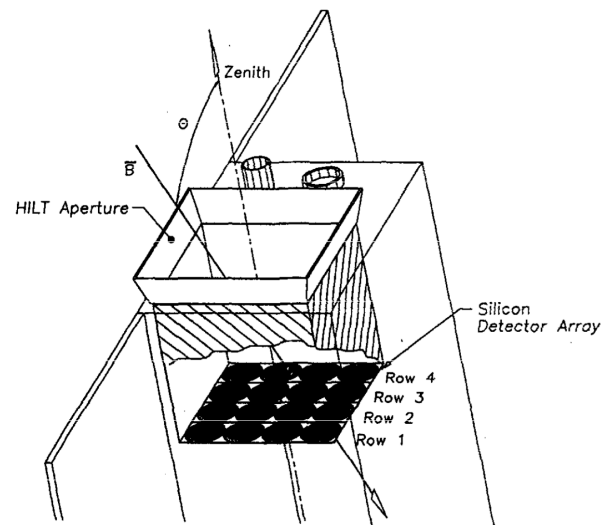
Figure 5.1 Cross-secton of the HILT instrument as mounted on the SAMPEX satellite. The square array of 16 SSDs is shown with the four rows explicitly shown. (From *Blake et al.,* 1996)

The equatorial loss cone in the outer radiation belt is < ~6°, making it difficult to resolve

precipitating fluxes from low inclination orbits. At low altitudes, however, this loss cone opens

up to ~60° or more, allowing SAMPEX to directly measure electrons within and just outside the

loss cone. Due to the offset asymmetric nature of Earth's internal magnetic field, the size of this

loss cone varies with both longitude and hemisphere. Particles can thus be categorized as one of

three types: ones that will be lost to the atmosphere within one bounce period (untrapped, or

bounce loss cone BLC), ones that are lost within one drift period (quasi-trapped, or drift loss

cone DLC), and those that remain trapped in the magnetosphere for timescales larger than their drift period. These three types are visualized in the cartoon in Figure 5.2, left panel (adapted from *Tu et al.*, 2010). With its wide, 68° field of view, SAMPEX/HILT measures a combination of these three particle populations at different points along its orbit, as demonstrated in Figure 5.2, right panel (adapted from *Dietrich et al.,* 2010). Measurements around the South Atlantic Anomaly (SAA), a region of lower magnetic field strength above the coast of Argentina (~60°-0°W), are dominated by trapped particles, while electrons measured at conjugate locations in the Northern hemisphere will precipitate within one bounce.
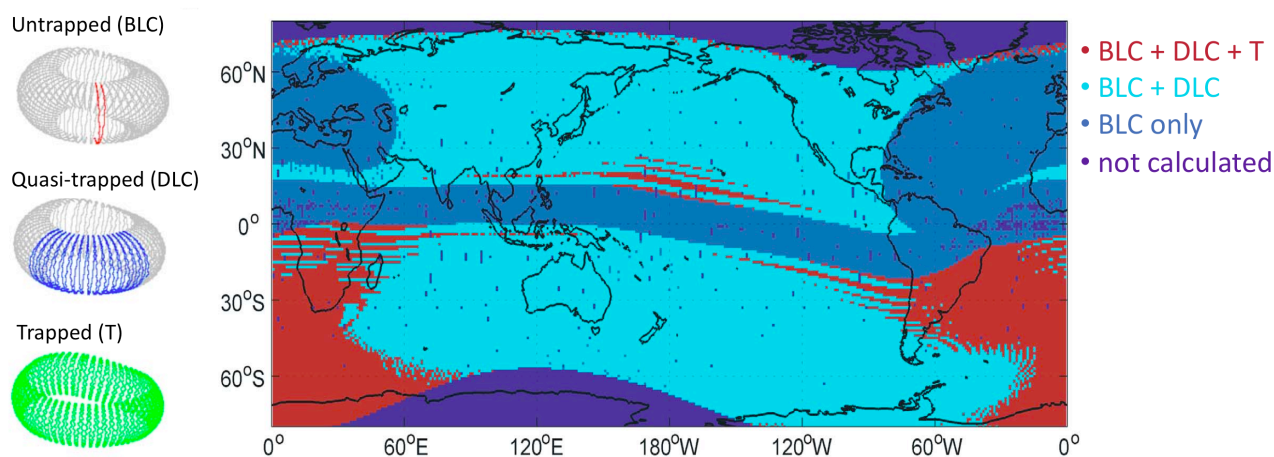
Figure 5.2 (left) Cartoons illustrating the three types of particle populations observed by SAMPEX: trapped (green), quasi-trapped (blue), and untrapped (red). (right) World map showing the changing radiation belt populations observed by SAMPEX/HILT, with T indicating trapped flux, DLC quasi-trapped (or drift loss cone) and BLC untrapped (or bounce loss cone). For most locations where there are significant radiation belt electrons, it observed a combination of DLC and BLC populations. (Adapted from *Tu et al.,* 2010 (left) and *Dietrich et al.,* 2010 (right))

To help distinguish among these three particle populations in the HILT data, qualitative pitch angle information can be extracted by comparing the count rates in SSD1 versus SSD4. Due to the rows' slightly different look directions, a difference in these two count rates suggests a more anisotropic distribution and measurements dominated by trapped and quasi-trapped electrons, while an isotropic distribution would result in all four SSD count rates converging to

the same value [*Blake et al.,* 1996]. While the HILT measurements tend to be dominated by trapped and quasi-trapped particles as SAMPEX passes through the outer belt, on certain occasions rapid pitch angle scattering occurs, filling the bounce loss cone and causing direct precipitation. In the data, these events appear as rapid flux increases and isotropization of the flux, superimposed atop the smoothly varying background anisotropic trapped and drift loss cone fluxes (as depicted in Figure 5.3). The following sections describe two distinct types of rapid precipitation events seen in the SAMPEX/HILT data – microbursts and precipitation bands.
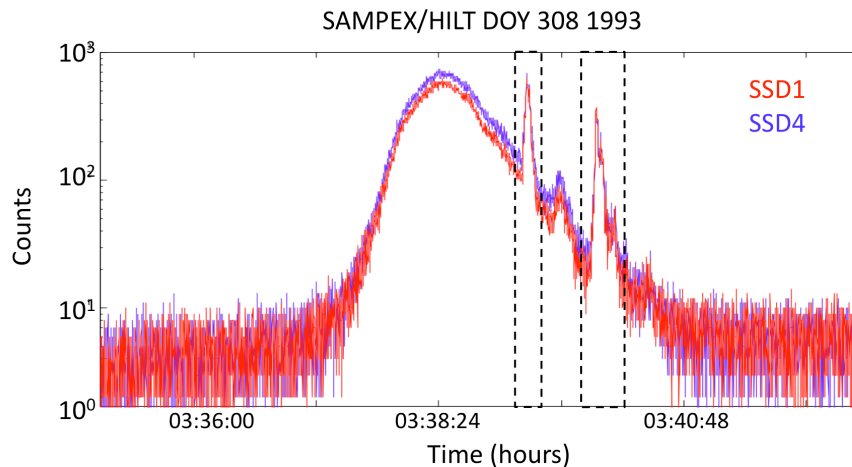
Figure 5.3 SAMPEX/HILT data from the SSD1 (red) and SSD4 (blue) detector rows during a pass through the outer radiation belt. Qualitative pitch angle information can be obtained by comparing the count rates in these two detector rows. More anisotropic, 90° peaked populations are observed throughout most of the outer radiation belt, while the count rates converge during rapid flux enhancement events shown in the dashed boxes.

5.2.1 Microbursts

Rapid bursts of electron precipitation lasting < 1 second were first observed by balloon borne detectors in 1964 [*Anderson and Milton*, 1964]. These observations were of 10s -100s of keV electrons and similar bursts were subsequently seen by low altitude satellites as well. The first similar duration (~100 ms) relativistic electron (>1MeV) precipitation bursts were detected

by the low altitude, sun-synchronous S81-1 satellite [*Imhof et al.*, 1992]. These relativistic microbursts have been seen by a number of LEO satellites since then, including SAMPEX, and are the precipitation features of interest here. They occur most frequently on the dawn side, more often during periods of enhanced geomagnetic activity [*Nakamura et al.*, 2000; *Lorentzen et al.*, 2001a]. They are consistently measured to have a sharp rise time with slower decay, suggesting that these precipitation bursts are temporal in nature, typically lasting a few 100s of milliseconds [*Millan and Thorne*, 2007]. They are often measured in groups or clumps though (see Figure 5.4), and the spatial and temporal extents of these regions of microburst activity are still very uncertain. Figure 5.4 illustrates microburst precipitation detected by the SSD1 detector on the SAMPEX/HILT instrument during a pass through the outer radiation belt. During this six minute pass, microburst activity extends from L=4.5-6.5, while each individual burst lasts less than one second.
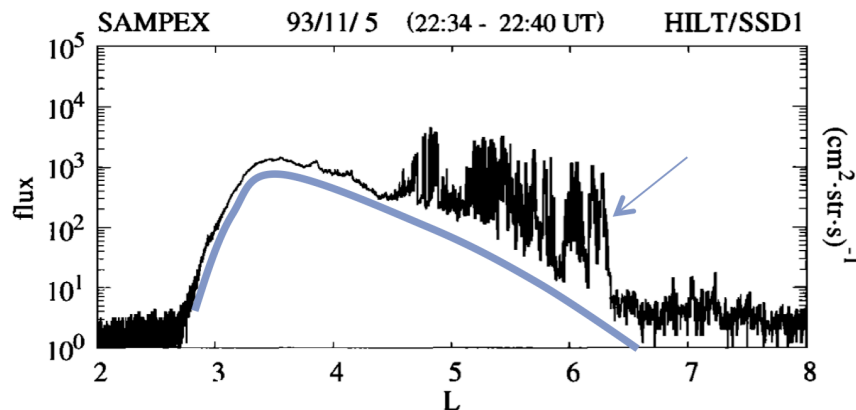
Figure 5.4 SAMPEX/HILT pass through the outer radiation belt on November 5, 1993. Microbursts up to multiple orders of magnitude above the background flux (shown by the blue curve) are evident. Microburst activity extends from ~L=4.5-6.5 (marked by the blue arrow), while each individual burst lasts less than one second. (Adapted from *Nakamura et al.*, 2000)

Whistler mode chorus waves are a primary mechanism believed to produce microburst precipitation. Similar distributions in local time and L-shell between the waves and precipitation

suggest that the two phenomena may be related [*Lorentzen et al.*, 2001a; *Johnston and Anderson,* 2010].   Theoretical calculations show that chorus waves near the equator are gyroresonant with the keV electrons by which they are generated but that they can resonate with MeV electrons at higher latitudes or harmonic numbers [*Thorne et al.*, 2005]. Additionally, large amplitude whistler waves propagating obliquely to the background magnetic field, first reported by *Cattell et al.* [2008], have also been suggested as a scattering mechanism through nonlinear wave-particle interactions. While a number of studies have attempted to correlate observations of whistler mode waves and microbursts (e.g. *Imhof et al.,* 1992; *Lorentzen et al.,* 2001a; *Kersten et al.*, 2011), one-to-one correspondences are difficult to make observationally.

Thorne et al. [2005] calculate radiation belt electron lifetimes due to microbursts to be on the order of one day during the main phase of geomagnetic storms, suggesting that these events can contribute significantly to storm-time losses. However, microbursts are often also detected during the recovery phases of storms that result in net enhancements of the outer radiation belt [*O'Brien et al.*, 2003]. *O'Brien et al.* [2004] try to reconcile this inconsistency by examining three storms, where they conclude that microbursts during the main phase contribute significant losses to the outer radiation belt, while those during the recovery phase were of smaller magnitude, and thus concurrent acceleration mechanisms dominate. Whistler mode chorus waves are known to be a strong local acceleration mechanism in the outer radiation belt as well as a potential source of microbursts [*Bortnik and Thorne*, 2007]. For this reason, microbursts have been used both as a measure of radiation belt electron loss, and additionally as a proxy for chorus waves and acceleration of electrons [*O'Brien et al.*, 2003]. The balance of the losses and acceleration, both possibly caused by chorus waves, determine the net effect on outer radiation belt electron fluxes.

5.2.2 Precipitation Bands

A second distinct type of rapid precipitation seen in SAMPEX data are broader, typically a few degrees in latitude, and are referred to here as "precipitation bands" following *Blake et al.* [1996]. These bands are often seen in conjugate locations and on consecutive orbits [*Blake et al.*, 1996], suggesting their 10s of seconds duration, as measured by LEO satellites, is due to spatial rather than temporal characteristics. Figure 5.5 depicts an example precipitation band measured by SAMPEX/HILT at the edge of the outer radiation belt. Other low-altitude spacecraft have detected similar features at a range of energies, from 10's of keV electrons up to MeV (e.g. *Paulikas et al.,* 1966). These measurements often, but not always, show some qualitative coherence in band structure among various energy channels.
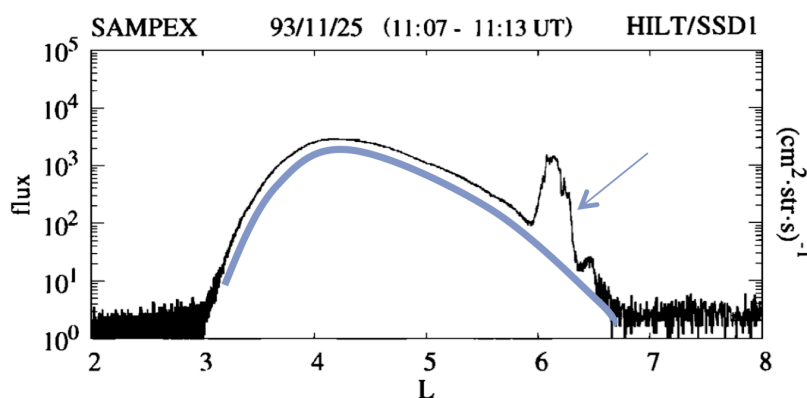
Figure 5.5   SAMPEX/HILT data from November 25, 1993 showing a strong precipitation enhancement at the outer edge of the outer radiation belt around L=6 (marked by the blue arrow). (Adapted from *Nakamura et al.,* 2000)

Precipitation bands have been observed during both quiet and more active times, spanning the afternoon and night sectors [*Brown and Stone*, 1972]. It has been suggested that those during times of high magnetic activity, often seen near the plasmapause, may be induced by electromagnetic ion cyclotron (EMIC) waves [*Vampola*, 1977; *Thorne and Kennel*, 1971], while those at quieter times may be associated with electrostatic waves or the trapping limit

[*Koons et al.*, 1972; *Vampola*, 1977; *Vampola*, 1971]. A number of open questions remain though regarding the distributions and generation mechanisms of these precipitation features, and how these vary with geomagnetic activity.

5.2.3 Automated Precipitation Identification

The first step towards investigating these rapid precipitation events was to identify the features in ~10 years of SAMPEX data (1996 – 2005) and set up a database to provide the framework for further studies. The features are identified based on their distinct durations and profiles: microbursts appearing as sharp spikes lasting less than a second, and precipitation bands as rapid enhancements in flux often remaining elevated for ~5-30 seconds. We have identified the microbursts using the following burst criterion developed by *O'Brien et al.* [2003]:

$$ - \left(N_{100} - A_{500} \right)/\sqrt{1 + A_{500}} > 10 $$

where N_{100} is the number of counts in 100 ms and A_{500} is a running average over 500 ms. Microburst magnitudes are then extracted by taking the difference between N_{100} and a baseline flux, defined as the 10th percentile in 3 second bins.

After much testing, an algorithm was also developed to detect band precipitation in the 100 ms SAMPEX/HILT data. We require:

- $N_{100} > 4$ x B_{20} for ≥ 5 seconds

- 10 second linear correlation coefficient between N_{100} and $B_{20} < 0.955$

where N_{100} is the instantaneous 100 ms count rate and B_{20} is the 10th percentile in 20 sec bins. Magnitudes are defined by the difference between N_{100} and this B_{20} value. The correlation coefficient requirement eliminates false detections from rapidly rising (falling) fluxes as the satellite enters (exits) the outer radiation belt. These criteria have been tuned to reduce false positives, however, this causes some smaller band events to go undetected. Figure 5.6 illustrates

example results of these two algorithms during two passes of SAMPEX through the outer radiation belt; we extract the time, location, duration, and magnitude of the microbursts and precipitation bands via these automated procedures.
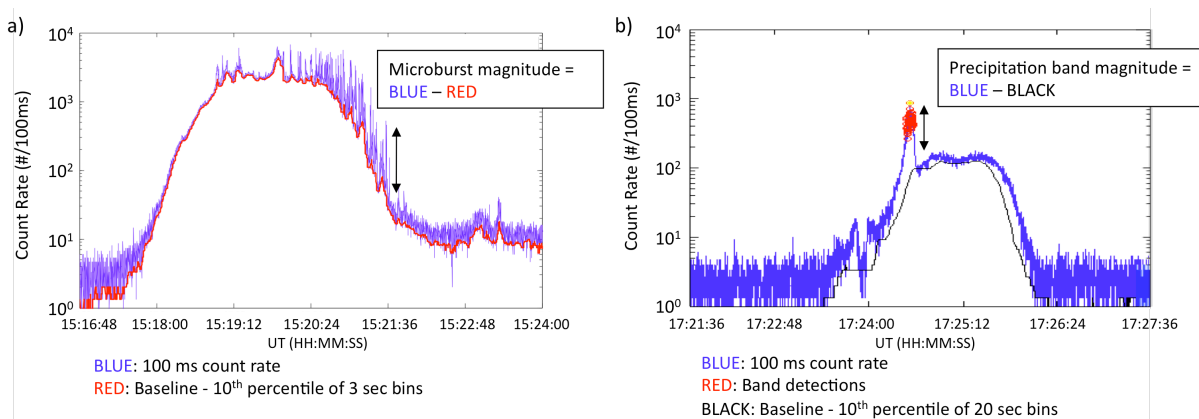
Figure 5.6 SAMPEX/HILT >1 MeV electron measurements during two passes through the outer radiation belt. Rapid enhancements in the flux are visible on millisecond (a) and longer duration (b) timescales. Results of an automated detection and magnitude calculation algorithm for microbursts (a) and precipitation bands (b) are shown.

With these two selection methods, we have created a database of both microbursts and precipitation bands from the SAMPEX/HILT SSD4 data from 1996 through 2005. After establishing this database, some preliminary studies are performed to investigate the spatial and storm-time distributions of these two types of rapid precipitation, described in the following sections.

5.3 Spatial Distributions of Rapid Precipitation Events

With the database of precipitation events described in Section 5.2.3, we are now able to investigate the spatial distributions of microbursts and precipitation bands. We look at both the occurrences and magnitudes of these two precipitation features across geographic latitude and longitude, as well as local time and L shell.

Figure 5.7 shows the magnitude of the flux measured by SAMPEX/HILT at all times (a), during microbursts (b), and during precipitation bands (c) across geographic latitude and longitude from 2003 through mid-2004, the end of the primary mission. Panel a illustrates the variations in trapped flux measured by a LEO satellite due to the longitudinal asymmetries of Earth's internal magnetic field. Outer radiation belt electrons are measured at high latitudes, while inner belt particles are measured only when the satellite passes over the SAA (at longitudes ~300-360°). The microburst and precipitation band magnitudes do not follow this same pattern in flux variation; instead the largest magnitude precipitation events, with fluxes ~10^4, are scattered throughout the outer radiation belt at all longitudes and in both hemispheres. This acts as a further confirmation of the general isotropization during these precipitation features, as otherwise one would expect their magnitudes to have a similar geographic dependence as in Figure 5.7a.

Figure 5.8 shows scatter plots of the location and magnitudes of microbursts (a) and precipitation bands (b) for this same year-and-a-half period now across magnetic local time (MLT) and L shell, calculated using the IGRF field model. Microbursts are clustered on the morning side, between midnight and noon, in good agreement with past statistical findings [*Lorentzen et al.,* 2001a]. Occurrences remain constrained primarily between L=4-6, indicated by the dashed circles, and magnitudes vary across this whole region and all local times.

The precipitation bands on the other hand, occur primarily on the evening and night sides, again in good agreement with past surveys (e.g. *Imhof et al.,*1986). This agreement in spatial distribution between our findings and other studies helps confirm our precipitation detection criteria. Magnitudes are observed to peak between 18 and 24 MLT and drop off with increasing L. The difference in the spatial distributions of the two precipitation types is quite distinct here,
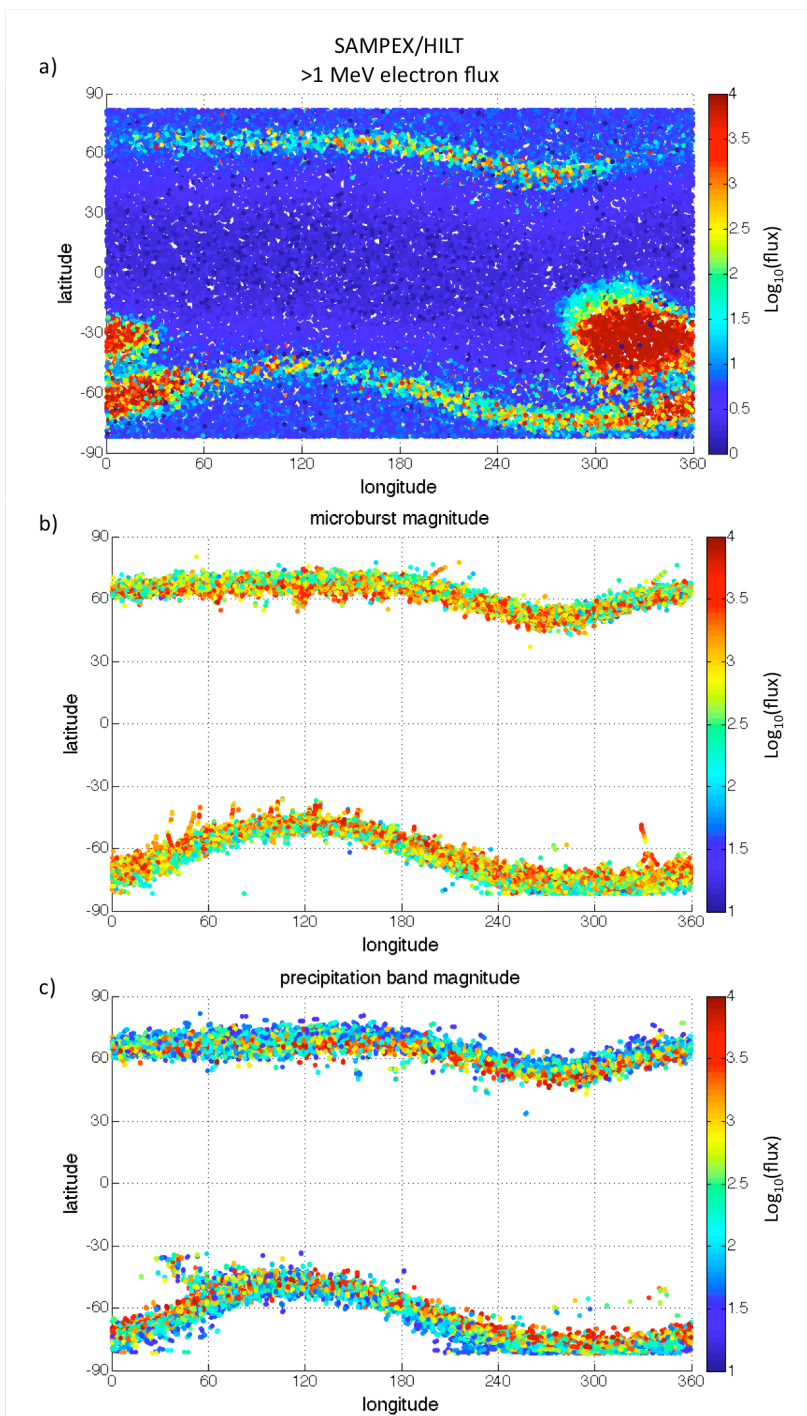
Figure 5.7 (a) Distribution of the >1MeV electron flux measured by SAMPEX/HILT over geographic latitude and longitude. The magnitudes of microbursts (b) and precipitation bands (c) are also shown across these coordinates.

suggesting that these precipitation features are caused by different scattering mechanisms or wave modes. While there are fewer small magnitude microbursts as compared to the precipitation bands, this is likely due to our selection criteria.
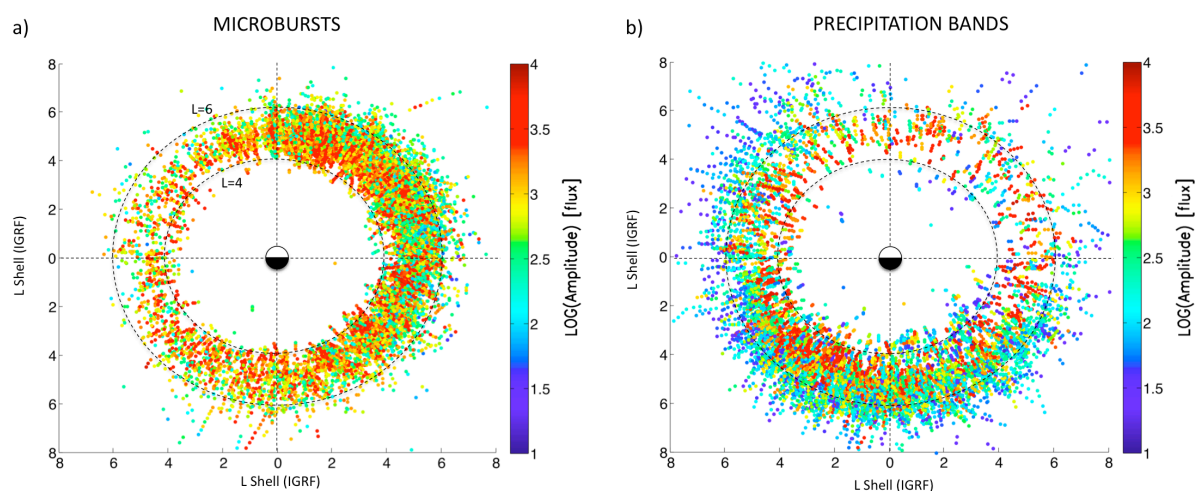
Figure 5.8 Distributions of microbursts (a) and precipitation bands (b) in L shell and magnetic local time (MLT). Precipitation magnitude is shown on the color scale. These data are collected from 2003-mid 2004, the end of the primary mission. The events are searched for within the same data set, so local time differences between the two precipitation types are not due to sampling.

While other studies have also investigated MeV precipitation events, selection criteria or the nature of the observations often differ, making it difficult to determine whether the same phenomena are being examined. Balloon campaigns have observed MeV electron precipitation at low altitude, constrained primarily to the duskside and thus termed "duskside relativistic electron precipitation" or DREP [*Millan et al.,* 2007]. As compared to LEO satellites, which cut across L shells at ~7 km/s, balloon measurements are relatively stationary, remaining at roughly constant geographic coordinates. The DREP events last minutes to hours as seen by balloons and, while precipitation events were observed at all local times by the MAXIS balloon campaign [*Millan et al.*, 2002], the harder MeV events occurred exclusively on the dusk side (see Figure 5.9). *Comess et al.* [2013] have also surveyed SAMPEX data for "REP" events, using data only

when the spacecraft is conjugate to the SAA and measuring purely bounce loss cone electrons, rather than selecting on the band-like features in the data as we have done. They find similar occurrence distributions in L and MLT to those shown here, with these studies all suggesting that MeV electron precipitation occurs preferentially in the dusk sector. What the structure of that precipitation is, as well as the exact relation between balloon measured "DREP" and the precipitation bands seen by LEO satellites, will be investigated further in Chapter 7.
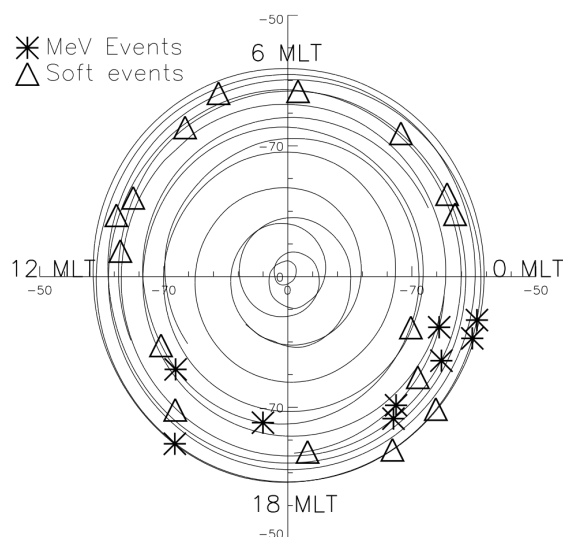
Figure 5.9 The distribution in magnetic latitude and magnetic local time of MeV events (asterisks) and soft precipitation (triangles) measured by the MAXIS balloon campaign. Noon is to the left now, and the solid line shows the balloon trajectory. (From *Millan et al.*, 2002)

5.4 Storm-Time Precipitation Distributions

We next explore how these precipitation features, both their occurrences and magnitudes, evolve in time during periods of changing geomagnetic activity, looking both at individual events as well as a set of high speed stream (HSS) driven storms.

5.4.1 Event Studies

We look in detail at a few individual storms to investigate the location and magnitude of precipitation bands and microbursts in relation to other plasma populations and magnetospheric phenomena. In particular, we investigate an event in June 2001, which was selected by the Plasmasphere-Magnetosphere Interactions focus group at the Geospace Environment Modeling (GEM) 2012 workshop as a GEM challenge event. A small disturbance occurred on June 9th, with Dst reaching a minimum of ~ -40 nT around 21:00 UT. During this period, the IMAGE satellite provided global images of the plasmaspheric dynamics and there are a number of in situ and ground based wave measurements available. Figure 5.10 shows the distributions of microbursts and precipitation bands surrounding this event in L shell and UT (Figure 5.10a) as well as MLT (Figure 5.10b). Local time sampling of SAMPEX during this period was restricted
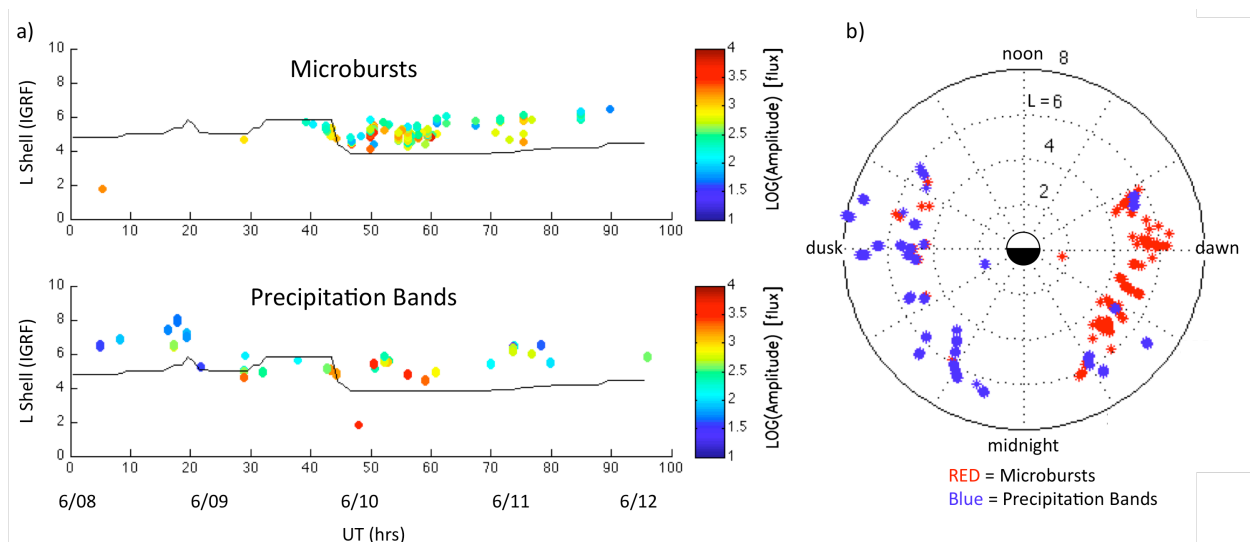
Figure 5.10 The magnitudes and distributions of microbursts and precipitation bands across (a) universal time, in hours since 06/08 00:00, and (b) MLT for an event in early June, 2001.

to the dawn and dusk. A Dst-dependent model for the plasmapause location [*O'Brien and Moldwin*, 2003] is overplotted as well (black solid line). The local time distributions of the two precipitation types, as well as their relation to the plasmapause location, again suggest different

source regions and mechanisms for the pitch angle scattering.

We look briefly at the source region of the precipitation bands during this event to help determine the scattering mechanism causing these precipitation signatures. Ground magnetometers in Antarctica (data courtesy of Mark Engebretson) show Pc1-2 activity occurring in the afternoon sector during this event, where EMIC waves often develop as the ring current overlaps the cold, dense plasmaspheric bulge or plume [*Spasojevic et al.*, 2004]. Geosynchronous satellites from the Los Alamos National Laboratory (LANL), measuring the equatorial source regions for EMIC waves, saw plasma conditions indicative of EMIC wave growth [*Blum et al.*, 2009] during passes through the afternoon sector, and *Chen et al.* [2014] find simulations of EMIC wave growth to be in this region as well (see Figure 3.11). We find good general agreement in the universal and local time of precipitation bands and EMIC waves during this event, in support of the theory that EMIC waves may be one main scattering mechanism responsible for producing these precipitation signatures [*Vampola*, 1977; *Thorne and Kennel*, 1971]. While the precipitation bands tend to appear close to the plasmapause, as inferred from the MLT-independent *O'Brien and Moldwin* [2003] model, further investigation of the location of the precipitation bands with respect to the measured global plasmapause and plasmaspheric plumes from IMAGE may shed light on the cause of the structure of these radially narrow precipitation features.

We have also looked at two other individual storms of varying size. Rapid precipitation distributions are shown for a small storm, Dst_{min} ~-40 nT (Figure 5.11a) as well as a major coronal mass ejection (CME) driven event in November 2003 with Dst_{min} ~-450 nT (Figure 5.11b). As a rough estimate of the relative loss due to microbursts as compared to precipitation bands, we sum the magnitudes of the precipitating count rates to estimate the average loss rate as
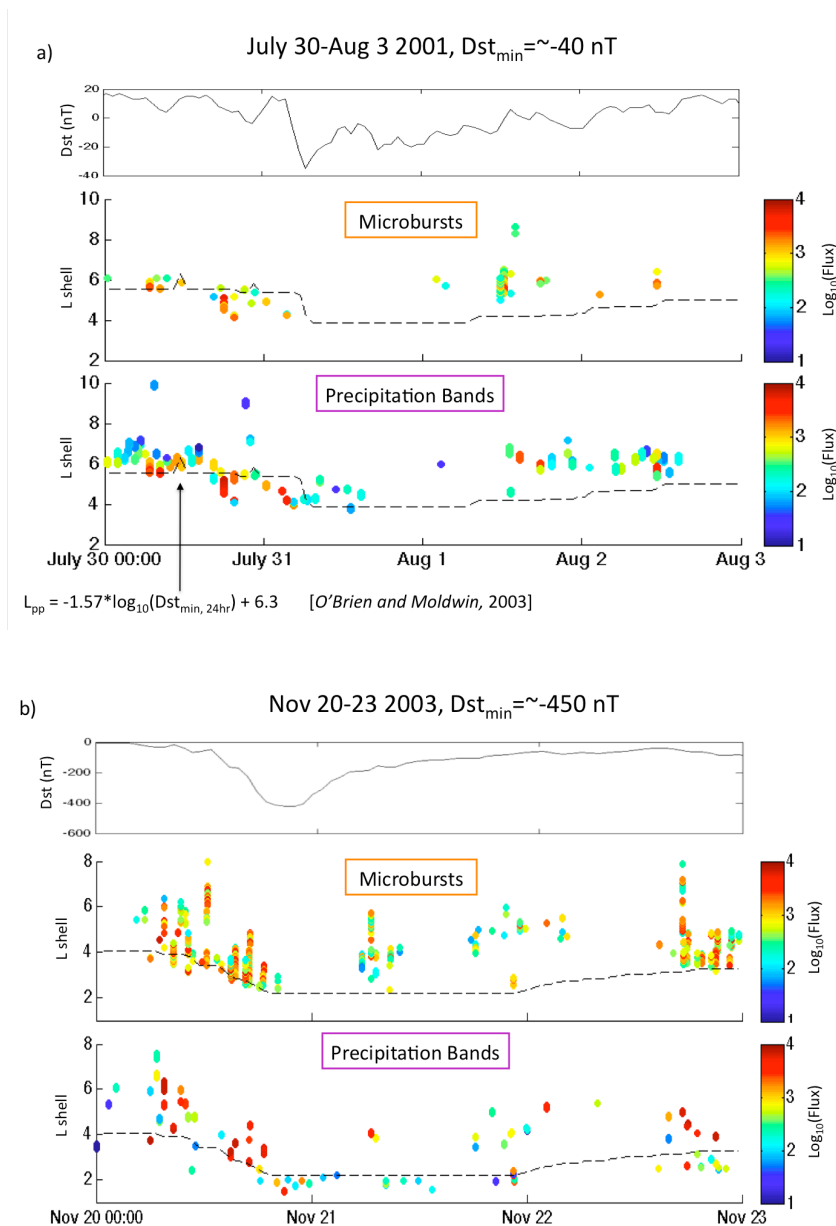
Figure 5.11 Dst (top panel), microburst magnitude (middle), and precipitation band magnitude (bottom) across L shell and time during two geomagnetic storms – a small storm in 2001 (a) and much larger superstorm in Nov 2003 (b). A model for the plasmapause location is plotted with the dashed black line.

well as total loss, as measured along the SAMPEX orbit, for the main and recovery phase of each storm. Table 5.1 displays these relative loss rates, as well as the total loss summed during each storm due to each precipitation type. While general trends are apparent among all three storms

shown here (increasing precipitation band magnitude during the main phase, microbursts constrained outside the plasmasphere, etc.), the overall occurrence of the events, as well as the relative occurrences and magnitudes of microbursts versus precipitation bands, varies tremendously. During the July-Aug 2001 storm, precipitation bands dominate the loss by an order of magnitude over microbursts, while during the Nov 2003 storm they are larger by only a factor of two. The total loss due to microbursts increases by an order of magnitude from the smaller Dst_{min}~-40 nT 2001 storm to the large Dst_{min}~-450 nT 2003 storm, showing a relation between storm size and microburst losses. Precipitation band loss on the other hand is similar between these two storms, indicating that even during relatively small storms this mechanism can produce significant loss. These findings emphasize the need to understand how the distributions and magnitudes of rapid precipitation events vary for different types of storms and storm phases.

Precipitation Type:	Main Phase:	Recovery:	Total Loss:
July 30-Aug 3 2001 Storm (Dst_{min}=~-40 nT)			
Microbursts	27 e-/s	115 e-/s	44 x 10^6 e-
Precipitation Bands	2700 e-/s	190 e-/s	600 x 10^6 e-
Nov 20-23 2003 Storm (Dst_{min}=~-450 nT)			
Microbursts	6000 e-/s	195 e-/s	400 x 10^6 e-
Precipitation Bands	9000 e-/s	1000 e-/s	700 x 10^6 e-

Table 5.1 Precipitation rates due to microbursts and precipitation bands during main and recovery phases of the two storms shown in Figure 5.11.

5.4.2 Superposed Epoch Study

As shown in the previous section, the relative occurrences of both precipitation bands and microbursts, as well as their magnitudes, can vary dramatically from storm to storm. We choose

next to focus on a single storm type and, using superposed epoch technique, to look for systematic patterns in rapid precipitation events across storm phase as well as L shell. A set of 41 high speed stream (HSS) driven storms from 2003-2005 are investigated, selected from a larger list of HSS storms originally studied by *Denton and Borovsky* [2008] and introduced earlier in Chapter 4. Characteristic dropouts are observed during the main phase of these storms, followed by a subsequent build up of outer belt fluxes a few days later. A number of studies have attempted to determine the cause or causes of these dropouts. Studying the plasma conditions measured at GEO during these events, *Borovsky and Denton* [2009] suggest high ring current density and anisotropy, concurrent with extended plasmaspheric plumes on the duskside during the main phase, could contribute to EMIC wave growth and relativistic electron scattering associated with the observed dropouts in the trapped population. *Morley et al.* [2010] find the magnetopause remains beyond $\sim 8 R_E$ during a similar set of HSS from 2005-2008, suggesting that other mechanisms must be producing the losses seen across the entire outer belt, down to L shells of ~ 3. *Meredith et al.* [2011] look at precipitating electrons seen by POES satellites at LEO during a subset of these same HSS storms, however, and find little indication of significant MeV loss to the atmosphere. Finally, *Hendry et al.* [2012] use ground instrumentation, sensitive to $\sim$10s-100s keV electrons, to quantify precipitation instead and find that the precipitating flux inferred by the ground measurements can be $\sim$10x larger than that observed by POES.

Figure 5.12 shows the superposed results from the *Meredith et al.* [2011] study, comparing >1 MeV count rates measured by the POES 90° telescope (panel a) and 0° telescope (panel b), superposed at storm convection onset. The POES Medium Energy Proton and Electron Detector (MEPED) instrument used here has 3 electron channels, >30keV, >100keV, and >300 keV [*Evans and Greer*, 2004]. However, its highest energy proton channel has been

shown to be sensitive to electrons > ~1MeV [*Yando et al.,* 2011] and is thus often used for radiation belt studies during times when solar proton events are not occurring. The MEPED instrument consists of two 30° field of view telescopes, one looking roughly along the field line (0° or T0) and one looking perpendicular (90° or T90). The 90° telescope responds to trapped and drift loss cone electrons, while the 0° one measures precipitating electrons. However, with its 30° field of view, this telescope covers only a small fraction of the total loss cone, anywhere from 2-10% [*Hendry et al.,* 2012]. Additionally, count rates have two-second resolution, so POES is not able to detect more rapid microburst precipitation. For these reasons, we look to see if SAMPEX/HILT, with its large geometric factor and field of view and high time resolution, can reveal anything more regarding precipitation loss during these HSS storms.
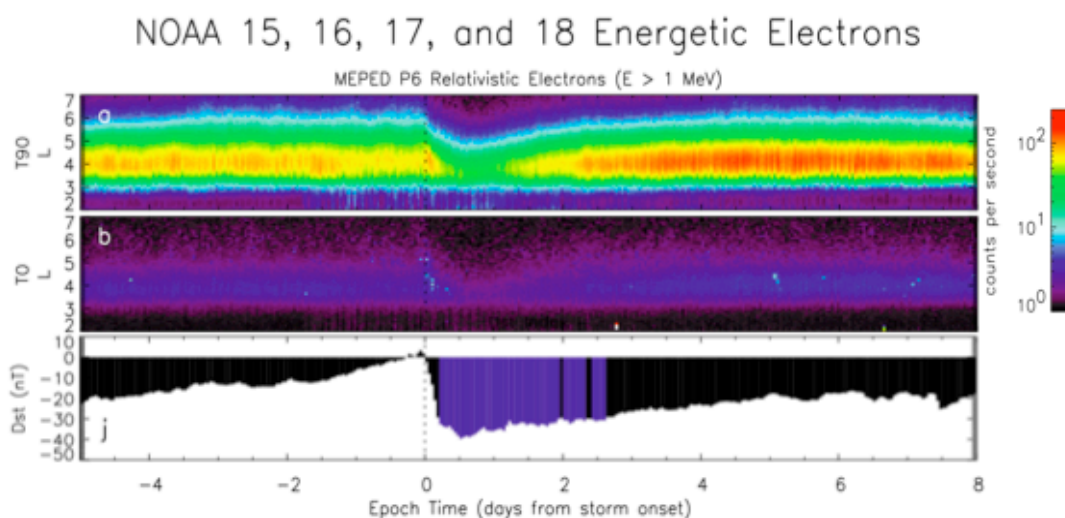
Figure 5.12 Superposed POES energetic electrons and Dst index during 42 HSS-driven storms. (Adapted from *Meredith et al.,* 2011)

Using our database of rapid precipitation features from Section 5.2.3, a statistical study is performed to investigate the distributions of energetic electron microbursts and precipitation bands during HSS storms across L shell and storm phase, looking both at occurrence rates as well as magnitudes of the precipitation types. Figure 5.13 shows the distributions of the rapid,

milliseconds-long microbursts (left panels), as well as the longer duration precipitation bands (right panels), with respect to L shell and epoch time, over 41 HSS-driven storms. While microburst occurrence rates increase dramatically during the recovery phase period, the magnitudes remain fairly independent of storm phase. The precipitation bands, on the other hand, show an increase in magnitude right around zero epoch as well as through the recovery phase, especially at lower L shells.
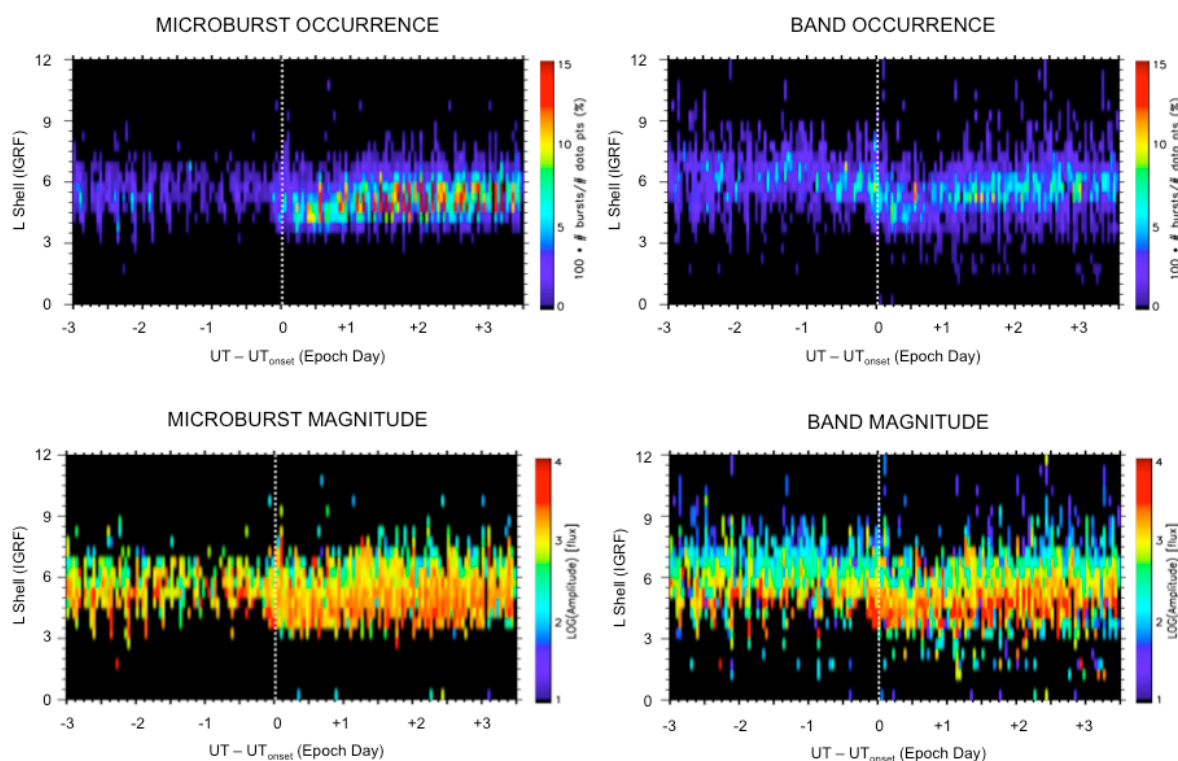
Figure 5.13 Superposed epoch results from 41 HSS-driven storms in 2003-2005. Occurrence rates (top panels) and magnitudes (bottom) are shown for microbursts (left) and precipitation bands (right) across L shell and storm phase, or epoch time.

Certain patterns are observable here, indicative of the role microburst and precipitation band losses play during these HSS-driven events. Microburst activity shows a dramatic increase during these storms, beginning in the main phase but continuing through the recovery as the trapped outer belt fluxes are built back up. More detailed investigations into the timing and

magnitude of this process must be performed to determine the balance between acceleration and loss that these features may indicate. It appears, however, that magnitudes do not vary much across storm phase, in contrast to the patterns observed by *O'Brien et al*. [2004] during three large CME driven storms, which showed microburst magnitudes peaking during storm main phase. The observed increase in precipitation band magnitude around zero epoch is consistent with enhanced EMIC wave activity during this time, as suggested by *Borovsky and Denton* [2009], as well as the *MacDonald et al.* [2010] study discussed briefly in Chapter 4, and suggests this mechanism may play a role in the main phase losses observed throughout the outer belt, especially at lower L shells. These findings also suggest that POES does not fully capture the loss of MeV electrons to the atmosphere occurring during these events, in agreement with ground observations of lower energy electron precipitation.

5.5 Summary

Here we have used the extensive SAMPEX/HILT database to study rapid precipitation events, their spatial distributions, and their relation to storm-time radiation belt dynamics. In particular, millisecond-long microburst precipitation as well as longer duration precipitation bands are investigated. Using automated criteria to detect these features, in the SAMPEX/HILT >1 MeV database, we perform both statistical and event studies to better understand the relative contributions of these precipitation events to radiation belt losses.

Local time occurrence distributions find microbursts constrained to the morning side of the magnetosphere, between L shells of 4-6, in good agreement with measured whistler mode chorus wave distributions in the inner magnetosphere. Precipitation bands have a peak both in magnitude as well as occurrence rate on the dusk and night side, strongest from 18-24 MLT. While they extend across a somewhat larger range of radial distances, L~3-8, band magnitudes

are significantly lower at these further radial distances. These distributions shed light on the potential scattering mechanisms causing these features, and support past hypotheses of whistler mode wave scattering producing microbursts and EMIC wave activity responsible for some precipitation bands.

Investigation of the storm-time distributions of microbursts and precipitation bands help illuminate both when and where the different precipitation mechanisms contribute most to radiation belt depletions. Here we've investigated distributions of these rapid precipitation features and shown that they play a clear role in storm-time radiation belt dynamics. Event studies indicate that the relative roles of these two precipitation mechanisms can vary tremendously during different storm types and phases, and that these losses are not necessarily directly related to storm magnitude. In a superposed epoch study of 41 HSS-driven storms, we find evidence for significant atmospheric losses and propose that large geometric factor and field of view measurements as well as high time resolution are necessary to fully capture this loss. This work not only pins down the role precipitation plays in radiation belt losses, but also which type of precipitation is active and when.

Chapter 6: New CubeSat Measurements to Study MeV Electron Dynamics

The following chapter includes work that was published in Blum and Schiller (2012), Characterization and testing of an energetic particle telescope for a CubeSat platform, *Small Satellite Conference,* AIAA/USU, SSC12-VIII-4.

6.1 Introduction: The CSSWE CubeSat

The Colorado Student Space Weather Experiment (CSSWE) is a Cubesat designed and built by University of Colorado (CU) students, launched in September 2012 and still returning data. With reentry of the SAMPEX satellite in November 2012, after 20 years of operation and valuable data return, this CubeSat provides new, differential measurements of MeV electrons at low altitude to continue investigation of radiation belt losses to the atmosphere. Additionally, with the successes of the Van Allen Probes, launched August 2012, and the BARREL balloon campaigns in Jan-Feb 2013 and 2014, a constellation of radiation belt monitors are currently providing multipoint measurements at a wide range of locations within the inner magnetosphere. Using data from the CSSWE CubeSat, in conjunction with other new missions and measurements, we can continue to study MeV electron precipitation.

This CubeSat project has provided me with invaluable hardware and management training as well as the unique experience of seeing a space flight hardware project from design and testing through launch and data analysis phases. As this was a large team effort including over 60 students and professionals, I would like to acknowledge and thank all the team members involved. My initial involvement in this project was as a team member on the Electrical Power System and Science Instrument subsystems, testing solar cells and instrument electronics and

designing a test plan for the instrument detectors. In January 2011 I took over as Ground Station Lead and that May as Project Manager of the team. I have acted in these roles for the past three years, seeing the project through flight build, system testing, delivery, launch, and operations. In the following sections, I give an overview of the system as a whole, as well as some more detailed information regarding the science payload onboard. In particular, I include aspects of the system design and performance that have directly affected our data processing and interpretation of the scientific measurements. Additionally, I try to highlight here the specific areas in which I had a direct role. Having been involved in these earlier stages of the project helped inform my analysis of the CubeSat data and my understanding of the instrument capabilities and limitations. On all accounts the project has been a huge success, demonstrating not only the value of CubeSats as educational tools but also that valuable scientific measurements can be achieved from such small platforms.

6.2 Mission and System Overview

The CSSWE CubeSat, for which Xinlin Li is the principal investigator (P.I.) and Scott Palo a Co-P.I., was designed and built primarily by students at the University of Colorado, with advising from CU and Laboratory for Atmospheric and Space Physics (LASP) professionals. Funded by the National Science Foundation (NSF) for $840,000 over the course of three years, starting in January 2010, the CubeSat was delivered January 2012 for integration as a secondary payload onto an Atlas-V launch vehicle, and launched September 13, 2012 into a high inclination, low altitude orbit. Mission operations were performed by students using a ground station and control room at LASP built specifically for the project. CubeSat beacons were received and decoded on the spacecraft's first pass over Boulder following deployment. A timeline of the project is provided in Figure 6.1.
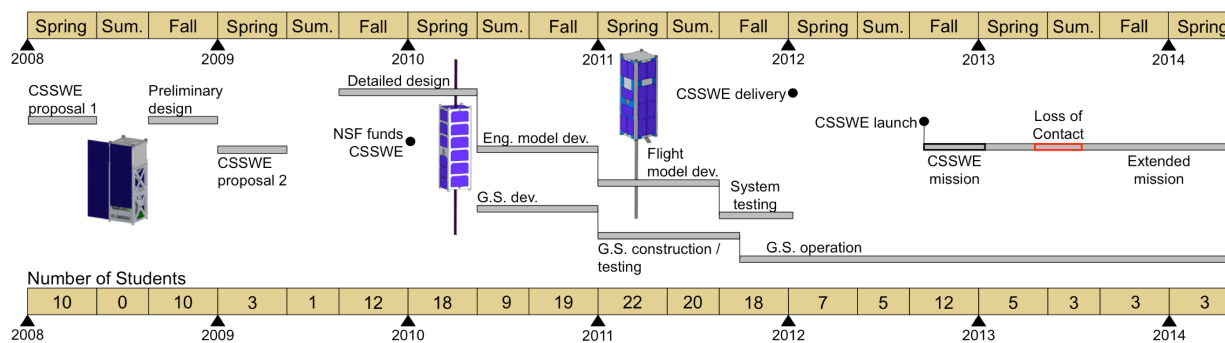
Figure 6.1 A timeline of the CSSWE mission, from design through build of both the CubeSat and Ground Station (G. S.) at LASP, through launch and operations.   The extended mission is continuing through the present time (as of June 2014).

CSSWE was designed to address critical space weather questions. The sole science payload onboard is the Relativistic Electron and Proton Telescope integrated little experiment (REPTile) instrument, which measures protons in the energy range of 9 - 40 MeV, and electrons from .58 - >3.8 MeV in differential energy channels. This instrument is a miniaturized, simplified version of the Relativistic Electron and Proton Telescope (REPT) instrument [*Baker et al*., 2012] designed and built at LASP onboard NASA's Van Allen Probes [*Kessel et al.*, 2012]. From its low altitude, high inclination orbit, CSSWE measures both trapped and precipitating MeV protons and electrons from the radiation belts as well as solar energetic particle events.

The project employed a "keep it simple" approach combined with rigorous system testing to minimize risks associated with low budget, student-built projects. Commercial off-the-shelf (COTS) components and subsystems were used where possible. Attitude is maintained with a passive magnetic attitude control (PMAC) system, consisting of a small bar magnet and six hysteresis rods [*Gerhardt et al.,* 2010]. This system aligns the long axis of the spacecraft with the background magnetic field to within ~15°, to both improve the RF communication link with the ground station as well as for instrument science requirements. Except for battery heaters, thermal control is passive as well, relying on thermal radiative apertures to release heat from the

electronics stack. Numerous full system tests were performed prior to delivery, including vibration testing, a 10-day 8-cycle thermal vacuum (TVAC) test, and "day-in-the-life" testing of full functionality over the RF link. The robust design and thorough testing helped verify on-orbit performance and build confidence in the success of the system.

6.3 Instrument Design

General design of the instrument and instrument electronics began in 2008-2009 and was already largely determined when I joined the project in Fall 2010. However, much testing and characterization of the instrument performance was still needed. Instrument Scientist Quintin Schiller and Instrument Electronics Lead Abhishek Mahendrakumar led these efforts with advising from LASP professionals Vaughn Hoxie and Chris Belting. As a team member on the Instrument subsystem, I participated in much of this testing, including electronics component performance characterization, detector test plan development, and discussions regarding the science drivers behind design requirements and decisions. The challenges of miniaturizing an instrument to fit within the constraints of a CubeSat dictated a number of the REPTile design features. Strict mass and volume budgets for CubeSats restrict REPTile's size, and the resulting space, power, and data transmission limitations played a large roll in the design of the electronics. Thus, careful preflight testing and calibration was all the more critical to understanding and optimizing instrument performance.

The REPTile instrument is a loaded-disc collimated telescope designed to measure energetic electrons and protons with a signal to noise ratio of two or greater. The instrument consists of a stack of four solid-state doped silicon detectors manufactured by Micron Semiconductor. The front detector has a diameter of 20mm, while the following three are 40mm across. The detector stack is housed in a tungsten (atomic number Z=74) chamber, which is

encased in an aluminum (Z=13) outer shield. Tantalum (Z=73) baffles within the collimator

prevent electrons from scattering into the detector stack from outside the instrument's 52° field

of view, and give the instrument a geometric factor of 0.52 sr·cm^2. The materials were chosen

based on a combination of their ability to shield energetic particles and minimize secondary

electron generation within the housing. The 0.5mm thick beryllium foil at the front of the

detector stack acts as a high-pass filter, stopping all electrons < 400keV and protons < 8MeV

(see Figure 6.2 for the instrument geometry). The total instrument mass is 1.25kg, with a

cylindrical envelope of 4.6cm (diameter) x 6.0cm (length). As beam testing was not within the
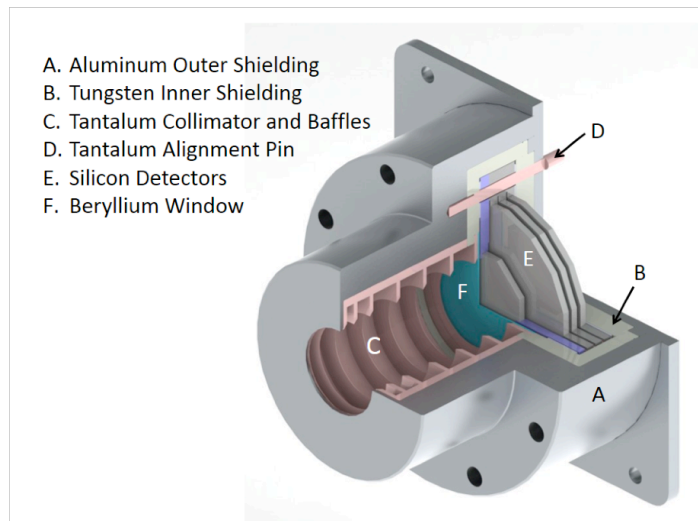
Figure 6.2 A Solidworks rendering of the REPTile instrument onboard CSSWE.

$840,000 budget of the CubeSat, detailed modeling of the instrument, as well as radioactive

source testing, was conducted to characterize its performance [*Schiller and Mahendrakumar*,

2010; *Blum and Schiller*, 2012]. The PMAC system maintains the boresight of the instrument

pointing roughly perpendicular to the background magnetic field, so measurements are

dominated by locally mirroring particles.

The REPTile electronics system acts to process and interpret the signals coming from the

detectors and calculate electron and proton count rates in each of the four energy channels. A block diagram of the signal chain is depicted in Figure 6.3, showing the stages the signal passes through before count rates are calculated. The chain is duplicated for each of the four detectors.

When a particle hits a detector, it produces a shower of electrons in the silicon. This charge pulse is collected on the anode and passed to a charge sensitive amplifier (CSA), which acts to amplify the signal and convert it to a shaped voltage pulse. The CSA selected was the A225 from Amptek Inc., which is a space grade component but very sensitive to noise and other environmental factors. Due to this sensitivity, a number of measures were taken to remove background noise from the signal. Details on the testing and correction methodologies are discussed in Section 6.5.
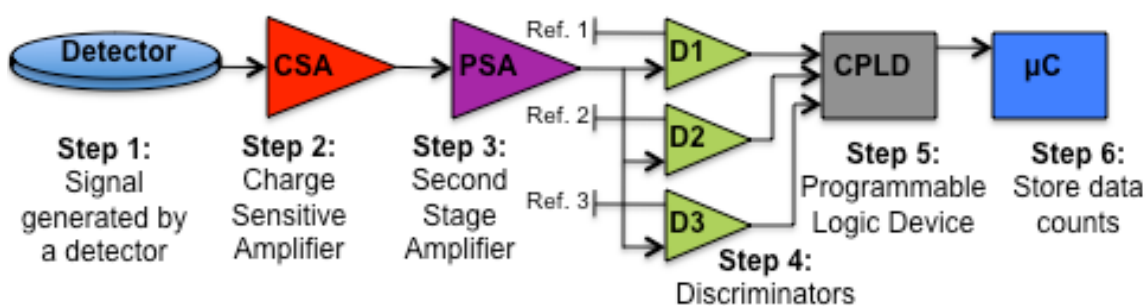
Figure 6.3 Instrument electronics block diagram. (From *Blum and Schiller*, 2012)

Following the CSA, a secondary amplification is performed by a pulse-shaping amplifier (PSA), which amplifies the signal by 3.4x and further shapes it. The output of this stage ranges from ~0-4V depending on the species and energy of the incident particle. These voltages are passed into a three-stage discriminator chain, which is used to identify whether the particle is an electron or proton based on the voltage measured. Each discriminator compares the output of the PSA to a predefined reference voltage. The reference voltages are set to 0.29, 1.35, and 3.88 V, equivalent to energy deposition in the detectors of 0.25, 1.5, and 4.5 MeV respectively, and are

adjustable from the ground during operations. The first discriminator in the chain returns a 1 if the input voltage exceeds the equivalent of 0.25 MeV deposited in the detector, and a 0 otherwise. The second returns a 1 when the second voltage threshold is exceeded, and similarly for the final discriminator and third threshold. Thus a discriminator chain output of 100 indicates a particle has deposited 0.25-1.5 MeV in a given detector.

In the final signal processing stage, the Complex Programmable Logic Device (CPLD) interprets the discriminator values and classifies the particle by species and energy. Particles depositing between 0.25 and 1.5 MeV in a detector are classified as electrons, and those depositing > 4.5 MeV as protons. Discriminator outputs of 1.5 – 4.5 MeV are discarded, as this energy range is contaminated by both electrons and protons. The number of detectors a particle hits determines the energy of the particle, as described by the binning logic applied by the CPLD. 6-second count rates are calculated for each energy channel for both electrons and protons, and these rates are passed on to the Command and Data Handling (C&DH) system to be stored and transmitted down to the ground.

Instrument commissioning began in early October 2012, a few weeks after launch, and consisted of turning on the high voltage to each detector one at a time. After a few days, it was determined that the third detector was not behaving properly, so it was turned off for the remainder of the mission. The onboard binning logic was designed to account for failure of one detector, so CSSWE returns three energy channels per species rather than the four originally designed. The current in-flight instrument energy channels as well as the four original channels are listed in Table 6.1.

Pre-Launch Energy Channels:				
Species:	Channel 1	Channel 2	Channel 3	Channel 4
Electrons	0.5-1.5 MeV	1.5-2.2 MeV	2.2-2.9 MeV	>2.9 MeV
Protons	8.5-18.5 MeV	18.5-25 MeV	25-30.5 MeV	30.5-40 MeV
Post-Launch Energy Channels:				
Species:	Channel 1	Channel 2		Channel 3
Electrons	0.58-1.63 MeV	1.63-3.8 MeV		>3.8 MeV
Protons	9-18 MeV	18-30 MeV		30-40 MeV

Table 6.1 REPTile energy channels pre- and post-launch.

6.4 Ground Station and Operations

To operate the CSSWE CubeSat and collect data, a ground station was built specifically for the mission on the rooftop of LASP. Trade studies had been performed and equipment selected and purchased when I took over as Ground Station Lead in January 2011. My main responsibilities were thus to construct the ground station, test it thoroughly, and coordinate mission operations after launch. This included installing the hardware both on the roof of LASP and in the control room, and testing the antenna tracking and alignment as well as the communication link between the ground station and onboard CubeSat radio.
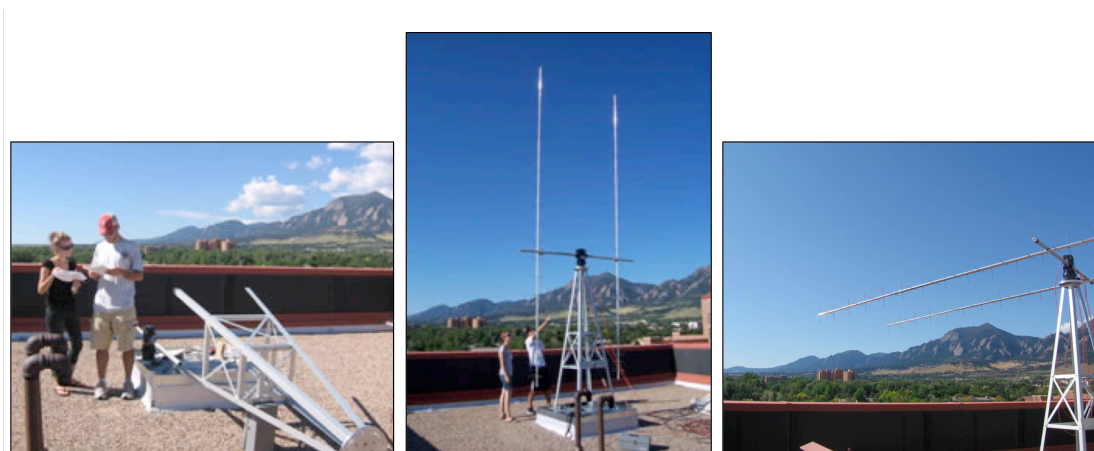
Figure 6.4 CSSWE ground station antennas during construction on the LASP rooftop.

The CSSWE ground station operates in half-duplex mode, communicating at a rate of 9.6 kbps at 437.345 MHz (UHF) for the uplink and downlink, the frequency designated to us by the International Amateur Radio Union (IARU). Commands are packetized and sent through Instrument and Spacecraft Interface Software (ISIS), commanding software that was inherited by LASP from the NOAA GOES-R program and has been customized for our uses. The Kantronics KAM XL terminal node controller (TNC) modulates/demodulates the signal, and the Kenwood TS-2000 radio is used to communicate at the UHF band. Two 18 foot M2 436CP42 cross Yagi antennas are used, each with a gain of ~17 dBdc and a circular beamwidth of 21°. The antennas are pointed using a Yaesu G5500 azimuth-elevation rotator controlled by SatPC32, a software package developed for use with amateur satellites. This program also controls radio frequency to account for Doppler shift during passes. The antennas and rotator are mounted on an 8-foot tower installed on the LASP roof and connected to the ground station control room with just over 200 ft of low-loss cabling, adding a total of - 5.4dBm loss to the RF signal. A block diagram of the ground station command and control chains is illustrated in Figure 6.5.

The ground station was fully tested before CubeSat delivery and launch, and was used to command the satellite in a simulated on-orbit scenario. We successfully sent commands and received data over the RF link with the CubeSat at an off-site location running off of its battery and solar panels, with attenuators in the signal chain to simulate on-orbit losses. The ground station continued to be tested after delivery with a functionally identical, spare version of the satellite (our "flatsat") built specifically for testing and calibration purposes. Tracking capabilities and antenna alignment were also confirmed by tracking, listening to, and decoding beacons from other spacecraft already in orbit, including University of Michigan's RAX2

CubeSat. Local HAM Radio operators Rick Kile and Rob Strieby helped us test and debug the system.
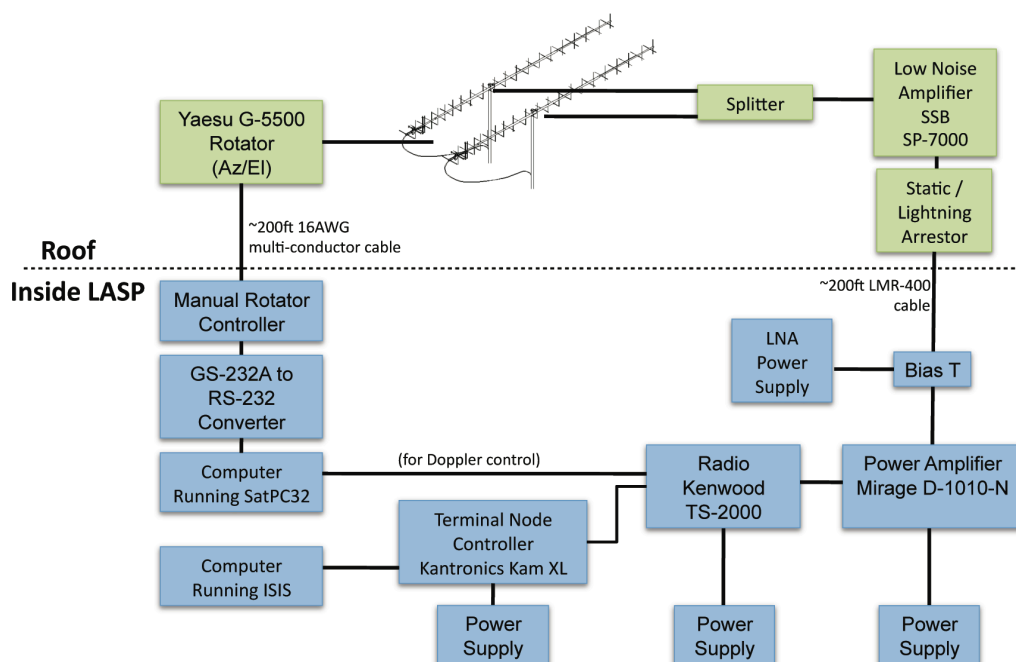
Figure 6.5 Ground station block diagram. (From *Li et al.,* 2012)

The operations team was composed of a handful of undergraduate and graduate CU students, with whom we developed a commissioning plan and manned passes (~6 per day) during the primary mission. Beginning in December 2012, CSSWE Systems Engineer David Gerhardt developed and implemented an Automated Commanding System to command and control CSSWE during passes without any human involvement. This system has been critical to our continued operations of CSSWE and has helped maximize the data we are able to retrieve. While our ground station is the only one able to send commands to CSSWE, stations around the world have helped track and collect beacons from our CubeSat. This was particularly helpful during the first few weeks after launch while we were trying to determine the object number and two line element (TLE) of our orbit and determine the system state of health.
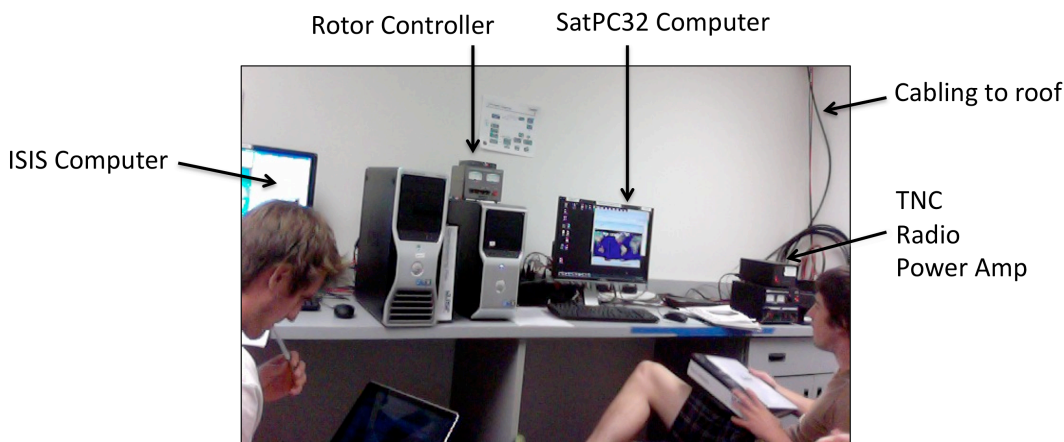
Figure 6.6 Ops team members Colin Stewart (left) and Wayne Russell (right) running a pass in the CSSWE ground station control room.

6.5 Data Processing

After colleting REPTile measurements, a number of processing steps are necessary before the data can be used. In particular, noise due to RF transmission and high temperatures must be removed. Additionally, count rates are corrected for saturation effects during periods of high fluxes. These processing steps are briefly outlined below to give better insight into the measurements obtained from REPTile. As instrument scientist, Quintin Schiller has developed the code to process raw instrument counts and convert them into flux. Sam Califf has also contributed by calculating the ephemeris data, including L shell and MLT, from the CubeSat two line elements (TLEs). As Project Manager I coordinated many of the system tests, such as TVAC, which alerted us to some of these potential noise sources. I have also been involved in some of these data processing steps, determining what features must be removed or corrected for and, through discussions and testing, how best to do so.

The raw, 6-second count rates received on the ground are processed to remove transmission noise by deleting data points within 12 seconds of a transmission event. This noise,

prior to removal, can be seen in Figure 6.7 as the red dots scattered above North America that clearly stand out from the measured outer belt fluxes. These transmission events contaminate some of our measurements of outer radiation belt electrons, particularly in the area above Boulder. Due to this, we intentionally limit communications during some passes to improve the collection rate of usable data from this region and increase our sampling of the outer radiation belt.
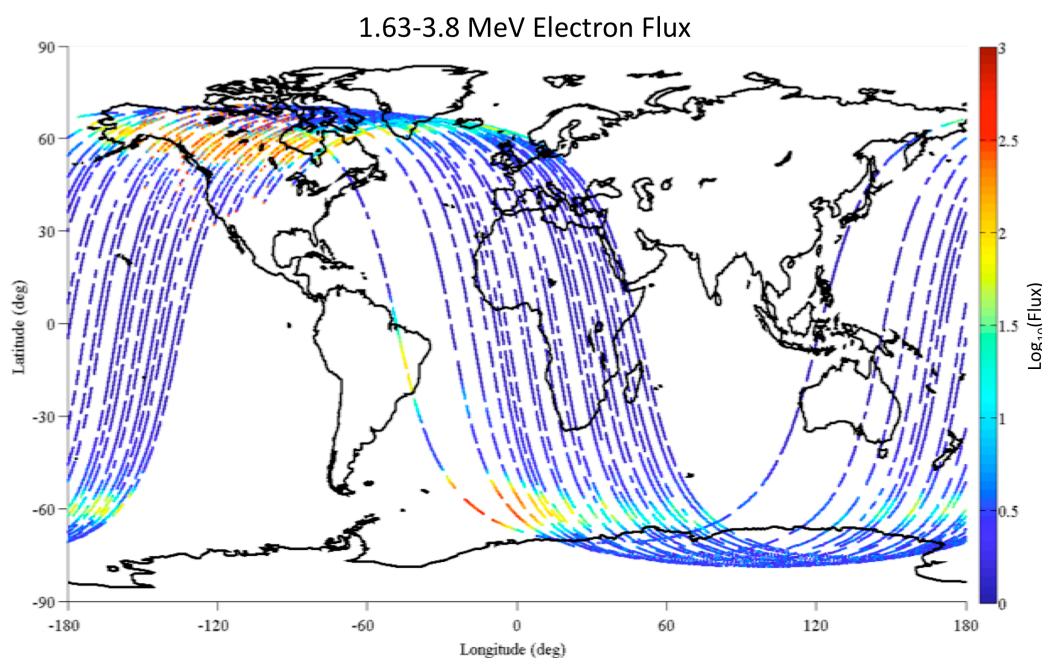
Figure 6.7 Ground tracks of CSSWE, with measured electron flux in the second energy channel on the color scale. Scattered red dots can be seen in the data above North America, which are due to transmission events and contaminate the true measurements.

Furthermore, during periods of high solar beta angle (the angle between the Sun-Earth vector and the satellite orbital plane), the spacecraft interior temperature increases, causing an increase in the leakage current created from the biased detectors. This temperature-dependent noise was observed during TVAC testing performed on the system at LASP before delivery and was anticipated to be an issue during periods when the detector temperature reached >25°C (as

seen in Figure 6.8). As there was no radiation source inside the TVAC chamber, all counts

registered in REPTile here are due to background noise. This noise is largest on Detector 2 and

is subtracted from the data during these hot, high beta angle periods.
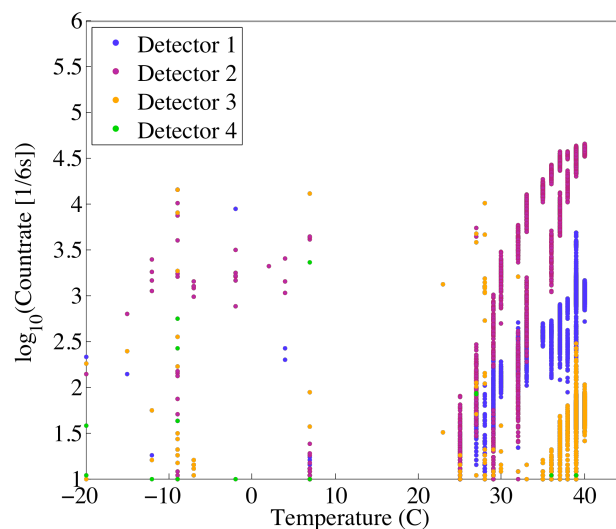
Figure 6.8 Measured singles count rates during thermal vacuum (TVAC) testing as a function of detector temperature for all four REPTile detectors. Maximum operational temperature is ~25° C, at which point system noise potentially overwhelms science data. (From *Blum and Schiller*, 2012)

Orbit beta angle varies on month timescales, as shown by the green line in Figure 6.9.

Also shown here is the REPTile duty cycle (blue). The spacecraft is not power positive during

certain orbital configurations, and over the course of the mission, as the power system continues

to degrade, REPTile on-time has decreased. Due to this duty cycling, coordination with other

missions was required to better allow for conjunction studies such as the one detailed in the

following Chapter. I led the coordination with the BARREL balloon team (campaigns in Jan-

Feb 2013 and 2014) as well as the Firebird CubeSat (Jan-Feb 2014) to ensure that REPTile was

on, data collected by the ground station, and transmit noise minimized during periods of interest

and overlap among missions. The gap from early March through late June 2013 during which

REPTile remained off full time was due to an anomaly causing us to lose contact with the

spacecraft for three months. This is discussed in more detail in *Schiller et al.,* [2014a] as well as in internal documents by David Gerhardt.
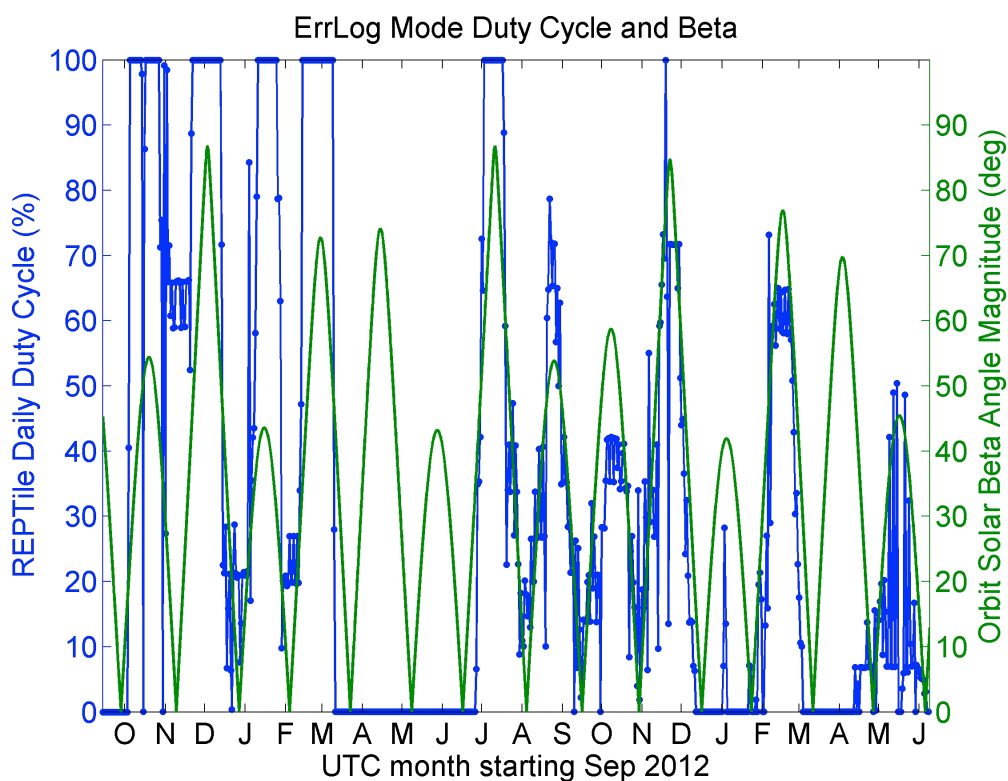
Figure 6.9 Daily averaged percent of time the REPTile instrument was on (blue) and daily averaged orbit beta angle magnitude (green). (Image courtesy of David Gerhardt)

Finally, during periods of high count rates, certain components in the instrument electronics become less efficient at counting the number of incident particles. Specifically, the baseline of the Amptek A225 charge sensitive amplifier drifts downward with increased input pulse rate, causing particles near the lower binning threshold to go uncounted. Figure 6.10 shows the recorded count rate versus input count rate during a lab test performed on the flatsat for a variety of pulse sizes (referenced here by the equivalent deposited energy in a detector, using 22mV/MeV, taken from the A225 spec sheet, to convert from pulse size to energy deposited in the silicon). Perfect counting is shown for 1 MeV deposited energy pulses, but as

pulse size decreases and count rates increase, the undercounting effect is enhanced. This effect is corrected for by characterizing the performance of the A225s to determine the lowest energy of measurable particles as a function of count rate. Thus, with knowledge of the lower energy limit on each channel, particles that are not counted can be corrected for by assuming an energy spectrum and adding the missing fraction of counts back in. An $E^{-\gamma}$ spectrum, where $\gamma=2$ (determined by comparison to Van Allen Probes/MagEIS Medium [*Blake et al.,* 2013] energy spectra), is assumed for convenience, although in reality the spectrum changes as a function of time and space. Quintin Schiller has led the data processing effort and conversion from raw count rates to flux using Monte Carlo simulations to estimate efficiency curves for each energy channel. The full count rate to flux conversion procedure is described in *Li et al.,* [2013a].
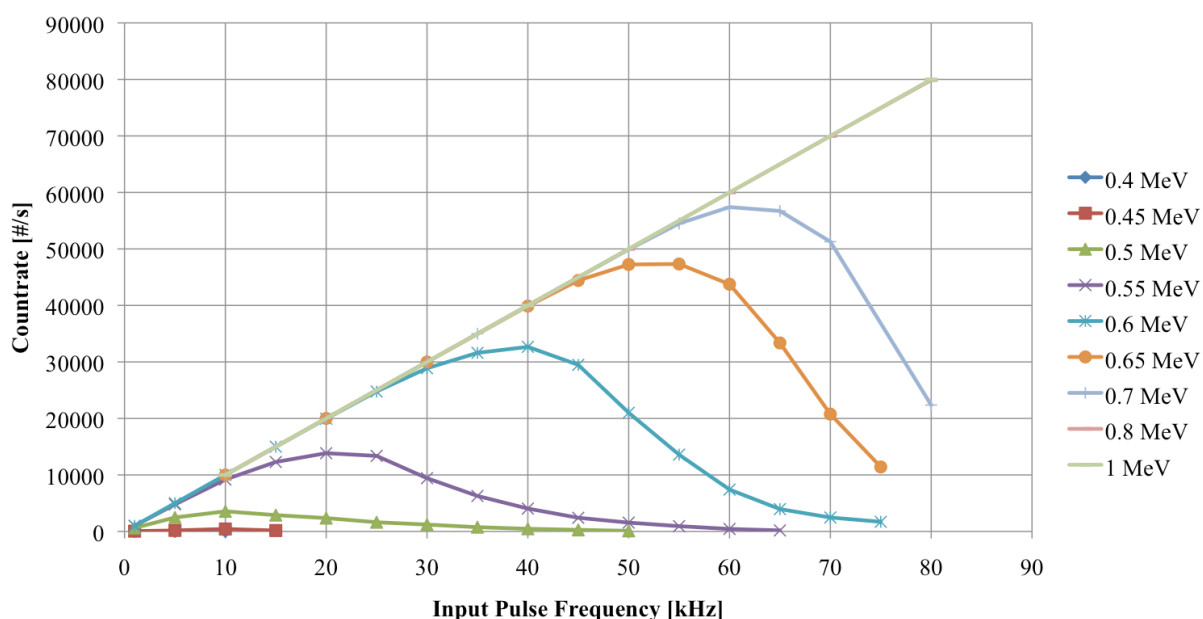
Figure 6.10   Measured versus incident count rate, as determined from lab tests on the CSSWE flatsat. Curves are given for various pulse sizes ranging from the equivalent of 0.4 MeV up to 1 MeV deposited in a detector.

Great care has been taken to ensure that we can accurately remove transmission noise so as to distinguish it from real features in the data, such as precipitation bands as were observed by

SAMPEX. Additionally, the current saturation correction methodology is sufficient for more qualitative comparisons between energy channels, but a detailed study of the changes in energy spectrum over time, especially during periods of high flux, would require a more detailed treatment and correction of this saturation effect. The study presented in Chapter 7 has kept these characteristics of the data products in mind to best accommodate for the strengths and limitations of the REPTile measurements.

6.6 On-Orbit Science Measurements

Figure 6.11 shows daily averaged measurements from the lowest energy electron channel, 0.58-1.63 MeV, and second energy channel, 1.63-3.8 MeV, over the first six months of the mission. The bottom panel shows the Dst index, a measure of geomagnetic activity, during this same period. The dynamic nature of the outer radiation belt is clear from these plots, and already within the first six months of the mission numerous different events have been investigated, including a large storm in October just after the instrument was first turned on [*Li et al.*, 2013a], an extended quiet period in December-January over which slow decay of the outer belt is observed [*Jaynes et al.*, *under review*], an electron enhancement around mid January not associated with a major storm [*Schiller et al.,* 2014b], and a precipitation event observed by both CSSWE and the BARREL balloons [*Blum et al.,* 2013]. The CubeSat continues to operate and return science data, long after its nominal 3-month mission lifetime. After careful data processing, enabled in part by the thorough instrument testing and modeling, we are able to study energetic electron dynamics in the outer radiation belt using the CSSWE mission. These measurements have resulted in numerous scientific publications in addition to engineering papers and conference presentations. The following Chapter details one scientific result using CSSWE

data, in combination with magnetically conjugate BARREL balloon measurements, to characterize and quantify precipitation losses.

Daily Averaged Electron Flux for a) E = 0.58 – 1.63 MeV, b) E = 1.63 – 3.8 MeV
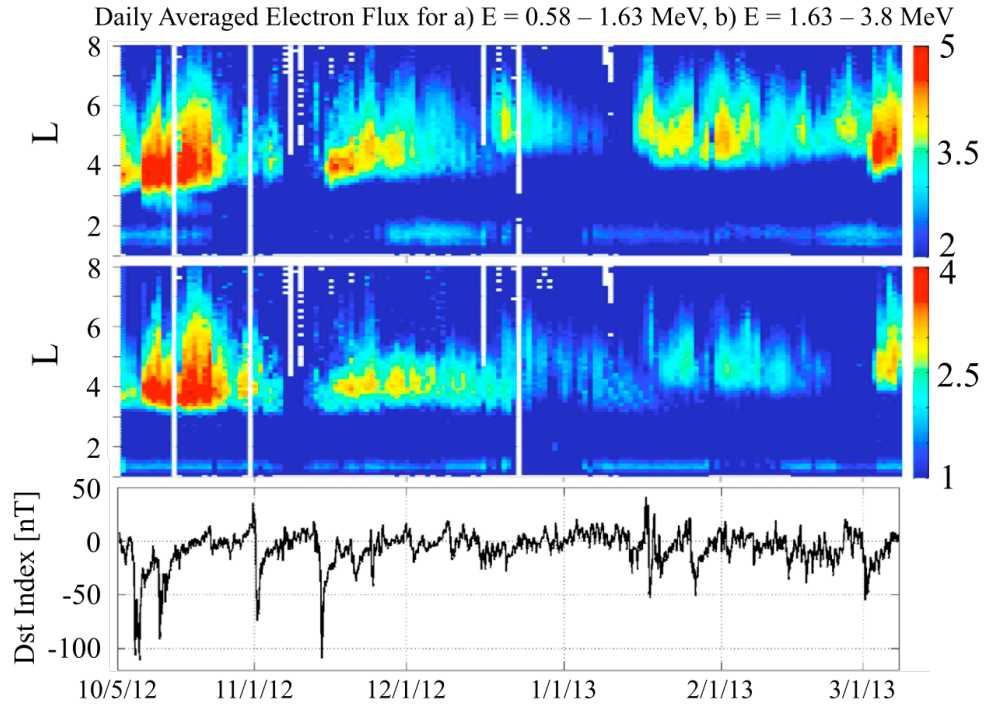
Figure 6.11 Daily averaged fluxes (log scale) from the 0.58-1.63 and 1.63-3.8 MeV electron channels of REPTile (top and middle panels, respectively), and the Dst index (bottom) for the first ~6 months of the CSSWE mission. Several data gaps are due to anomalies that sent the spacecraft into safe mode, turning off the science instrument. The instrument did not operate at 100% duty cycle during some periods, leading to some irregularity, such as the on-off appearance of the inner belt. (From *Li et al.*, 2013a)

Chapter 7: Precipitation Event Characterization and Quantification

The following Chapter is based on work that was published in Blum et al. (2013), New conjunctive CubeSat and balloon measurements to quantify rapid energetic electron precipitation, *Geophys. Res. Lett., 40,* doi:10.1002/2013GL058546.

7.1 Introduction

Particle precipitation into the atmosphere is a critical part of radiation belt electron loss; without quantified understanding of this loss mechanism, we are unable to fully understand acceleration mechanisms. In particular, rapid electron precipitation is often observed at low altitude extending a few degrees in latitude (termed precipitation bands, following *Blake et al*., 1996). These precipitation bands have been hypothesized to be an integral contributor to storm-time relativistic electron precipitation loss [*Bortnik et al*., 2006], but quantification of their net contribution is still needed.

Precipitation bands, also referred to as "spikes" historically (e.g. *Brown and Stone*, 1972), have been observed by a number of satellites in low Earth orbit (LEO). They occur both during quiet and more active times, primarily across the afternoon and night sectors [*Imhof et al.*, 1986; *Nakamura et al.,* 2000]. Their 5-30 sec duration, as observed by LEO satellites, is thought to be spatial rather than temporal, as precipitation bands are often seen on consecutive orbits and in conjugate hemispheres [*Nakamura et al.*, 1995]. Their exact temporal duration is difficult to estimate from a single LEO satellite alone.

Wave-particle interaction theory predicts rapid precipitation events to occur on the duskside due to pitch-angle scattering of MeV electrons by electromagnetic ion cyclotron

(EMIC) waves [*Thorne and Kennel*, 1971]. *Vampola* [1971] suggested that a subset of the precipitation bands measured by the OV3-3 satellite at LEO were the observational signatures of EMIC wave-MeV electron interactions. *Imhof et al*. [1986] found a correspondence between the radial location of precipitation bands and the plasmapause, as well as concurrent keV ion precipitation on a few occasions, further supporting EMIC waves as a cause of the bands. Electrostatic waves and pitch-angle scattering at the trapping boundary have also been proposed precipitation band generation mechanisms [*Koons et al*., 1972; *Brown and Stone*, 1972]. Data from the SAMPEX/HILT instrument, which measures a combination of trapped and precipitating > 1 MeV electrons and provides some pitch angle distribution information, suggest fluxes become more isotropic during these band features, indicating a rapid scattering mechanism and precipitation of the electrons into the atmosphere [*Blake et al.*, 1996; *Li et al*., 1997].

Historically, electron precipitation has also been investigated by balloon campaigns measuring bremsstrahlung x-rays produced by precipitating electrons as they collide with neutrals in the atmosphere (see *Parks et al*., 1993 for a review). *Foat et al*. [1998] presented the first reported measurement of x-rays extending up to MeV energies, indicating relativistic electron precipitation, or "REP". Using measurements from the MAXIS balloon payload, *Millan et al*. [2002] found that REP events were constrained to the afternoon sector, between noon and midnight, while softer precipitation was measured across the full range of local times. SAMPEX/HILT measurements also indicate that harder precipitation events preferentially occur in the afternoon, night and dawn sectors, with a peak occurrence around 22 MLT at an L shell of 5-6 [*Comess et al.*, 2013]. However, due to the inherently different nature of the observations, the exact relationship between the precipitation bands observed at LEO and the REP events seen by balloons is still uncertain.

Here we investigate precipitation bands, as measured at LEO by the Colorado Student Space Weather Experiment (CSSWE) CubeSat [*Li et al.*, 2012, 2013b]. Two precipitation bands were observed by CSSWE on Jan 18-19, 2013, concurrent with relativistic electron precipitation seen by the BARREL balloon array [*Millan et al.*, 2013]. These magnetically conjugate observations confirm the link between precipitation bands and balloon-measured REP and can be used to constrain the duration and extent of the precipitation bands. We calculate the net electron loss due to these precipitation bands and compare to the total radiation belt content at the time. The newly available differential flux measurements from CSSWE, combined with the spatial coverage of the array of BARREL balloons, allow a detailed quantification of precipitation band loss for the first time.

7.2 Rapid Precipitation Observations

7.2.1 Instrument Descriptions

As introduced above, the CSSWE CubeSat, designed, built, and operated by students at the University of Colorado, was launched from Vandenberg Airforce Base on Sept 13, 2012 into a 65° inclination, 480 x 780 km altitude orbit [*Li et al*., 2013b]. The sole science payload onboard is the Relativistic Electron and Proton Telescope integrated little experiment (REPTile), a miniaturized version of the REPT instrument [*Baker et al*., 2012] onboard NASA/Van Allen Probes [*Kessel et al.,* 2012]. This instrument provides 6-second directional, differential electron flux in three energy ranges: .58-1.63, 1.63-3.8, and > 3.8 MeV. With a field-of-view of 52° pointing within 15° of perpendicular to the background magnetic field, REPTile measures a combination of trapped and precipitating particles, similar to the SAMPEX/HILT instrument. Details on the instrument design and calibration can be found in *Schiller and Mahendrakumar*

[2010] and *Blum and Schiller* [2012], and the data processing and conversion to flux is described in *Li et al*. [2013a]. Care has been taken to remove noise due to temperature variations and radio transmissions.

Data from the 2013 Balloon Array for Radiation belt Relativistic Electron Losses (BARREL) campaign are also examined here. Roughly five balloons, distributed in local time and magnetic latitude, were taking measurements at 27-37 km over Antarctica on any given day throughout the Jan-Feb 2013 campaign. These balloons carry x-ray spectrometers sensitive to bremsstrahlung x-rays ranging from 20 keV up to 10 MeV. Using GEANT4 simulations and a forward-folding technique, described in detail in *Millan et al.* [2013], one can estimate the energy spectrum of the incident precipitating electrons from the measured x-ray spectrum (e.g., *Foat et al*., 1998; *Millan et al*., 2007). Here, however, we use the x-ray measurements simply as an indication of energetic electron precipitation, and the CSSWE measurements to determine exact electron energies and fluxes.

7.2.2 Jan 18-19 2013 Precipitation

Late January 18th and early on the 19th, 2013, CSSWE observed two large precipitation bands of MeV electrons. Concurrently, payload 1C of the BARREL balloon array measured x-rays due to energetic electron precipitation. The top panels of Figure 7.1 show the electron flux during two passes of CSSWE through the outer radiation belt on consecutive orbits. Superimposed atop the smoothly varying background of trapped and drift-loss-cone electrons (as indicated by the dashed black curve), a distinct rapid flux enhancement is seen at 23:03 UT 1/18 and again around 00:39 UT 1/19. The bottom panel of Figure 7.1 shows the x-ray spectrum measured by BARREL balloon 1C during this same time period. Three large precipitation events are seen, the second two extending to energies > 0.5 MeV.
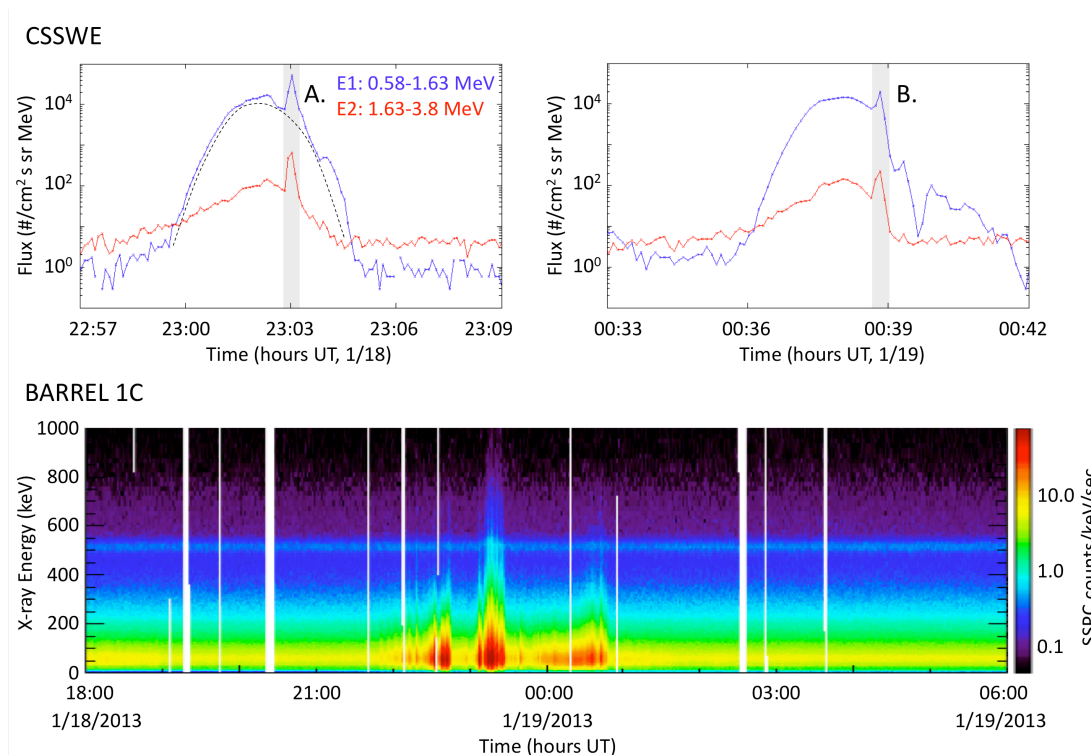
Figure 7.1 **(top) Measurements from the CSSWE CubeSat and (bottom) BARREL balloon 1C during a precipitation event on 18–19 January 2013. CSSWE measures two precipitation bands (labeled A and B and indicated by the shaded grey regions) on two consecutive passes through the outer belt. The dashed black line suggests the background trapped and bounce loss cone flux upon which the precipitation bands are superimposed. (bottom) X-ray spectra from balloon 1C are shown from 18:00 UT 18 January through 06:00 UT 19 January. During this time, three main precipitation events are measured by the balloon, the second two showing X-rays of energies >0.5 MeV. No background subtraction has been applied here to either the BARREL or CSSWE measurements.**

Figure 7.2 shows the location of the two precipitation bands along the ground track of the CubeSat, as well as the balloon 1C position from 22:00 UT 1/18 – 01:00 UT 1/19. The background color indicates 0.5-1.63 MeV electron flux measurements from CSSWE over a two-week period, to demonstrate the typical sampling of the outer and inner radiation belts from the CubeSat orbit. CSSWE is in the Northern hemisphere during both the precipitation band observations, while BARREL is in the Southern, supporting the idea that the bands are an

indication of rapid pitch angle scattering causing simultaneous electron precipitation in both hemispheres.
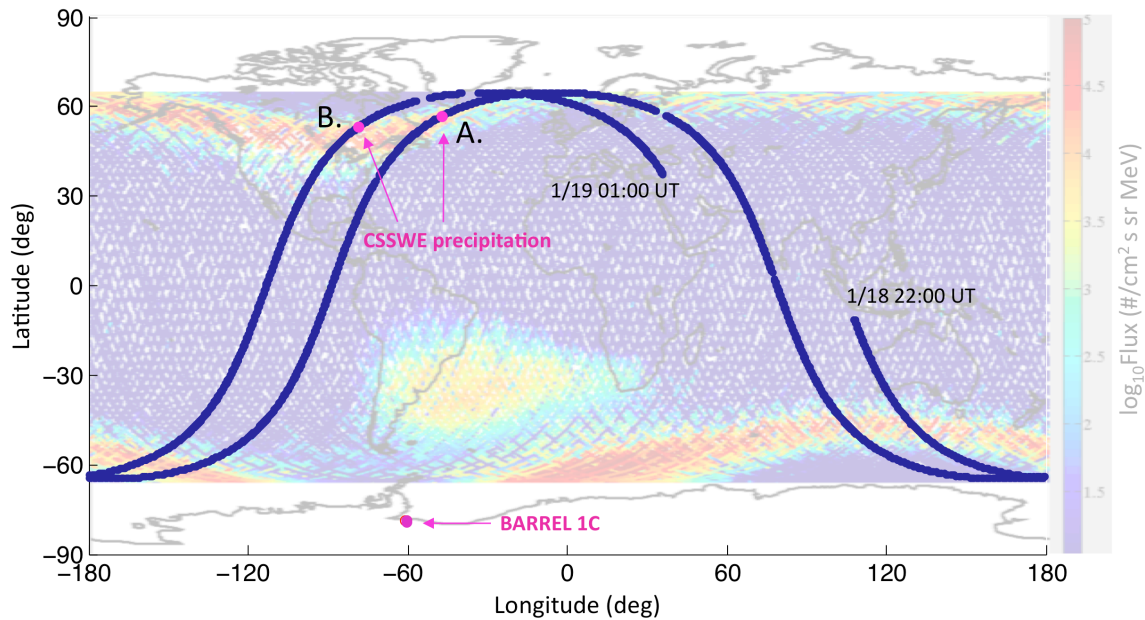
Figure 7.2 The ground track of CSSWE from 22:00 UT 18 January through 01:00 UT 19 January is shown in dark blue, with the location of precipitation bands A and B in pink (band labels are consistent throughout all figures). BARREL balloon 1C was located in the Southern Hemisphere at a conjugate location during this period. The 0.58–1.63 MeV electron measurements from CSSWE during a 2 week period are plotted on the color scale in the background to show typical inner and outer belt sampling by the CubeSat from its low-altitude orbit.

To better investigate the location and timing of the precipitation observed by CSSWE and balloon 1C, their positions are mapped to the magnetic equatorial plane using the T89 magnetic field model [*Tsyganenko*, 1989], with real-time Kp as input (Kp varies between 2 and 3+ during this period). The T89 model has been shown to perform well on the dusk side during quiet to moderate geomagnetic conditions such as these [*McCollough et al*. 2008]. Figure 7.3 shows the CubeSat and balloon locations in this plane in L shell and magnetic local time (MLT). The color bar here indicates universal time of their positions. The periods of precipitation have been marked with black circles; these include the two precipitation bands measured by CSSWE and the second two precipitation occurrences measured by BARREL around 23:15 UT 1/18 and

00:35 UT 1/19. The first precipitation band measured by CSSWE at 23:03 UT 1/18 lines up with the third precipitation region seen by BARREL balloon 1C almost 2 hours later. The second band, measured by CSSWE at 00:39 UT 1/19, is aligned with the precipitation measured by balloon 1C ~23:15 UT 1/18. From this figure, it is evident that the precipitation bands agree in both L and MLT with precipitation seen by BARREL. These magnetically conjugate observations suggest that at least some precipitation bands measured at LEO are the same phenomenon as the REP events seen by balloons.
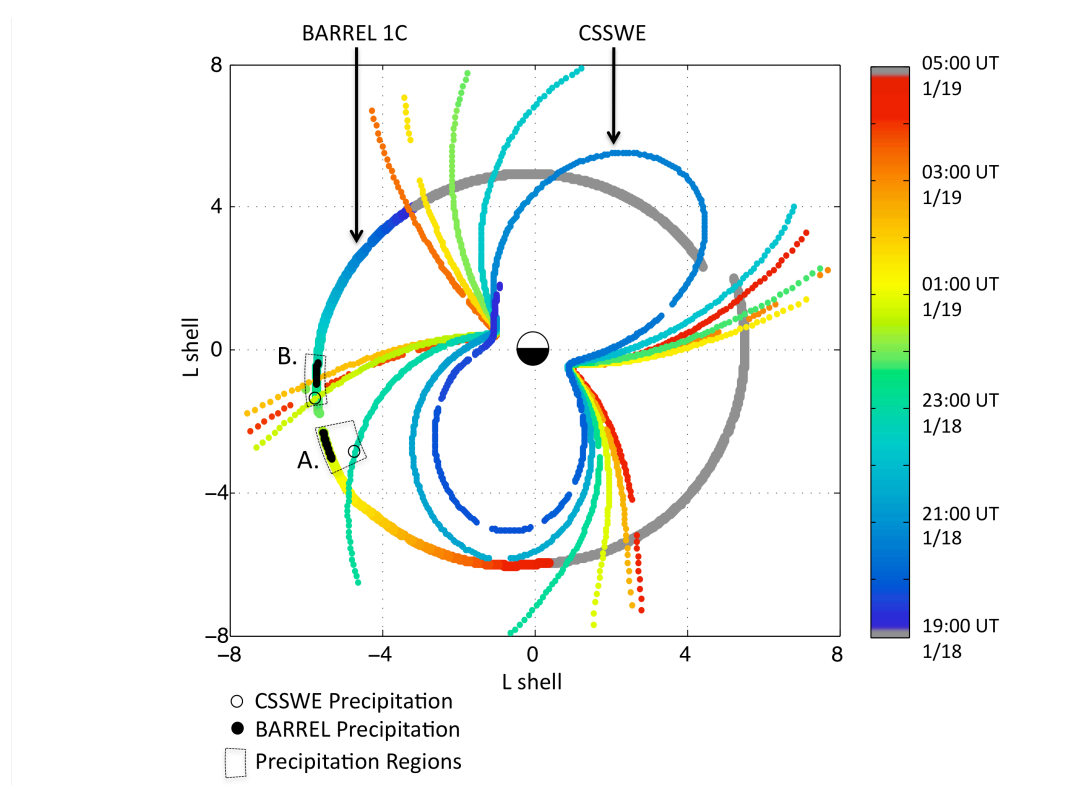
Figure 7.3 The location of CSSWE and balloon 1C mapped to the magnetic equatorial plane, with local noon at the top. Universal time of the locations is shown on the color bar. The balloon drifts across the dusk sector at a fairly constant L ~ 5.5–6, while the CubeSat cuts across this track every roughly 90 min. The locations of the precipitation bands, as measured by CSSWE, are indicated by the open black circles. The tracks of solid black circles indicate when balloon 1C measures >0.5MeV X-rays due to precipitating electrons. The dotted boxes outline the two precipitation regions as determined from the conjunctive measurements, (exact dimensions of these regions are listed in Table 7.1).

7.3 Discussion

7.3.1 Loss Quantification

The balloon and LEO satellite measurements combine to constrain the temporal and spatial features of the precipitation bands. The balloons measure the azimuthal extent of the precipitation in local time, while the bands measured by CSSWE indicate a narrow radial width of the precipitation regions, consistent with a lack of precipitation observed by additional balloons at L~4 and L~8 also in the dusk sector. Combined, they bound the physical dimensions of the precipitation regions, as well as place constraints on the duration of the event in UT. The dashed black boxes in Figure 7.3 outline the precipitation regions estimated from the balloon and CubeSat measurements, with exact dimensions listed in Table 7.1. While the end time of the events is fairly well constrained by subsequent CubeSat passes through the region, these measurements provide only a lower bound on the UT duration, as the precipitation may have begun before the CubeSat and balloons moved into this duskside region.

	Band A			Band B		
Universal Time (UT)	Start: 23:03 1/18[a]	Stop: 00:50 1/19	Δ: 01:47 h	Start: 23:05 1/18	Stop: 00:39 1/19	Δ: 1:34 h
Magnetic Local Time (MLT)	Start: 19:30	Stop: 20:00	Δ: 0.5 h	Start: 18:12	Stop: 18:42	Δ: 0.5 h
Magnetic Latitude (MLAT)	Start: 66.95°	Stop: 65.15°	Δ: 1.8°	Start: 63.1°	Stop: 62.6°	Δ: 0.5°
0.58–1.6 MeV Flux	Peak: 5.3×10^4	Background: 7.7×10^3	Δ: 4.5×10^4	Peak: 2.0×10^4	Background: 6.0×10^3	Δ: 1.4×10^4
1.6–3.8 MeV Flux	Peak: 661.1	Background: 64.42	Δ: 596.68	Peak: 218.5	Background: 34.74	Δ: 183.76

[a]Dates are formatted as month/day.

Table 7.1 The parameters used to calculate area and total loss for precipitation bands A and B (as labeled in Figure 7.1-Figure 7.3).

Using these estimates of the dimensions and duration of the precipitation bands, we are thus able to calculate a lower limit to the overall loss of energetic electrons into the atmosphere during this event. Following the technique used by *Lorentzen et al.* [2001b] and *O'Brien et al.*

[2004] to estimate losses measured by SAMPEX, we calculate the electron flux through the area of the precipitation regions at the altitude of CSSWE using the following equation:

$$\# e- = 2 \cdot \Delta f \cdot \Delta T \cdot A \cdot 2\pi \tag{7.1}$$

where Δf is the magnitude of the precipitation band above the background trapped and drift-loss-cone flux (e.g., solid minus dashed line in Figure 7.1a), ΔT the duration of the precipitation in UT, and A the area of the precipitation region at the CubeSat altitude. The factor 2 comes from assuming conjugate precipitation in both hemispheres and 2π from an assumption of isotropy over the down-going hemisphere.

Table 7.1 lists these parameters estimated for precipitation bands A and B, as determined from Figure 7.1-Figure 7.3. For band A, we calculate an area of $8.35*10^{14}$ cm^2 and a loss of $2.5*10^{24}$ electrons in CSSWE's first energy channel and $6.6*10^{22}$ in the second channel. Band B gives an area of $2.6*10^{14}$ cm^2 and a loss of $2.2*10^{23}$ electrons in the first energy channel and $5.8*10^{21}$ in the second. Combined, these bands produce a total loss of $\sim2.7*10^{24}$ .58-1.63 MeV electrons and $7.2*10^{22}$ 1.63-3.8 MeV electrons. For this analysis we have chosen to group the precipitation measurements by physical location (MLT) rather than UT and magnitude. However, if instead we group precipitation measurements by UT (band A measured by CSSWE paired with precipitation seen by BARREL ~23:15 UT on 1/18) and interpret the events as two shorter duration (~30 min) precipitation regions spanning the duskside from 17:30-20:00 MLT, we get a total loss within a factor of 1.5 of the above calculation. While the observations cannot necessarily distinguish between these two scenarios (two longer duration but narrower in local time precipitation regions versus more extended, but shorter duration, regions), the exact interpretation of the precipitation structure does not significantly affect the estimates here.

For comparison, *Millan et al.* [2002] estimated that a precipitation event measured by the MAXIS balloon in January 2000 produced a loss of ~ $5*10^{25}$ >0.5 MeV electrons over the course of eight days. Another type of rapid precipitation, microbursts, were found by *O'Brien et al.* [2004] to contribute ~10^{23} >1 MeV electrons during one pass of SAMPEX through the outer belt, while *Lorentzen et al.* [2001b] calculate a loss of ~10^{24} for the same pass using a less sophisticated calculation method.

To put these numbers into context, a quick estimate of the total radiation belt content can be made following *O'Brien et al.* [2004]. Using CSSWE measurements of the trapped outer belt population and assuming a sin^n form of the pitch angle distribution with n=2.5 [*Gannon et al.*, 2007], we integrate flux over pitch angle and L shell volume from L=3-6.5. This produces a total electron content of ~$7*10^{25}$ for .58-1.63 MeV electrons and $2*10^{24}$ 1.63-3.8 MeV electrons. If we look at just the drift shells right around the precipitation region (~L=5.5-5.8), we estimate the content to be ~1/10 that of the whole belt.

As shown by these calculations, the precipitation events on Jan 18-19 2013 produced a significant amount of loss, precipitating roughly half the content of their given drift shell and at least 5% of the total outer radiation belt content at the time. Events such as these could easily empty entire drift shells in a few hours, and approximately 20 of them could empty the outer radiation belt. While geomagnetic conditions were relatively mild during this event (Dst ~ -20 nT following a moderate storm on 1/17) and precipitation band occurrence rates are expected to be low during quiet times, ~1-10% [*Nakamura et al.*, 2000], occurrences have been observed to increase during more active periods. During a large storm on November 20, 2003, over 60 precipitation bands were measured by SAMPEX over the three-day storm [*Bortnik et al.,* 2006]. During that storm, as well as others, precipitation bands potentially contributed a large amount of

radiation belt electron loss. Whether these losses lead to radiation belt dropouts and depletions depends upon competing acceleration mechanisms and will be the focus of future work. This study indicates that precipitation losses must be taken into account when studying outer radiation belt dynamics and that precipitation bands, more specifically, can contribute significant rapid losses that may not be fully accounted for if looking only at longer time-averaged precipitation rates.

7.3.2 Potential Scattering Mechanisms

One remaining open question involves the scattering mechanism or mechanisms responsible for rapid precipitation events, and we can use the characteristic spatial features of the precipitation regions investigated here to help shed light on the scattering mechanism. The Jan 18-19 2013 precipitation event extended across the dusk, lasting over an hour in UT, but confined narrowly in L shell. Recent studies [*Mann et al.*, 2014; *Paulson et al.*, 2014] have found electromagnetic ion cyclotron (EMIC) waves showing similar structures, extending a few hours in MLT and UT, but restricted to narrow radial regions. By combining ground and in situ measurements, they confine the EMIC activity to widths of a few tenths of an R_E, but persisting multiple hours in local or universal time (see Figure 7.4).

We have taken a preliminary look at the wave environment during the Jan 18-19 2013 precipitation event. Wave activity from GOES and the Carisma ground magnetometer network (courtesy of M. Engebretson and M. Usanova, respectively) are shown in Figure 7.5a. EMIC activity in the H^+ band is observed from ~12-20 MLT (Figure 7.5b), lasting from ~16 UT on Jan 18 through 02 UT on Jan 19, concurrent with the precipitation observed by CSSWE and BARREL. A more detailed investigation into the potential relationship between the observed EMIC waves and precipitation bands will be performed in future studies.
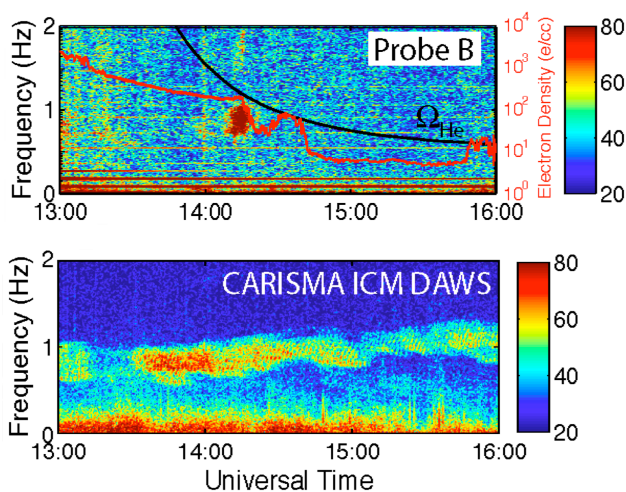
Figure 7.4 Spectrogram of the (top) Bx GSM magnetic field component power from Van Allen Probe B and the (bottom) D-component induction coil magnetometer spectrogram from the Dawson City (DAWS, L=6.09) station of the Carisma ground magnetometer network from 13 to 16 UT on 11 October 2012. The black line shows the local helium gyrofrequency, and the red line shows the electron plasma density derived from spacecraft potential measurements. (Adapted from *Mann et al.,* 2014)
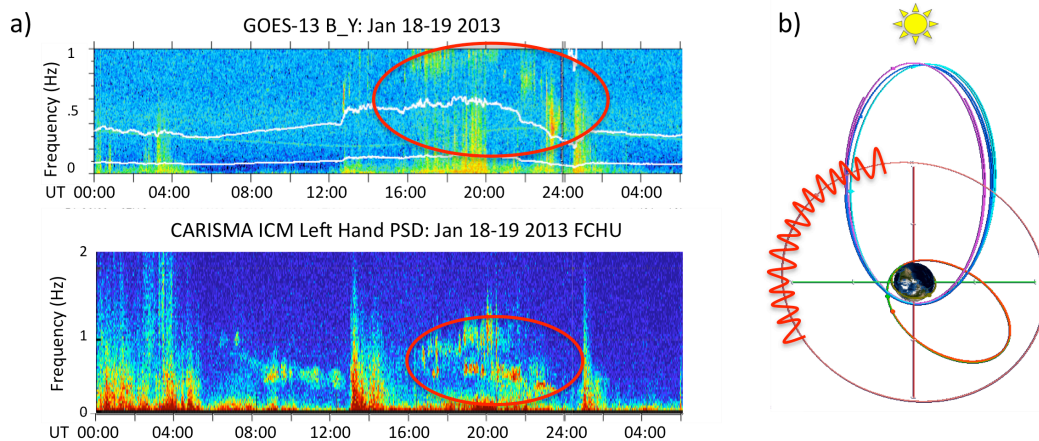
Figure 7.5 (a) Magnetic field spectrograms from the GOES 13 satellite at GEO and the Fort Churchill ground station from Jan 18-19 2013. EMIC wave activity has been circled in red. (b) The location of the GOES 13 (pink), Van Allen Probes A and B (green and red) and THEMIS A, D and E (magenta, cyan, and blue) orbits during this time period. EMIC wave activity as observed by GOES 13 has been indicated in red along the GOES orbit.

7.4 Conclusions

This study combines differential energy measurements of rapid energetic electron precipitation observed by the CSSWE CubeSat at LEO with precipitation measured at lower altitude from the BARREL balloon array. Magnetically conjugate measurements of simultaneous precipitation observed by the CubeSat and balloon 1C on Jan 18-19 2013 help constrain the dimensions and duration of the precipitation regions. The combination of these new measurements enables a detailed estimate of MeV electron loss due to precipitation bands for the first time, to our knowledge. We find that the loss of 0.58-1.63 and 1.63-3.8 MeV electrons during this event was at least 5% of the total outer radiation belt content. The following points summarize the findings of this study:

1. Conjunctive measurements confirm the association between "precipitation band" measurements made by satellites at LEO (e.g. *Brown and Stone*, 1972; *Vampola* 1971; *Imhof et al.*, 1986; *Blake et al.*, 1996) and relativistic electron precipitation "REP" measured by balloons at lower altitude (e.g. *Foat et al.,* 1998; *Millan et al.*, 2002).

2. New measurements from CubeSat and balloon payloads are combined here to estimate the spatial and temporal characteristics of two dusk-side precipitation events.

3. Quantification of the MeV electron loss due to the measured precipitation bands indicates that ~20 such events could empty the entire outer radiation belt.

Using newly available measurements from the CSSWE and BARREL missions in support of the Van Allen Probes, this study demonstrates that precipitation bands, commonly observed during geomagnetic storms, play an important role in outer radiation belt dynamics and losses.

7.5 Statistical Extensions

Some preliminary work has been done to expand this event study and look statistically at conjunctions between CSSWE and the 2013 BARREL balloons to understand the frequency and extent of precipitation events like the one studied above. Following the technique outlined in Section 7.2.2, to better understand the relative locations and timing between balloon and CubeSat measurements we map their positions along magnetic field lines to the magnetic equator using the T89 model with Kp=2. Figure 7.6 shows the balloon and CubeSat locations on January 17 2013 looking down on this plane, with local time indicated by azimuth (noon towards the top) and L shell shown by radial distance from the center. The universal time of these locations is indicated by the color scale, in hours throughout the day. While five BARREL balloons were up on this day, we include only two in this Figure for clarity. By finding places where the CubeSat
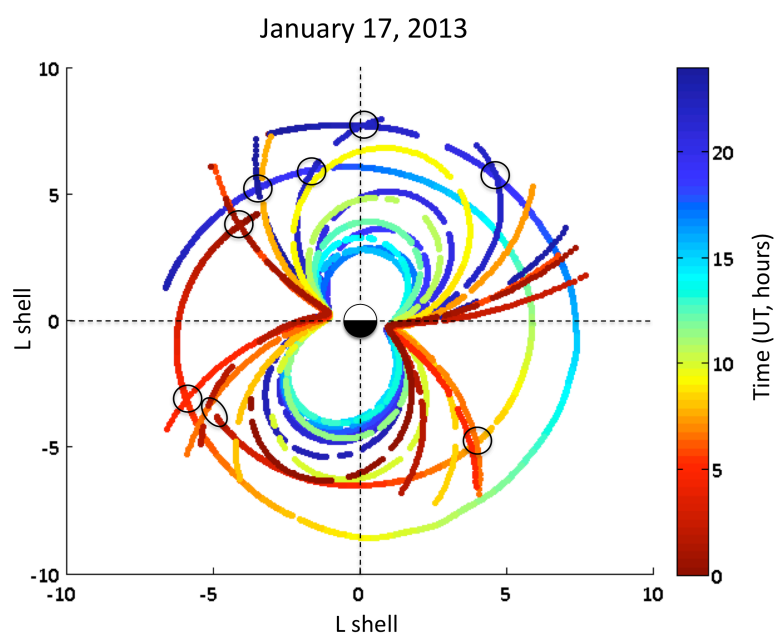
Figure 7.6 The location of CSSWE and two BARREL balloons mapped to the magnetic equatorial plane, with local noon at the top. Universal time of the locations is shown on the color bar. Black circles indicate periods of close magnetic conjunction between the CubeSat and balloons.

and balloon trajectories approach each other, at similar times (colors), we can find periods of close magnetic conjunction between the measurements. The black circles in Figure 7.6 indicate a few such times.

To get a rough idea of the total number of conjuction periods throughout the 2013 BARREL campaign, we can scale the average number of conjunctions per day per balloon by the total length of the campaign as well as the number of balloons up each day. Other considerations include the L shell of the balloons – we are concerned here only with L shells of ~3-8, as we are focused here on radiation belt precipitation and the inner magnetosphere – as well as the duty cycle of the REPTile instrument onboard CSSWE. Figure 7.7 demonstrates the percent of time REPTile was on during the first 6 months of the missions (in blue). The orbit beta angle is overplotted in Figure 7.7 in green. During periods of large beta angle, and thus longer portions
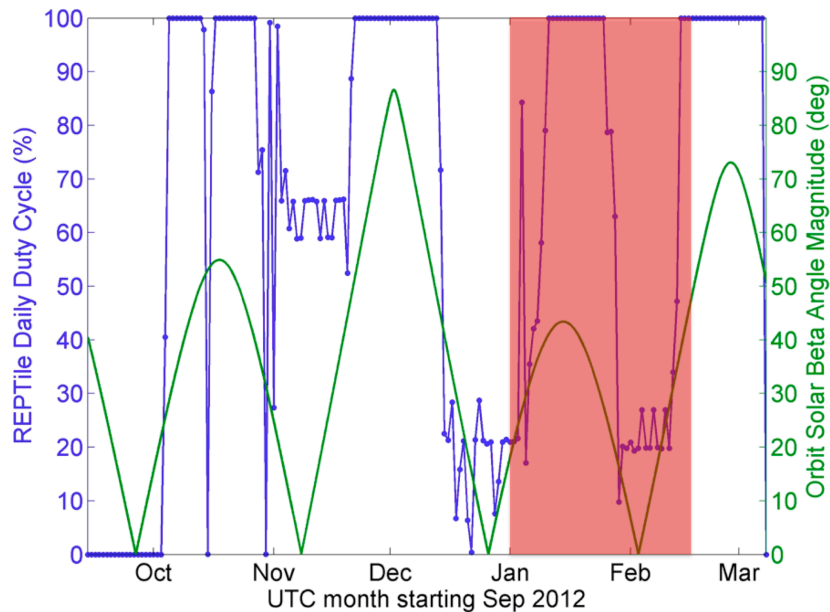
Figure 7.7 **The percent of time REPTile was on during the first 6 months of the missions (blue). This duty cycle is highly dependent on the amount of insolation versus eclipse time on a given CubeSat orbit, which varies on roughly month timescales as the orbit precesses. A measure of this changing insolation time, the orbit beta angle (angle between the Sun-Earth line and orbital plane), is overplotted here (green). The period of overlap with the 2013 BARREL campaign is shaded in orange, during which the REPTile instrument was on anywhere between ~20-100% of the time.**

of the orbit in illumination, the REPTile instrument is able to remain on full time. The period of overlap with the 2013 BARREL campaign is shaded in orange, during which the REPTile instrument is on anywhere between ~20-100% of the time. When taking all these variables into account, we get an average of five conjuctions per balloon per day, 180 balloon-days where balloons are at L<8, and the REPTile duty cycle ranging between ~20-100% during this period. Combining these variables, there are a total of approximately 500 conjunctions between the CSSWE CubeSat and a BARREL balloon over this month-and-a-half campaign.

Moving forward from this analysis, we plan to perform a more rigorous and flexible conjunction finding for the 2013 and 2014 BARREL campaigns. Using a simple Matlab routine, which has been used in the past to calculate conjunctions between the CSSWE CubeSat and Van Allen Probes, we can search routinely for periods of magnetic conjunction between CSSWE and the BARREL balloons now. Defining our search domain to be in L-MLT space, we use an understanding of the physical extents of various processes that may contribute to MeV electron precipitation to define what we consider a conjunction. Starting with criteria of <1 hour MLT, <1 L shell, and <2 hrs UT, we can also vary these parameters to tighten or loosen the conjunction criteria. Examining over what spatial and temporal extents we observe precipitation at both the CubeSat and one, or more, balloons will potentially give insight into the physical extents of precipitation regions. Similarly, finding periods when either the CubeSat or a balloon does not see precipitation while the other one does can also help constrain the area and duration of precipitation events. Our recent studies suggest precipitation regions can persist for hours in regions constrained to narrow radial distances, and this will be tested in a more thorough, statistical manner through future investigations. Putting constraints on the physical extents and

durations of precipitation regions will help in the quantification of MeV electron precipitation loss, a critical open question remaining in the understanding of radiation belt dynamics.

Chapter 8: Summary and Future Work

8.1 Summary and Conclusions

The work in this thesis is motivated by some of the following open questions in radiation belt physics: What processes control the dynamics of the outer radiation belt? When and where do losses dominate over acceleration mechanisms? What role does precipitation into the atmosphere play in these losses, and what mechanisms or wave modes are primarily responsible for the precipitation? We have investigated these questions through a number of techniques and data sets, and a summary of our findings is provided below. Additional ideas for extensions to these studies are also outlined.

In Chapters 3 and 4, we focus on electromagnetic ion cyclotron (EMIC) waves, which are able to resonate with MeV electron and scatter them into the atmosphere. Studying the distributions of these waves, as well as their generation conditions, gives insight into when this particular loss mechanism may be active. In Chapter 3, we develop a plasma-based proxy for EMIC waves and validate the use of it for future investigations of EMIC wave distributions in the inner magnetosphere. Good agreement is found both in the statistical distributions of the inferred and measured waves, as well as for specific case studies investigated. This study demonstrates the powerful applications of plasma data to infer wave distributions in space and to understand the source populations and growth mechanisms of EMIC waves. In Chapter 4 we then use this wave proxy to investigate plasma conditions as well as inferred wave distributions in local time and storm phase during two different sets of storms – ones resulting in post-storm enhancements of outer radiation belt MeV electrons, and ones resulting in no enhancements. We

find statistically significant differences in the various plasma populations during the two sets of storms, as well as a suppression of EMIC waves during the recovery phase of the storms resulting in higher electron fluxes. This is consistent with the idea that EMIC waves can cause increased loss of MeV electrons to the atmosphere, preventing build up of the outer radiation belt during the recovery phase of storms. It also underlines the importance of the balance of loss and acceleration mechanisms in radiation belt dynamics, and suggests that it may often be a suppression of losses rather than increased acceleration that leads to radiation belt enhancements.

We then move to examine precipitating electrons directly, with studies enabled by low altitude measurements from both the 20 year SAMPEX mission as well as the more recent Colorado Student Space Weather Experiment (CSSWE) CubeSat, on orbit since September 2012. Through high-cadence low-altitude measurements from the SAMPEX satellite, we investigate the distributions of millisecond (microburst) as well as longer duration (band-type) precipitation and the relative contributions of these two precipitation features to overall radiation belt dynamics. Dramatically different local time and radial distributions of the between microbursts and precipitation bands support different wave modes as the causal scattering mechanisms for the two precipitation types. In a superposed epoch study of precipitation losses during high speed stream driven storms, we find evidence for significant main and recovery phase losses to the atmosphere, especially at lower L shells, that are not fully captured by instruments with lower time resolution and smaller geometric factors and fields of view than SAMPEX/HILT.

Then using new measurements from the CSSWE CubeSat, built and operated by students here at University of Colorado, we have quantified loss to the atmosphere during some such precipitation events. Careful testing, calibration, and data processing of the CSSWE/REPTile

instrument, outlined in Chapter 6, was required to enable such scientific investigations. Combining CSSWE measurements with those from the 2013 BARREL balloon campaign, we find MeV precipitation constrained narrowly in L shell but occurring across the dusk sector during an event in January 2013. An estimate of the loss due to precipitation during this event indicates that precipitation bands can contribute significant loss of MeV electrons from the outer radiation belt. These conjugate measurements combine to help disentangle the spatial versus temporal extents of precipitation and allow for quantification of loss to the atmosphere during such events.

These studies combine to form a more cohesive picture of the relationship between electromagnetic waves, their source populations, and the interactions of these waves with relativistic electrons in the outer radiation belt. The interplay and energy transfer between particle populations in the inner magnetosphere is especially critical for many of these studies. In particular, it is important to emphasize the role of cold plasma in mediating the generation of electromagnetic waves as well as the interaction of these waves with MeV electrons. Studying specific types of MeV electron precipitation helps answer the question not only of how much loss is due to precipitation events, but what wave modes are responsible for this loss, and how this varies with local time and storm type and phase. We can thus understand the contribution of individual loss mechanisms to the net response of the outer radiation belt. Together these studies aid in understanding the dynamics of the outer radiation belt and the relationship between precipitating energetic electrons and global magnetospheric conditions.

8.2 Potential Extensions and Future Work

There are a number of directions I would like to expand and extend this work, a few of which are outlined briefly below.

8.2.1 EMIC Wave Generation Conditions

Our studies of EMIC wave generation conditions and development of a plasma-based proxy in Chapters 3 and 4 were limited by a number of factors due to the LANL instrumentation that may now be remedied with new Van Allen Probe data. Simultaneous plasma and wave measurements onboard the Van Allen Probes enable a more detailed examination of the validity of such a proxy, as the LANL spacecraft are not equipped with magnetometers and GOES do not provide the necessary plasma parameters to calculate this proxy. Additionally, ion composition measurements provided by the Van Allen Probes/HOPE instrument [*Funsten et al.,* 2013] allow for more in depth investigation into the role of heavy ions in EMIC wave growth. It would also be interesting to compare plasma conditions during EMIC waves occurring in different frequency bands, as waves in the H^+ versus He^+ band have been shown to have distinctly different local time distributions [*Min et al.*, 2012].

8.2.2 Further Precipitation Investigations

I would also like to look more directly and quantitatively into the link between electromagnetic waves and radiation belt precipitation in the inner magnetosphere. A few such studies have been initiated and suggested earlier in the text. Are the distinct temporal and spatial characteristics of rapid precipitation events determined by wave distributions? Or does cold plasma structure dictate some features, such as the narrow radial extent of precipitation bands observed at LEO? Comparisons between the global plasmaspheric images from the IMAGE satellite and precipitation distributions observed by SAMPEX may shed light on some of these questions. Additional comprehensive wave, cold plasma, and radiation belt measurements in the inner magnetosphere from the Van Allen Probes, combined with BARREL and CSSWE precipitation measurements, will also be valuable in this effort. Resonance conditions at the

equator will be investigated to more directly connect wave activity to pitch angle scattering and compare expected precipitation characteristics (energy spectrum, temporal and spatial features, etc.) with measured ones.

Bibliography

Albert, J. M. (2003), Evaluation of quasi-linear diffusion coefficients for EMIC waves in a multispecies plasma, J. Geophys. Res., 108(A6), 1249, doi:10.1029/2002JA009792.

Anderson, K. A. and D. W. Milton (1964), Balloon observations of x-rays in the auroral zone, J. Geophys. Res., 69, 21.

Anderson, B. J., R. E. Denton, G. Ho, D. C. Hamilton, S. A. Fuselier, and F. J. Strangeway (1996), Observational test of local proton cyclotron instability in the Earth's magnetosphere, J. Geophys. Res., 101, 21,527–21,543, doi:10.1029/96JA01251.

Anderson, B. J., R. E. Erlandson, and L. J. Zanetti (1992), A statistical study of Pc1–2 magnetic pulsations in the equatorial magnetosphere: 1. Equatorial occurrence distributions, J. Geophys. Res., 97(A3), 3075–3088, doi:10.1029/91JA02706.

Baker, D. N., Mason, G. M., Figueroa, O., Colon, G., Watzin, J. G., and R. M. Aleman (1993), An overview of the solar anomalous, and magnetospheric particle explorer (SAMPEX) mission, Geoscience and Remote Sensing, IEEE Transactions on, 31(3), 531-541.

Baker, D. N., et al. (2012), The Relativistic Electron-Proton Telescope (REPT) instrument on board the Radiation Belt Storm Probes (RBSP) spacecraft: Characterization of Earth's radiation belt high-energy particle populations, Space Sci. Rev., 179, 337–381, doi:10.1007/s11214-012-9950-9.

Baker, D. N., et al. (2013), A Long-Lived Relativistic Electron Storage Ring Embedded in Earth's Outer Van Allen Belt, Science, 340 (6129), 186-190, doi:10.1126/science.1233518.

Blake, J. B., M.D. Looper, D.N. Baker, R. Nakamura, B. Klecker, and D. Hovestadt (1996), New High Temporal and Spatial Resolution Measurements by SAMPEX of the Precipitation of Relativistic Electrons, Adv. Space Res. 18, 171-186.

Blake, J. B., et al. (2013), The Magnetic Electron Ion Spectrometer (MagEIS) instruments aboard the Radiation Belt Storm Probes (RBSP) spacecraft, *Space Sci. Rev.,* doi:10.1007/s11214-013-9991-8.

Blum, L. W., E. A. MacDonald, S. P. Gary, M. F. Thomsen, and H. E. Spence (2009), Ion observations from geosynchronous orbit as a proxy for ion cyclotron wave growth during storm times, J. Geophys. Res. 114, A10214, doi:10.1029/2009JA014396.

Blum, L. W., E. A. MacDonald, L. B. N. Clausen, and X. Li (2012), A comparison of magnetic field measurements and a plasma-based proxy to infer EMIC wave distributions at geosynchronous orbit, J. Geophys. Res., 117, A05220, doi:10.1029/2011JA017474.

Blum, L. W., Q. Schiller, X. Li, R. Millan, A. Halford, and L. Woodger (2013), New conjunctive CubeSat and balloon measurements to quantify rapid energetic electron precipitation, Geophys. Res. Lett., 40, doi:10.1002/ 2013GL058546.

Blum, L. W. and Q. G. Schiller (2012), Characterization and testing of an energetic particle telescope for a CubeSat platform, Small Satellite Conference, AIAA/USU.

Borovsky, J. E. and M. H. Denton (2009), Relativistic-electron dropouts and recovery: A superposed epoch study of the magnetosphere and the solar wind, J. Geophys. Res., 114(A2), A02201.

Borovsky, J. E. and M. H. Denton (2006), Differences between CME-driven storms and CIR-driven storms, *J. Geophys. Res., 111,* A07S08, doi:10.1029/2005JA011447.

Bortnik, J., N. Omidi, L. Chen, R. M. Thorne, and R. B. Horne (2011), Saturation characteristics of electromagnetic ion cyclotron waves, J. Geophys. Res., 116, A09219, doi:10.1029/2011JA016638.

Bortnik, J., R. M. Thorne, T. P. O'Brien, J. C. Green, R. J. Strangeway, Y. Y. Shprits, and D. N. Baker (2006), Observation of two distinct, rapid loss mechanisms during the 20 November 2003 radiation belt dropout event, J. Geophys. Res., 111, A12216, doi:10.1029/2006JA011802.

Bortnik, J., and R. M. Thorne (2007), The dual role of ELF/VLF chorus waves in the acceleration and precipitation of radiation belt electrons, *J. Atmos. Sol. Terr. Phys., 69,* 378-386, doi:10.1016/j,jastp.2006.05.030.

Bossen, M., R. L. McPherron, and C. T. Russell (1976), A statistical study of Pc 1 magnetic pulsations at synchronous orbit, J. Geophys. Res., 81, 6083–6091, doi:10.1029/JA081i034p06083.

Brown, J. W. and E. C. Stone (1972), High-energy electron spikes at high latitudes, Journal of Geophys. Res., 77, 19.

Burch, J. L. (2000), Image mission overview, *Space Sci. Rev., 91,* 1.

Carson, B. R., C. J. Rodger, and M. A. Clilverd (2012), POES satellite observations of EMIC-wave driven relativistic electron precipitation during 1998-2010, *J. Geophys. Res., 118,* doi:10.1029/2012JA017998.

Cattell, C., et al. (2008), Discovery of very large amplitude whistler-mode waves in Earth's radiation belts, Geophys. Res. Lett., 35, L01105, doi:10.1029/2007GL032009.

Chen, L., V. K. Jordanova, M. Spasojevic, R. M. Thorne, and R. B. Horne (2014), Electromagnetic ion cyclotron wave modeling during the geospace environment modeling challenge event, J. Geophys. Res. Space Physics, 119, doi:10.1002/2013JA019595.

Chen, L., R. M. Thorne, V. K. Jordanova, C.-P. Wang, M. Gkioulidou, L. Lyons, and R. B. Horne (2010), Global simulation of EMIC wave excitation during the 21 April 2001 storm from coupled RCM-RAM- HOTRAY modeling, J. Geophys. Res., 115, A07209, doi:10.1029/ 2009JA015075.

Clausen, L. B. N., J. B. H. Baker, J. M. Ruohoniemi, and H. J. Singer (2011), EMIC waves observed at geosynchronous orbit during solar minimum: Statistics and excitation, J. Geophys. Res., 116, A10205, doi:10.1029/2011JA016823.

Comess, M. D., D. M. Smith, R. S. Selesnick, R. M. Millan, and J. G. Sample (2013), Duskside relativistic electron precipitation as measured by SAMPEX: A statistical survey, J. Geophys. Res. Space Physics, 118, doi:10.1002/jgra.50481.

Cornwall, J. M., F. V. Coroniti, and R. M. Thorne (1970), Turbulent loss of ring current protons, J. Geophys. Res., 75(25), 4699–4709, doi:10.1029/ JA075i025p04699.

Denton, M. H., M. F. Thomsen, H. Korth, S. Lynch, J. C. Zhang, and M. W. Liemohn (2005), Bulk plasma properties at geosynchronous orbit, J. Geophys. Res., 110, A07223, doi:10.1029/2004JA010861.

Denton, M. H., J. E. Borovsky, R. M. Skoug, M. F. Thomsen, B. Lavraud, M. G. Henderson, R. L. McPherron, J. C. Zhang, and M. W. Liemohn (2006), Geomagnetic storms driven by ICME- and CIR-dominated solar wind, J. Geophys. Res., 111, A07S07, doi:10.1029/2005JA011436.

Denton, M. H., and J. E. Borovsky (2008), Superposed epoch analysis of high-speed-stream effects at geosynchronous orbit: hot plasma, cold plasma, and the solar wind, *J. Geophys. Res., 113*, A07216, doi:10.1029/2007JA012998.

Dietrich, S., C. J. Rodger, M. A. Clilverd, J. Bortnik, and T. Raita (2010), Relativistic microbursts storm characteristics: Combined satellite and ground-based observations, J. Geophys. Res., 115, A12240, doi:10.1029/2010JA015777.

Engebretson, M. J., et al. (2008), Pc1-Pc2 waves and energetic particle precipitation during and after magnetic storms: Superposed epoch analysis and case studies, J. Geophys. Res., 113, A01211, doi:10.1029/ 2007JA012362.

Erlandson, R. E., and A. E. Ukhorskiy (2001), Observations of electro- magnetic ion cyclotron waves during geomagnetic storms: Wave occurrence and pitch angle scattering, J. Geophys. Res., 106(A3), 3883–3895, doi:10.1029/2000JA000083.

Evans, D. S., and M. S. Greer (2004), Polar orbiting environmental satellite space environment monitor – 2. Instrument descriptions and archive data documentation, verson 2.0, technical memorandum, Space Environ. Lab., NOAA, Boulder, Colo. (Available at http://ngdc.noaa.gov/stp/satellite/poes/documentation.html).

Fälthammar, C. G. (1965), Effects of time-dependent electric fields on geomagnetically trapped radiation, J. Geophys. Res., 70(11), 2503-2516.

Foat, J. E., R. P. Lin, D. M. Smith, F. Fenrich, R. Millan, I. Roth, K. R. Lorentzen, M. P. McCarthy, G. K. Parks, and J. P. Treilhou (1998), First detection of a terrestrial MeV X-ray burst, Geophys. Res. Lett., 25, 4109–4112.

Fraser, B. J., and T. S. Nguyen (2001), Is the plasmapause a preferred source region of electromagnetic ion cyclotron waves in the magnetosphere?, J. Atmos. Sol. Terr. Phys., 63, 1225–1247, doi:10.1016/S1364- 6826(00)00225-X.

Fraser, B. J., R. S. Grew, S. K. Morley, J. C. Green, H. J. Singer, T. M. Loto'aniu, and M. F. Thomsen (2010), Storm time observations of electromagnetic ion cyclotron waves at geosynchronous orbit: GOES results, J. Geophys. Res., 115, A05208, doi:10.1029/2009JA014516.

Funsten, H. O., et al. (2013), Helium, Oxygen, Proton, and Electron (HOPE) mass spectrometer for the Radiation Belt Storm Probes mission, *Space Sci. Rev.,* doi:10.1007/s11214-013-9968-7.

Gannon, J. L., X. Li, and D. Heynderickx (2007), Pitch angle distribution analysis of radiation belt electrons based on Combined Release and Radiation Effects Satellite Medium Electrons A data, J. Geophys. Res., 112, A05212, doi:10.1029/2005JA011565.

Gary, S. P., Theory of Space Plasma Microinstabilities, Cambridge Univ. Press, New York, 1993.

Gary, S. P., M. B. Moldwin, M. F. Thomsen, D. Winske, and D. J. McComas (1994), Hot proton anisotropies and cool proton temperatures in the outer magnetosphere, J. Geophys. Res., 99, 23,603–23,615, doi:10.1029/ 94JA02069.

Gendrin, R., M. Ashour-Abdalla, Y. Omura, and K. Quest (1984), Linear analysis of ion cyclotron interaction in a multicomponent plasma, J. Geophys. Res., 89, 9119–9124, doi:10.1029/JA089iA10p09119.

Gerhardt, D. (2010), Passive magnetic attitude control for CubeSat spacecraft, *Small Satellite Conference,* AIAA/USU.

Goldstein, J., M. Spasojevic, P. H. Reiff, B. R. Sandel, W. T. Forrester, D. L. Gallagher, and B. W. Reinisch (2003), Identifying the plasmapause in IMAGE EUV data using IMAGE RPI in situ steep density gradients, *J. Geophys. Res., 108*(A4), 1147, doi:10.1029/2002JA009475.

Green, J. C. and M. G. Kivelson (2004), Relativistic electrons in the outer radiation belt: differentiating between acceleration mechanisms, *J. Geophys. Res., 109*, A03213, doi:10.1029/2003JA010153.

Green, J. C., T. G. Onsager, T. P. O'Brien, and D. N. Baker (2004), Testing loss mechanisms capable of rapidly depleting relativistic electron flux in the Earth's outer radiation belt, J. Geophys. Res., 109, A12211, doi:10.1029/2004JA010579.

Halford, A. J., B. J. Fraser, and S. K. Morley (2010), EMIC wave activity during geomagnetic storm and nonstorm periods: CRRES results, J. Geophys. Res., 115, A12248, doi:10.1029/2010JA015716.

Hendry, A. T., Rodger, C. J., Lilverd, M. A., Thomson, N. R., Morley, S. K. and Raita, T. (2013), Rapid radiation belt losses occurring during high-speed solar wind stream-driven storms: importance of energetic electron precipitation, in Dynamics of the Earth's Radiation Belts and Inner Magnetosphere (eds D. Summers, I. R. Mann, D. N. Baker, and M. Schulz), American Geophys. Union, Washington, D. C., doi:10.1029/2012GM001299.

Horne, R. B., and R. M. Thorne (1993), On the preferred source location for the convective amplification of ion cyclotron waves, J. Geophys. Res., 98(A6), 9233–9247, doi:10.1029/92JA02972.

Horne, R. B., et al. (2005), Wave acceleration of electrons in the Van Allen radiation belts, Nature, 437(7056), 227-230.

Horne, R. B., Lam, M. M., and J. C. Green (2009), Energetic electron precipitation from the outer radiation belt during geomagnetic storms, Geophys. Res. Lett., 36(19).

Huang, C., H. Spence, and H. Singer (2009), Identifying loss mechanisms of radiation belt electrons during flux dropout events, *Eos Trans. AGU, Fall Meet. Suppl. 90*, abstract SM23A-1591.

Hudson, M. K., D. N. Baker, J. Goldstein, B. T. Kress, J. Paral, F. R. Toffeletto, and M. Wiltberger (2014), Simulated magnetopause losses and Van Allen Probe flux dropouts, Geophys. Res. Lett., 41, doi:10.1002/2014GL059222.

Imhof, W. L., Robinson, R. M., Collin, H. L., Wygant, J. R., & Anderson, R. R. (1992). Simultaneous equatorial measurements of waves and precipitating electrons in the outer radiation belt. Geophys. Res. Lett., 19(24), 2437-2440.

Imhof, W. L., H. D. Voss, J. B. Reagan, D. W. Datlowe, E. E. Gaines, and J. Mobilia (1986), Relativistic electron and energetic ion precipitation spikes near the plasmapause, J. Geophys. Res., 91, A3, 3077-3088.

Jaynes, A. N., X. Li, Q. G. Schiller, L. W. Blum, W. Tu, D. L. Turner, B. Ni, J. Bortnik, D. N. Baker, S. G. Kanekal, J. B. Blake, and J. Wygant (*under review)*, Evolution of relativistic outer belt electrons during an extended quiescent period, *J. Geophys. Res.*

Johnston, W. R., and P. C. Anderson (2010), Storm time occurrence of relativistic electron microbursts in relation to the plasmapause, J. Geophys. Res. (1978–2012), 115(A2).

Jordanova, V. K., J. U. Kozyra, A. F. Nagy, and G. V. Khazanov (1997), Kinetic model of the ring current-atmosphere interactions, J. Geophys. Res., 102(A7), 14,279–14,291, doi:10.1029/96JA03699.

Jordanova, V. K., C. J. Farrugia, R. M. Thorne, G. V. Khazanov, G. D. Reeves, and M. F. Thomsen (2001), Modeling ring current proton precipitation by electromagnetic ion cyclotron waves during the 14–16 May 1997 storm, J. Geophys. Res., 106(A1), 7–22, doi:10.1029/2000JA002008.

Kavanagh Jr., L. D., J. W. Freeman Jr., and A. J. Chen (1968), Plasma flow in the magnetosphere, *J. Geophys. Res.,* 73(17), 5511-5519, doi:10.1029/JA073i017p05511.

Kennell, C. F., and H. E. Petschek (1966), Limit on stably trapped particle fluxes, *J. Geophys. Res., 71,* 1.

Kersten, K., C. A. Cattell, A. Breneman, K. Goetz, P. J. Kellogg, J. R. Wygant, L. B. Wilson, J. B. Blake, M. D. Looper, and I. Roth (2011), Observation of relativistic electron microbursts in conjunction with intense radiation belt whistler‐mode waves, Geophys. Res. Lett., 38(8).

Kessel, R. L., N. J. Fox, and M. Weiss (2012), The Radiation Belt Storm Probes (RBSP) and space weather, Space Sci. Rev., 179, 531–543, doi:10.1007/s11214-012-9953-6.

Kivelson, M. G. and C. T. Russell (Eds.), Introduction to Space Physics, Cambridge Univ. Press, New York, 1995.

Koons, H. C., Vampola, A. L., and D. A. McPherson (1972), Strong pitch-angle scattering of energetic electrons in the presence of electrostatic waves above the ionospheric trough region, J. Geophys. Res., 77(10), 1771-1775.

Kozyra, J., T. Cravens, A. Nagy, E. Fontheim, and R. Ong (1984), Effects of energetic heavy ions on electromagnetic ion cyclotron wave generation in the plasmapause region, J. Geophys. Res., 89, 2217–2233, doi:10.1029/JA089iA04p02217.

Li, W., Thorne, R. M., Bortnik, J., Tao, X., and V. Angelopoulos (2012), Characteristics of hiss‐like and discrete whistler‐mode emissions, Geophys. Res. Lett., 39(18).

Li, X., D. Baker, M. Temerin, T. E. Cayton, E. G. D. Reeves, R. A. Christensen, J. B. Blake, M. D. Looper, R. Nakamura, and S. G. Kanekal (1997), Multisatellite observations of the outer zone electron variation during the November 3-4, 1993, magnetic storm, J. Geophys. Res., 102, 14,123–14,140.

Li, X., et al. (2012), Colorado Student Space Weather Experiment: Differential flux measurements of energetic particles in a highly inclined low Earth orbit, in Dynamics of the Earth's Radiation Belts and Inner Magnetosphere, Geophys. Monogr. Ser., vol. 199, edited by D. Summers et al., pp. 385-404, AGU, Washington, D. C., doi:10.1029/ 2012GM001313.

Li, X., et al. (2013a), First results from CSSWE: Characteristics of relativistic electrons in the near-earth environment during the October 2012 magnetic storms, J. Geophys. Res. Space Physics, 118, 1–11, doi:10.1002/ 2013JA019342.

Li, X., S. Palo, R. Kohnert, L. Blum, D. Gerhardt, Q. Schiller, and S. Califf (2013b), Small mission accomplished by students—Big impact on Space Weather Research, Space Weather, 11, 55–56, doi:10.1002/swe.20025.

Lin, R. -L., et al. (2014), Testing linear theory of EMIC waves in the inner magnetosphere: Cluster observations, *J. Geophys. Res., 119,* 1004-1027, doi:10.1002/2013JA019541.

Lorentzen, K. R., Blake, J. B., Inan, U. S., and J. Bortnik (2001a), Observations of relativistic electron microbursts in association with VLF chorus, J. Geophys. Res. (1978–2012), 106(A4), 6017-6027.

Lorentzen, K. R., M. D. Looper, and J. B. Blake (2001b), Relativistic electron microbursts during the GEM storms, Geophys. Res. Lett., 28, 2573–2576.

Loto'aniu, T. M., B. J. Fraser, and C. L. Waters (2005), Propagation of electromagnetic ion cyclotron wave energy in the magnetosphere, J. Geophys. Res., 110, A07214, doi:10.1029/2004JA010816.

Lyons, L. R., and R. M. Thorne (1973), Equilibrium structure of radiation belt electrons, J. Geophys. Res., 78(13), 2142-2149.

Lyons, L. R. and D. J. Williams, *Quantitative aspects of magnetospheric physics*, D. Reidel, Dordrecht-Holland, 1984.

MacDonald, E. A., M. H. Denton, M. F. Thomsen, and S. P. Gary (2008), Superposed epoch analysis of a whistler instability criterion at geosynchronous orbit during geomagnetic storms, J. Atmos. Sol. Terr. Phys., 70, 1789–1796, doi:10.1016/j.jastp.2008.03.021.

MacDonald, E. A., L. W. Blum, S. P. Gary, M. F. Thomsen, and M. H. Denton (2010), High-speed stream driven inferences of global wave distributions at geosynchronous orbit: Relevance to radiation-belt dynamics, Proc. R. Soc. A, 466, 3351–3362, doi:10.1098/rspa.2010.0076.

Madden, D. and M. S. Gussenhoven (1990), Auroral boundary index from 1983 to 1990. Technical Report no. GL-TR-90-0358, Air Force Goephysics Laboratory, Hanscom AFB, MA.

Mann, I. R., M. E. Usanova, K. Murphy, M. T. Robertson, D. K. Milling, A. Kale, C. Kletzing, J. Wygant, S. Thaller, and T. Raita (2014), Spatial localization and ducting of EMIC waves: Van Allen Probes and ground-based observations, *Geophys. Res. Lett., 41*, 785-792, doi:10.1002/2013GL058581.

McCollough, J. P., J. L. Gannon, D. N. Baker, and M. Gehmeyr (2008), A statistical comparison of commonly used external magnetic field models, Space Weather, 6, S10001, doi:10.1029/2008SW000391.

McIlwain, C. E. (1961), Coordinates for mapping the distribution of magnetically trapped particles, *J. Geophys. Res., 66*, 3681-3691.

Mende, S. B., et al. (2000), Far ultraviolet imaging from the image spacecraft. 3. Spectral imaging of lyman-α and oi 135.6 nm, *Space Sci. Rev., 91,* 287.

Meredith, N. P., R. M. Thorne, R. B. Horne, D. Summers, B. J. Fraser, and R. R. Anderson (2003), Statistical analysis of relativistic electron energies for cyclotron resonance with EMIC waves observed on CRRES, J. Geophys. Res., 108(A6), 1250, doi:10.1029/2002JA009700.

Meredith, N. P. et al. (2006), Energetic outer zone electron loss timescales during low geomagnetic activity, J. Geophys. Res., 111(A5), A05,212.

Meredith, N. P., Horne, R. B., Lam, M. M., Denton, M. H., Borovsky, J. E., and J. C. Green (2011), Energetic electron precipitation during high-speed solar wind stream driven storms, J. Geophys. Res. (1978–2012), 116(A5).

Millan, R. M., R. P. Lin, D. M. Smith, and M. P. McCarthy (2007), Observations of relativistic electron precipitation during a rapid decrease of trapped relativistic electron flux, Geophys. Res. Lett., 34, L10101, doi:10.1029/2006GL028653.

Millan, R. M., R. P. Lin, D. M. Smith, K. R. Lorentzen, and M. P. McCarthy (2002), X-ray observations of MeV electron precipitation with a balloon-borne germanium spectrometer, Geophys. Res. Lett., 29, 24, 2194, doi:10.1029/2002GL015922.

Millan, R. M., and R. M. Thorne (2007), Review of radiation belt relativistic electron losses, J. Atmos. Sol. Terr. Phys., 69, 362.

Millan, R. M., K. B. Yando, J. C. Green, and A. Y. Ukhorskiy (2010), Spatial distribution of relativistic electron precipitation during a radiation belt depletion event, Geophys. Res. Lett., 37, L20103, doi:10.1029/ 2010GL044919.

Millan, R. M., et al. (2013), The Balloon Array for RBSP Relativistic Electron Losses (BARREL), Space Sci. Rev., 179, 503–530, doi:10.1007/s11214-013-9971-z.

Min, K., J. Lee, K. Keika, and W. Li (2012), Global distribution of EMIC waves derived from THEMIS observations, *J. Geophys. Res., 117,* A05219, doi:10.1029/2012JA017515.

Miyoshi, Y., K. Sakaguchi, K. Shiokawa, D. Evans, J. Albert, M. Connors, and V. Jordanova (2008), Precipitation of radiation belt electrons by EMIC waves, observed from ground and space, Geophys. Res. Lett., 35, L23101, doi:10.1029/2008GL035727.

Miyoshi, Y., and R. Kataoka (2005), Ring current ions and radiation belt electrons during geomagnetic storms driven by coronal mass ejections and corotating interaction regions, Geophys. Res. Lett., 32, L21105, doi:10.1029/2005GL024590.

Morley, S. K., R. HW Friedel, E. L. Spanswick, G. D. Reeves, J. T. Steinberg, J. Koller, T. Cayton, and E. Noveroske (2010), Dropouts of the outer electron radiation belt in response to solar wind stream interfaces: global positioning system observations, Proc. R. Soc. A, 466(2123), 3329-3350.

Nakamura, R., Isowa, M., Kamide, Y., Baker, D. N., Blake, J. B., and M. Looper (2000), SAMPEX observations of precipitation bursts in the outer radiation belt, J. Geophys. Res., 105(A7), 15875-15885.

Nakamura, R., D. N. Baker, J. B. Blake, S. Kanekal, B. Klecker, and D. Hovestadt (1995), Relativistic electron precipitation enhancements near the outer edge of the radiation belt, J. Geophys. Res., 22, 1129–1132.

O'Brien, T. P., R. L. McPherron, D. Sornette, G. D. Reeves, R. Friedel, and H. J. Singer (2001), Which magnetic storms produce relativistic electrons at geosynchronous orbit?, J. Geophys. Res., 106, 15,533–15,544, doi:10.1029/2001JA000052.

O'Brien, T. P., K. R. Lorentzen, I. R. Mann, N. P. Meredith, J. B. Blake, J. F. Fennel, M. D. Looper, D. K. Milling, and R. R. Anderson (2003), Energization of relativistic electrons in the presence of ULF wave power and MeV microbursts: evidence for dual ULF and VLF acceleration, J. Geophys. Res., 108, 1329.

O'Brien, T. P., and M. B. Moldwin (2003), Empirical plasmapause models from magnetic indices, Geophys. Res. Lett., 30(4).

O'Brien, T. P., Looper, M. D., and J. B. Blake (2004), Quantification of relativistic electron microburst losses during the GEM storms, Geophys. Res. Lett., 31(4).

Parks, G. K., T. J. Freeman, M. P. McCarthy, and S. H. Werden (1993), The discovery of auroral X-rays by balloon-borne detectors and their contributions to magnetospheric research, in Auroral Plasma Dynamics, Geophys. Monogr. Ser., vol. 80, edited by R. L. Lysak, pp. 17–23, AGU, Washington, D. C., doi:10.1029/GM080p0017.

Paulikas, G. A., Blake, J. B., and S. C. Freden (1966), Precipitation of energetic electrons at middle latitudes, J. Geophys. Res., 71(13), 3165-3172.

Paulson, K. W., C. W. Smith, M. R. Lessard, M. J. Engebretson, R. B. Torbert, and C. A. Kletzing (2014), In situ observations of Pc1 pearl pulsations by the Van Allen Probes, Geophys. Res. Lett., 41, doi:10.1002/2013GL059187.

Posch, J. L., M. J. Engebretson, M. T. Murphy, M. H. Denton, M. R. Lessard, and R. B. Horne (2010), Probing the relationship between electromagnetic ion cyclotron waves and plasmaspheric plumes near geosynchronous orbit, J. Geophys. Res., 115, A11205, doi:10.1029/ 2010JA015446.

Reeves, G. D. et al. (2013), Electron acceleration in the heart of the Van Allen radiation belts, Science, 341(6149), 991-994, doi:10.1126/science.1237743.

Reeves, G. D., K. L. McAdams, R. H. W. Friedel, and T. P. O'Brien (2003), Acceleration and loss of relativistic electrons during geomagnetic storms, Geophys. Res. Lett., 30(10), 1529, doi:10.1029/2002GL016513.

Roederer, J. G., Dynamics of Geomagnetically Trapped Radiation, Springer, New York, 1970.

Sarachaga, M. H., et al. (2014), Study of geomagnetic storms and assessment of their impact on technology and infrastructure in Spain and Portugal, *Seguridad y Medio Ambiente, 34*, 133.

Schiller, Q. and A. Mahendrakumar (2010), REPTile: A miniaturized detector for a CubeSat mission to measure relativistic particles in near-earth space, Small Satellite Conference, AIAA/USU.

Schiller, Q., D. Gerhardt, L. Blum, X. Li, and S. Palo (2014a), Design and scientific return of a miniaturized particle telescope onboard the Colorado Student Space Weather Experiment (CSSWE) CubeSat, IEEE Aerospace Conference, 8.1102.

Schiller, Q., X. Li, L. Blum, W. Tu, D. L. Turner, and J. B. Blake (2014b), A nonstorm time enhancement of relativistic electrons in the outer radiation belt, *Geophys. Res. Lett., 41,* 7-12, doi:10.1002/2013GL058485.

Schulz, M. and L. Lanzerotti, *Particle Diffusion in the Radiation Belts*, Springer, New York, 1974.

Shprits, Y. Y., Thorne, R. M., Friedel, R., Reeves, G. D., Fennell, J., Baker, D. N., and S. G. Kanekal (2006), Outward radial diffusion driven by losses at magnetopause, J. Geophys. Res. (1978–2012),111(A11).

Smith, A. J., N. P. Meredith, and T. P. O'Brien (2004), Differences in ground-observed chorus in geomagnetic storms with and without enhanced relativistic electron fluxes, J. Geophys. Res., 109, A11204, doi:10.1029/ 2004JA010491.

Spasojevic, M., H. U. Frey, M. F. Thomsen, S. A. Fuselier, S. P. Gary, B. R. Sandel, and U. S. Inan (2004), The link between a detached subauroral proton arc and a plasmaspheric plume, Geophys. Res. Lett., 31, L04803, doi:10.1029/2003GL018389.

Spasojevic, M., and S. A. Fuselier (2009), Temporal evolution of proton precipitation associated with the plasmaspheric plume, J. Geophys. Res., 114, A12201, doi:10.1029/2009JA014530.

Spasojevic, M., L. W. Blum, E. A. MacDonald, S. A. Fuselier, and D. I. Golden (2011), Correspondence between a plasma-based EMIC wave proxy and subauroral proton precipitation, Geophys. Res. Lett., 38, L23102, doi:10.1029/2011GL049735.

Summers, D., R. M. Thorne, and F. Xiao (1998), Relativistic theory of wave-particle resonant diffusion with application to electron acceleration in the magnetosphere, *J. Geophys. Res., 103(A9),* 20487-20500, doi:10.1029/98JA01740.

Summers, D., and R. M. Thorne (2003), Relativistic electron pitch-angle scattering by electromagnetic ion cyclotron waves during geomagnetic storms, J. Geophys. Res., 108(A4), 1143, doi:10.1029/2002JA009489.

Temerin, M., I. Roth, M. K. Hudson, and J. R. Wygant (1994), New paradigm for the transport and energization of radiation belt particles, AGU, Eos, 538.

Thomsen, M. F., E. Noveroske, J. E. Borovsky, and D. J. McComas (1999), Calculation of moments from measurements by the Los Alamos Magnetospheric Plasma Analyzer, LA Rep. LA-13566-MS, Los Alamos Natl. Lab., Los Alamos, N. M.

Thomsen, M. F. (2004), Why Kp is such a good measure of magnetospheric convection, *Space Weather, 2,* S11004.

Thorne, R. M., and C. F. Kennel (1971), Relativistic electron precipitation during magnetic storm main phase, J. Geophys. Res., 76(19), 4446-4453.

Thorne, R. M., Horne, R. B., Glauert, S., Meredith, N. P., Shprits, Y. Y., Summers, D., and Anderson, R. R. (2013), The influence of wave-particle interactions on relativistic electron dynamics during storms, in Inner Magnetosphere Interactions: New Perspectives from Imaging (eds J. Burch, M. Schulz and H. Spence), American Geophysical Union, Washington, D. C., doi:10.1029/159GM07.

Thorne, R. M., O'Brien, T. P., Shprits, Y. Y., Summers, D., and R. B. Horne (2005), Timescale for MeV electron microburst loss during geomagnetic storms, J. Geophys. Res. (1978–2012), 110(A9).

Tsurutani, B. T., and G. S. Lakhina (1997), Some basic concepts of wave-particle interactions in collisionless plasmas, Reviews of Geophysics, 35(4), 491-501.

Tsyganenko, N. A. (1989), A magnetospheric magnetic field model with a warped tail current sheet, Planet. Space Sci., 37, 5–20, doi:10.1016/0032- 0633(89)90066-4.

Tu, W., R. Selesnick, X. Li, and M. Looper (2010), Quantification of the precipitation loss of radiation belt electrons observed by SAMPEX, J. Geophys. Res., 115, A07210, doi:10.1029/2009JA014949.

Turner, D. L., et al. (2014), On the cause and extent of outer radiation belt losses during the 30 September 2012 dropout event, J. Geophys. Res., 119, doi:10.1002/2013JA019446.

Turner, D. L., Shprits, Y., Hartinger, M., and V. Angelopoulos (2012), Explaining sudden losses of outer radiation belt electrons during geomagnetic storms, Nature Physics, 8(3), 208-212.

Vampola, A. L. (1977), The effect of strong pitch angle scattering on the location of the outer-zone electron boundary as observed by low-altitude satellites, J. Geophys. Res., 82(16), 2289-2294.

Vampola, A. L. (1971), Electron pitch angle scattering in the outer zone during magnetically disturbed times, J. Geophys. Res., 76, 19.

Vampola, A. L. (1998), "Measuring Energetic Electrons," Measurement Techniques in Space Plasmas: Particles, edited by R. F. Pfaff, J. E. Borovsky, and D. T. Young, Geophysical Monograph, American Geophysical Union, p. 102.

Yando, K., R. M. Millan, J. C. Green, and D. S. Evans (2011), A Monte Carlo simulation of the NOAA POES Medium Energy Proton and Electron Detector instrument, *J. Geophys. Res., 116,* A10231, doi:10.1029/2011JA016671.